THESIS

A FINITE ELEMENT ANALYSIS OF FLEXIBLE DEBRIS-FLOW BARRIERS

Submitted by

Aliena Marie Debelak

Department of Civil and Environmental Engineering

In partial fulfillment of the requirements

For the Degree of Master of Science

Colorado State University

Fort Collins, Colorado

Summer 2018

Master's Committee:

Advisor: Christopher A. Bareither

Hussam N. Mahmoud
Lisa Stright

ABSTRACT

A FINITE ELEMENT ANALYSIS OF FLEXIBLE DEBRIS FLOW BARRIERS

The objective of this study was to simulate the stress-displacement behavior of a flexible debris-flow mitigation structure with a three-dimensional finite element model (FEM). Flexible, steel ring-net structures are becoming state-of-practice for debris-flow mitigation in mountainous terrain. These structures have been shown effective in geohazard mitigation; however, design of these structures commonly does not incorporate coupled interactions between debris flow mechanics and stress-strain response of the steel structure Thus, this study focused on assessing the effectiveness of using a FEM model in ABAQUS to simulate coupled behavior encountered in a flexible debris-flow mitigation structure. The debris flow was modeled as a series of rectangular solid blocks and the flexible debris-flow barrier was modeled as a series of three individual parts – braking elements, cables, and rings. The primary model outputs evaluated were the temporal and spatial relationships of forces within the structure and final barrier deformation. A full-scale field experiment from literature was used as a benchmark test to validate FEM simulations, and subsequently the FEM was used to assess barrier sensitivity via a parametric study. Parameters were chosen to represent common geotechnical variables of the debris flow and structural variables of the steel, ring-net structure.

TABLE OF CONTENTS

LIST OF TABLES

LIST OF FIGURES

CHAPTER 1: INTRODUCTION

Debris flows are moving masses of loose solid particles, water, and air that present an inherent risk to human health, infrastructure, and the environment due to their rapid development and downslope movement (Iverson 1997; Santi 2012; Hungr et al. 2014). Debris flows primarily develop on steep slopes (>10-20°) and can mobilize directly from a mass of soil or rock, grow from a small failure with subsequent entrainment of sediment from bed-slope erosion, or initiate from surface water runoff with subsequent erosion and particle entrainment (e.g., Varnes 1978; Hungr et al. 2005; Hungr et al. 2014). The size, extent, and frequency of debris flows vary considerably with respect to surface material composition, geologic setting, and amount of water present (Jakob 2004).

Landslides, and in particular debris flows, often occur along transportation corridors in mountainous regions due to the presence of disturbed soil and rock involved in roadway construction and steep slopes (Highland 2012). Debris flows are an ever present and growing risk for transportation corridors in the Western United States. The ability to understand practical hazard mitigation possibilities prior to the occurrence of a debris flow can provide transportation personnel and consulting engineers vital tools to enhance protection of human life, infrastructure, and the environment.

Debris flow mitigation structures most commonly are deployed in the vicinity of infrastructure, and include flexible barriers, levees and dams, and baffles (Mizuyama 2008; Wendeler et al. 2008; Santi 2012; Ng. et al. 2014; Choi et al. 2015). The most successful mitigation strategies involve entrapping debris as the material moves downslope to prevent an increase in debris flow volume due to channel erosion and entrainment (e.g., Iverson 1997; Santi 2012). These common mitigation structures are often expensive and labor intensive to build, and present difficulties with construction and maintenance in remote areas. Retention-type systems, such as silt fences and basins, can quickly fill with sediment and water and easily

overflow. Due to the construction challenges and performance limitations with current debris flow mitigation strategies, recent research has focused on the efficacy of flexible steel, ring-net barriers.

Flexible steel, ring-net barriers designed as debris flow barrier systems typically include (i) a steel mesh or ring-type structure that spans the width of a channel and (ii) a connection system that anchors the steel structure to the earth. The structure is designed to intercept and retain material and is constructed of loosely connected high tensile-strength steel wire rings or mesh that is supported by steel wire ropes anchored to the ground (DeNatale et al 1999; Roth et al. 2010; Canelli et al 2012; Volkein et al. 2011; Brighenti et al 2013; Volkein et al. 2015). The open, freely-draining properties of the steel rings or mesh allow water and small debris to pass through the barrier, which increases material retention capacity and reduces pore-pressure build-up behind the barrier. Flexible barriers are light-weight and require minimal space for installation, which is ideal for installation in remote locations (Sasiharan et al. 2006) and along transportation corridors where right-of-way and zoning issues pose design constraints for hazard mitigation structures (Wendeler et al. 2008). Roth et al. (2010) report that flexible barrier systems were effective in mitigating large erosion events and that retention capacity of the barrier system can be restored by removing accumulated debris.

Recent research on flexible debris flow barriers has focused on (i) model development to estimate impact force on a barrier and subsequent deformation and (ii) field and laboratory testing of the barriers (Roth et al 2010). Equations based on the principal of kinetic energy have been developed to determine impact forces of debris flows on structures, which can be used in barrier design (e.g. Armanini 1997; Brighenti et al 2014; Volkwein 2014; Volkwein et al. 2015). However, this technique does not include stress-strain behavior and structural response of the barrier to loading induced by the debris flow (Ashwood and Hungr 2016).

Field and laboratory testing of debris flow barriers has been used to assess structural response of a barrier to dynamic loading caused by the debris flow. Experiments conducted with

artificially generated debris flows (deNatale et a 1999; Bugnion et al. 2008; Canelli et al. 2012; Ferrero et al. 2015; Ashwood and Hungr 2016) may not adequately represent loads expected in situ and results may be confounded by scale effects (Volkwein et al. 2015). Full-scale testing of barrier structures with natural debris flows (Wendeler et al. 2006, 2007, 2008) provides the most realistic loading scenario. However, full-scale experiments of debris flows are expensive and labor intensive, which limits the practicality of conducting multiple experiments to evaluate variability or different design parameters (Volkwein et al. 2015).

Recent advances in numerical modeling have enabled simulation of dynamic debris flow events for barrier systems (e.g., Volkwein et al. 2015). However, numerical modeling efforts have focused on either the response of a complex barrier structure to empirically derived impact forces (Wendeler et al. 2006, 2007, 2008; Von Boetticher et al. 2011) or the impact of a complex, multi-phase debris flow on a simplified barrier (e.g. Leonardi et al. 2014; Calvetti et al. 2015). Limited work has been conducted on coupling debris flow behavior, dynamic nature of the impact forces, and corresponding response of a ring-net flexible barrier system (Ferrero et al. 2015).

The objectives of this study were to (i) create a model using finite element analysis that couples a debris flow and flexible barrier system and (ii) evaluate the response of the model to different debris flow and barrier system parameters. The model was verified via comparison to barrier deformation and cable tension data collected from a full-scale flexible barrier experiment conducted by Ferrero et al. (2015). The verified model of the barrier was then used to systematically investigate (i) response of the barrier to different loading scenarios and (i) response of the barrier to different structural properties of the barrier components.

CHAPTER 2: BACKGROUND

2.1 Debris Flows

A debris flow is a gravity-induced rapid mass movement composed of solid, air, and liquid phases (Costa 1984). The air phase typically is ignored, particles silt size and smaller are considered part of the fluid phase, and particles sand size and larger are considered the solid phase (Iverson 1997; Iverson 2005). The mechanical nature of a debris flows is fluid-like and ranges between a sediment-laden water flow, which contains minor particle interaction from fluid motion, and a rock avalanche, where nearly all particles interact with neighboring particles (Costa 1984; Iverson 1984). In a debris flow, energy is transferred via particle-fluid interactions and particle-particle interactions (Iverson 2005). Velocity is dependent on slope, water content, and grain distribution (Brighenti et al. 2013) and typically ranges between 0.5 m/s and 10 m/s (Coussot and Meunier 1996; Costa 1984). The relative velocity between solid particles and fluid is small, and debris flows are often viewed as a composite deforming mass. Bulk densities of debris flows typically range from 1900 kg/m^3 to 2300 kg/m^3 (Coussot and Meunier 1996; Iverson 1997). The size, extent, and frequency of debris flows vary considerably with respect to surface material composition, geologic setting, and amount of water present. The debris flow path contains an initiation zone, transport zone, and deposition zone (Jakob and Hungr 2005).

2.1.1 Initiation

2.1.1.1 Geologic Conditions

Debris flows typically occur when there is abundant source material of unconsolidated rock and debris, steep slopes, a large discrete source of moisture, and limited vegetation (Costa 1984). Debris flows typically initiate on slopes steeper than 20^o (Jakob and Hungr 2005; Godt and Coe 2007; Iverson 2013), are less than 3000 m^2 in area (Godt and Coe 2007), and contain

cohesionless soil (Jakob and Hungr 2005; Mears 1997; Iverson 2013). Rock and soil slopes that are susceptible to weathering have more frequent debris flows (Costa 1984).

2.1.1.2 Triggering Mechanisms

Development of a debris flow requires failure of a mass of soil or rock, sufficient water to mobilize the mass, and conversion of gravitational potential energy to kinetic energy to change the motion of a sliding mass to deformation recognized as a flow (Iverson 1997). Most debris flows begin on steep slopes consisting of poorly sorted rock or soil and a rapid influx of water (Costa 1984). As the debris materials begins to move downslope, the loose debris contracts and rearranges, which increases pore pressure, reduces shear strength, and promotes liquefaction (Jakob and Hungr 2005; Iverson 2013) There are three initiation processes for debris flows: shallow landslides, riling, and the firehose effect (Godt and Coe 2007).

The development of debris flows from shallow landslides is the least common initiation mechanism. Translational slope failures can transition into debris flows due to liquefaction induced from excess pore water pressure or a sudden increase in slope angle (Costa 1984; Coussot and Meunier 1996). Debris flows that develop from shallow landslides typically have low energy that is dissipated rapidly, which results in short travel distances (Coe and Godt 2003; Godt and Coe 2007).

Rilling is a process that typically coincides with precipitation whereby channels erode onto the surface of the slope. This process is common on unvegetated hillslopes with loose colluvium and when bedrock is close to the surface. An increase in available water to initiate rilling will lead to increased erosion, and subsequently the increase in material entrained in the flow will increase the erosive and entrainment energy promoting growth of the debris flow. Eventually the debris flow will become localized in a channel and additional channel deposits can become mobilized in the flow (Costa 1984). A debris flow will continue to run-out until the flow escapes confinement in the channel and/or the slope decreases, which promotes energy

dissipation and demobilization of entrained particles. Debris flows caused by rilling are generally more disastrous because they increase in energy as flow occurs (Coussot and Meunier 1996; Coe and Godt 2003; Godt and Coe 2007).

The firehose effect often occurs on steep, bare rock outcrops located above talus deposits (Godt and Coe 2007). Overland flow mobilizes loose sediment and eventually reaches a channel. As water enters the channel, more debris is mobilized and the energy of the flow continues to increase as additional material mobilizes (Coe and Godt 2003; Godt and Coe 2007). Any unconsolidated sediment within the channel can become mobilized in the flow (Costa 1984; Coussot and Meunier 1996).

2.1.1.3 Wildfire Induced Flows

Detailed assessments of debris flows in the Western United States have been conducted for both unburned and burned areas following wildfires (e.g., Santi et al. 2013). Wildfires have a pronounced influence on the hydrologic response of watersheds, and debris flows are a hazardous consequence of rainfall on burned slopes (Parrett 1987; Morton 1989; Meyer and Wells 1997; Cannon 2001; Cannon 2005; Gartner et al 2007). The increase in debris flow activity on burned slopes is a result of reduced infiltration and an increase in sediment supply such that runoff dominated erosion is the dominant triggering mechanism (Swanson 1981; Spittler 1995; Doerr et al. 2000; Cannon et al 2001; Martin and Moody 2001; Moody and Martin 2001b; Wondzell and King, 2003; Cannon 2005; Cannon and Gartner 2005; Santi et al 2006; Godt and Coe 2007; Santi et al 2008; Cannon 2010; Santi and Morandi 2013). Wildfires remove vegetation that protects surface soil from raindrop impact forces and can create hydrophobic conditions in surface sediments, which reduces infiltration and promotes erosion, rapid runoff, and overland flow (Swanson 1981; Spittler 1995; Doerr et al. 2000; Martin and Moody 2001; Moody and Martin 2001b; Wondzell and King, 2003; Cannon and Gartner 2005; Gartner et al 2007; Cannon 2010; Santi and Morandi 2013).

2.1.2 Run-Out

Debris flows grow in volume as they travel down a channel and can continue to flow on slopes greater than 10° (Hunger et al 2005). The main sources for sediment entrainment are erosion of the channel, destabilization of the channel bed due to bed instability and drag forces, and liquefaction caused from rapid undrained loading (Hungr et al 2005; Iverson 2013).

Debris flows commonly include a broad range of particle sizes, ranging from clay to boulders (Phillips and Davis 1991; Hungr 1995). The properties of a debris flow depend on the clay content, particle gradation, and sediment sorting (Costa 1984). Analyses of debris flows have indicated that approximately 10-20% of material is silt and clay size particles, with the largest particle dependent on the average flow depth. On average, 50-90% of debris flows can be characterized as the solid phase with the reminder characterized as the fluid phase (Costa 1984; Phillips and Davis 1991; Coussot and Meunier 1996; Iverson 1997; Iverson 2005).

A cross-sectional schematic of a typical debris flow is shown in Figure 2.1. The head of a debris flow is considered to be a frictional, steady, uniform flow that tends to contain the largest particle sizes, largest flow depth, and limited pore pressure (Costa 1984; Hungr 1999; Iverson 2013). In contrast, the tail of the debris flow is primarily the fluid phase with some suspended particles, and is characterized by high pore water pressures and turbulent flow (Costa 1984; Iverson 2013). The liquefied flow in the tail provides energy to push coarser-grained particles at the head of the flow. In general, the range in particle sizes and flow height of the tail decreases with distance from the flow head (Hungr 1999). Impact from debris flows is experienced as a series of surges where each surge is equal to the height of the debris flow. After initial impact on an object, the debris flow will continue to flow over the now existing deposit from the original surge. This process repeats itself until the structure is overtopped or fails (Wendeler 2006; Wendeler et al. 2007; Brighenti et al 2013; Volkwein et al. 2011; Volkwein et al 2014; Ashwood and Hungr 2016).

2.1.3 Deposition

Debris flows lose velocity upon reaching a decrease in slope or decrease in confinement (e.g., widening of a channel). These changes allow a debris flow to spread out and thin, and deposition occurs as energy in the flow is no longer sufficient to overcome fictional resistance of the channel bed or sides (Costa 1984; Jakob and Hungr 2005; Iverson 2013). Deposition is encouraged by limited sediment supply, insufficient water, and rapid drainage (Jakob 2004). The lateral extent of a debris flow has lower shear rates compared to the center, which allows larger particles to deposit (Costa 1984; Coussot and Meunier 1996; Iverson 2013). The coarser-grained, highly permeable head of a debris flow (Figure 2.1) deposits first and acts as a dam that contains the remaining finer-grained, liquefied flow (Iverson 2013). An identifying feature of a debris flow deposit is a broad range of particle sizes with a fine-grained matrix surrounding large particles (Costa 1984; Coussot and Meunier 1996).

2.2 Debris Flow Mitigation

Designing for debris flow mitigation requires consideration of factors such as debris flow frequency, debris flow volume, solid particle gradation, runout distance, potential flow paths, impact forces, and deposition angle. Appropriate mitigation methods can be determined based on these parameters (Van Dine 1996) and applied as either hillslope or channel treatments. Hillslope treatments are applied on a large spatial scale and are designed to reduce runoff and increase infiltration, whereas channel treatments are most commonly deployed in the vicinity of infrastructure to capture debris within a potential debris flow channel (Santi et al. 2006; Mizuyama 2008; Wendeler et al. 2008 Santi 2012; Ng. et al. 2014; Choi et al. 2015). Successful mitigation strategies entrap debris as the material moves downslope to prevent an increase in debris flow volume due to subsequent channel erosion and entrainment (e.g., Costa 1984; Iverson 1997; Santi et al 2006; deWolf et al 2008; Santi 2012).

2.2.1 Hillslope Treatments

2.2.1.1 Seeding

Seeding is conducted to rapidly establish vegetation on a bare slope to prevent runoff and erosion (Santi 2009). Seeding is used as a mitigation technique for newly constructed slopes or in burned areas, and commonly is used in combination with other methods (e.g., mulching) since seeding is ineffective until vegetation develops (Napper 2006). The presence of vegetation also increases infiltration and provides a protective layer above the soil to reduce raindrop impact. Seeding most commonly is prescribed for slopes ≤ 37^{o} (deWolf et al. 2008) and is applicable up to rates of approximately 40 lb of seeding per acre (Santi 2006). Challenges of seeding are the loss of seeds via wind and rain prior to establishing vegetation.

2.2.1.2 Mulching

Mulching is a method by which mulch (e.g., hay, wood chips, etc.) is applied to the surface of a slope to mitigate against runoff and erosion. This technique commonly is used following wildfires to provide ground cover and protection when seeding is used. The presence of mulch on the soil surface reduces raindrop impact, helps hold surficial soil in place, and creates an interface between overland flow and the soil surface. Mulching can help maintain adequate soil moisture and temperature to promote vegetative growth (Napper 2006). Mulching is effective on slopes up to 33° and is most effective as an erosion protection method when applied with a uniform thickness or percent ground cover (deWolfe et al. 2008).

Mulching is effective when applied to suitable sites and is directly related to the amount and quality of ground cover achieved (Santi et al 2006; deWolf et al. 2008). Mulch can be applied aerially from a helicopter to cover large areas or distributed manually for smaller areas. Effective coverage for mulching has been reported to be at least 40-50% of the ground surface, and U.S. Forest Service recommends application of 0.22 kg/m^2 (2 tons/acre) (Santi et al 2006).

The challenge of applying mulch aerially is difficultly in achieving an even distribution, which can leave select areas exposed and create additional challenges for revegetation (Santi 2009).

2.2.2 Channel Treatments

2.2.2.1 Lateral Walls

Lateral walls are structures installed parallel along a desired flow path to constrain a debris flow to a specified route or to direct a flow away from unstable ground or infrastructure (Van Dine 1996; Napper 2006). These walls can be constructed as earthen berms or concrete walls (Van Dine 1996) and commonly are installed along the steepest part of the slope and/or where the flow path is known. Deflection berms lengthen the flow path, decrease overall gradient, and encourage debris deposition. The anticipated maximum discharge volume and debris flow depth are important factors for lateral wall design such that the debris flow does not overwhelm and destroy the walls (Van Dine 1996).

2.2.2.2 Log Erosion Barriers

Log erosion barriers provide a physical barrier to runoff that reduce rill erosion, increase infiltration potential, and decrease debris flow velocity to encourage debris deposition (Van Dine 1996). This technique involves securing logs in a staggered pattern perpendicular to a hillslope. Logs used for these erosion barriers commonly are 150 to 300-mm diameter by 3 to 10-m long, and the U.S. Forest Service recommends using 40 logs/acre (Santi et al 2006). Small catchment basins develop behind the logs that catch eroded sediment. Spacing between adjacent barriers decreases as the slope steepens to maintain barrier effectiveness (Santi et al 2006), and in general, log erosion barriers are not applicable for slopes greater than 22^{o}. Additionally, heavy rains or slopes with highly erodible soil can create conditions that overwhelm log erosion barriers (deWolf et al. 2008; Santi 2009).

2.2.2.3 Check Dams

Check dams can be composed of reinforced concrete, timber, straw bales, or steel rock-filled cribs (e.g., gabions) and are constructed as a physical barrier perpendicular to the direction of a debris flow (Napper 2006; deWolf et al. 2008). Check dams can be constructed in sequence along a potential flow path to enhance mitigation effectiveness, and the spacing between check dams depends on the slope, dam height, and deposition angle of the sediment (Van Dine 1996). The accumulation of sediment behind a check dam decreases the slope angle and in turn decreases peak flow velocity (Napper 2006). Additionally, the deposited material provides a layer of protection for the channel and the lower flow rate reduces scour along the bottom and sides of the channel (Van Dine 1996; Santi 2006). Check dams have documented success when installed on mild slopes (< 5%) located high in a given watershed (Napper 2006). However, accumulated debris is not removed from check dams after a flow event, which can limit their effectiveness to provide long-term debris flow mitigation (deWolf et al. 2008).

2.2.2.4 Debris Basins

Debris basins are large-scale check dams constructed across a debris flow path and are designed to retain debris from single flow events (Van Dine 1996; Santi et al 2006). Debris basins are most effective when used on large debris fans with low gradients. However, debris basins must be cleaned out after each flow (deWolf et al 2008). The large amount of space required to construct a debris basin combined with maintenance following a given debris flow event, makes these structures a last resort for debris flow mitigation (Napper 2006).

2.2.2.5 Debris Racks

Debris racks are similar to debris dams, but constructed or timber, steel pipes, or high tensile ring-nets that trap and retain coarse debris while allowing finer material and water to pass through (Napper 2005; Napper 2006; deWolf et al 2008). These barriers are used for

small- to medium-sized flows and are typically installed in locations to keep culverts, bridges, and other infrastructure free of debris (deWolf et al 2008). Rack dimensions are designed to accommodate the volume of debris expected per flow event (Napper 2006). Debris collected behind a debris rack must be removed following to restore mitigation effectiveness.

2.3 Flexible Ring-Net Barriers

Flexible ring-net barriers are constructed perpendicular to a hillslope or direction of anticipate debris flow and are designed to inhibit flow and retain material. A schematic of a flexible ring-net barrier that would be observed in the direction of the anticipated debris flow is shown in Figure 2.2. A ring-net barrier consists of loosely-connected, high tensile-strength, steel-wire rings or mesh that is supported by steel wire ropes anchored to the ground (DeNatale et al 1999; Roth et al. 2010; Canelli et al 2012; Brighenti et al 2013; Escallion and Wendeler 2013; Volkein et al. 2011; Volkein et al. 2015). The open, freely-draining properties of the steel rings or mesh allow water and small debris to pass through the barrier, which increases retention capacity and reduces build-up of pore water pressure behind the barrier (Wendeler 2006; Ashwood and Hungr 2016). Installation of ring-net barriers contributes minimal site disturbance since structural support develops from wire ropes secured to ground anchors instead of heavy foundations (Ashwood and Hungr 2016).

Flexible ring-net barriers have an advantage over other mitigation structures as they are light-weight and require minimal space for installation. These attributes make ring-net barriers ideal structures for installation in remote locations (Sasiharan et al. 2006) and along transportation corridors where right-of-way and zoning issues constrain design possibilities for hazard mitigation structures (Wendeler et al. 2008). Additionally, the flexible nature of the barrier slowly transfers impact forces to ground anchors, which reduces the magnitude of the impact forces (Von Boetticher et al 2011; Volkwein et al. 2015). Existing barriers have been shown to withstand earth pressures ranging from 60 to 180 kN/m^2 (Geobrugg 2016) and impact forces up

to 8000 kJ (Escallon and Wendeler 2013; Volkwein et al. 2015). Roth et al. (2010) reported that flexible barrier systems were effective in mitigating large erosion events and that retention capacity of the barrier system can be restored by removing accumulated debris.

2.3.1 Ring-Net Structure

The ring-net structure consists of loosely-connected wire rings held in-place by cables extending from one side of the structure to the other (Figure 2.2). The rings commonly are made of ultra-high strength steel wire bundles such that the total strength of the net depends on the number of wire wrappings in a given ring (Escallon and Wendeler 2013). Nets are sized so that 90% of the anticipated particles will be retained (Brighenti et al. 2013; Volkwein 2014). A smaller mesh net can be incorporated in design as an overlay on the ring-net to restrain smaller particles (Brighenti et al. 2013). The loose nature of the rings allows the entire ring-net barrier to deform when impacted from a debris flow (Escallon and Wendeler 2013).

Steel support cables act to keep the ring-net structure in-place and are the main load bearing components to transfer load from the debris flow to the ground anchors. Cables are installed horizontally and evenly distributed along the barrier height (Figure 2.2). The number of cables depends on the anticipated loads and design height of the barrier (Brighenti et al. 2013; Volkwein 2014).

2.3.2 Braking Elements

Braking elements are connected to each support cable and are usually located adjacent to an anchor. A commonly-used braking element is shown in Figure 2.3, which includes an aluminum tube formed into a circle through which the steel cable passes. The aluminum loop deforms as the barrier is loaded, which allows the debris flow to decelerate and reduces the magnitude of the impact load (Wendeler 2006; Wendeler 2008; Von Boetticher et al. 2011; Brighenti et al. 2013; Volkwein 2014). The number of braking elements in a flexible ring-net

barrier depends on the anticipated loads. After a debris event, braking elements must be checked and potentially replaced (Roth et al. 2010).

2.3.3 Anchors

The purpose of the foundations is to transmit force from the ring-net barrier to the ground. The typical anchors for the barriers consist of ground anchors or and post foundations (Muraishi et al 2005; Wendeler 2007; ETAG027 2013; Ferrero 2016; Maccaferri 2016) and can safely support loads up to 400 kN (Merifield and Sloan 2006, Wendeler 2007; Wendeler 2013).

Typical ground anchors consist of anchor head, a concrete ground plate, a free anchor length, and a fixed anchor length which is bonded to the ground by grout (De Cock 2008). Anchor lengths are adjusted according to the loads expected from the barrier and the load capacity of the ground (Volkwein 2011). Anchors have flexible heads, which allow the anchors to maintain optimum loading even as the barrier deform and ensure that forces that are not in the effective pulling direction of the barrier are absorbed. Rigid anchors can be damaged by impact loads and are susceptible to bending loads. (Volkwein 2014; Geobrugg 2016; Wendeler 2016). For barriers constructed on rock, grouted rope anchors are sufficient, whereas on barriers on less suitable soil require grouted anchor bolt (Wendeler 2016).

Post foundations consist of a concrete structural block set into soil. Post foundations use three standard foundation designs for typically encountered foundation geomaterials including soil, rock overlain by a thin veneer of soil, and rock. For foundations in colluvial soils, foundations are 2.5 x 2.5 x 2.5-foot concrete blocks with steel anchor bolts set into the concrete or drilled and grouted after the concrete has cured. For foundations on a thin layer of soil overlaying rock, the concrete block extends the depth of the soil, and then grouted steel anchor bolts extend past into the rock. If the anchor is in rock, then the concrete block can be reduced to a small slab, with grouted anchor bolts extended below. Typical anchors extend 1 m – 2 m

into the rock depending on strength properties of rock and the expected barrier loads (Burtz 2003).

2.3.4 Loading Mechanisms

A schematic of the sequential surge loading process that commonly impacts flexible ring-net barriers is shown in Figure 2.4. The first impact load is the head of the debris flow hitting the barrier. The dynamic nature of this first load transitions to a static load as the material is brought to a stop. Following the first impact load, a second debris flow surge will impact the barrier via flowing over the previously deposited material from the first surge. This sequential process of dynamic loading in surges repeats until the barrier is full and begins to over top (Wendeler 2006; Wendeler et al. 2007; Brighenti et al 2013; Volkwein et al. 2011; Volkwein et al 2014; Ashwood and Hungr 2016). After some time, the mass behind the barrier has suitable strength to retain the incoming debris giving the barrier a maximum retained volume (Wendeler 2006).

Impact loads and static forces on flexible ring-net barriers can be determined via empirical relationships with predictive parameters that include debris volume, peak velocity, flow depth, front density, and impact time (Roth et al 2010; Von Boetticher et al 2011; Brighenti et al 2013; Volkwein 2014; Volkewein et al 2014; Ashwood and Hungr 2016). Other important characteristics include particle size distribution, water content, and channel geometry (Roth et al. 2010; Volkwein 2014).

2.3.5 Current Design Practices

Current design methods for flexible barrier mitigation systems rely on empirical methods, engineering judgment, and experience (Sasiharan et al. 2006; Volkein et al. 2015). However, application of one barrier design to a different site often results in over and under design of structural strength or debris retention capacity, as each site requires unique barrier heights,

capacities, and earth retention infrastructure (Volkein et al. 2011). Recent experimental and numerical studies have documented that key aspects to avoid barrier failure include a strong anchorage system, strong lateral wires and up-slope support connections, energy absorption capabilities, protection against abrasion, and suitable retention volumes (Roth et al. 2010; Volkein et al. 2011; Canelli et al 2012; Brighenti et al 2013; Volkein et al. 2015). However, this collection of research does not provide guidance on model parameterization for design of a flexible barrier system or develop practical tools such that transportation personnel and other practitioners can readily design flexible barrier systems for site-specific conditions.

2.4 Finite Element Analysis

Finite element analysis (FEA) is a numerical method to transform a set of differential equations into a set of algebraic equations that can be solved via three steps: (i) breakdown, (ii) assembly, and (iii) solution. The breakdown step deconstructs a geometrically complex domain into more simplistic subdomains or elements. Each element can be defined by nodes at which a set of mathematical expressions is solved for a given problem. The accuracy of a given FEA can be increased via additional elements; however, computation time will also increase as the number of elements increases.

Linear approximations of a governing equation are created and applied to each element, and each element is individually analyzed to develop a stiffness matrix. The general system of equations follows the format $[K]\{u\} = \{F\}$ where [K] is the stiffness matrix, {u} is the nodal vector and {F} is the force vector. After individual element stiffness equations have been developed, they must be assembled together to form a global matrix. The global matrix must maintain compatibility of nodal displacements and force equilibrium at each node. This is done by adding individual element matrices together. Lastly, initial and boundary conditions are imposed. Once the global stiffness matrix and nodal and force vectors are constructed, the entire domain is represented by a system of equations that can be solved. The advantage of

FEA is that a solution can be represented by the approximation equations, capturing the local effects of each element. Discretization of the domain into elements allows for simple and accurate representation of complex geometries and dissimilar material properties.

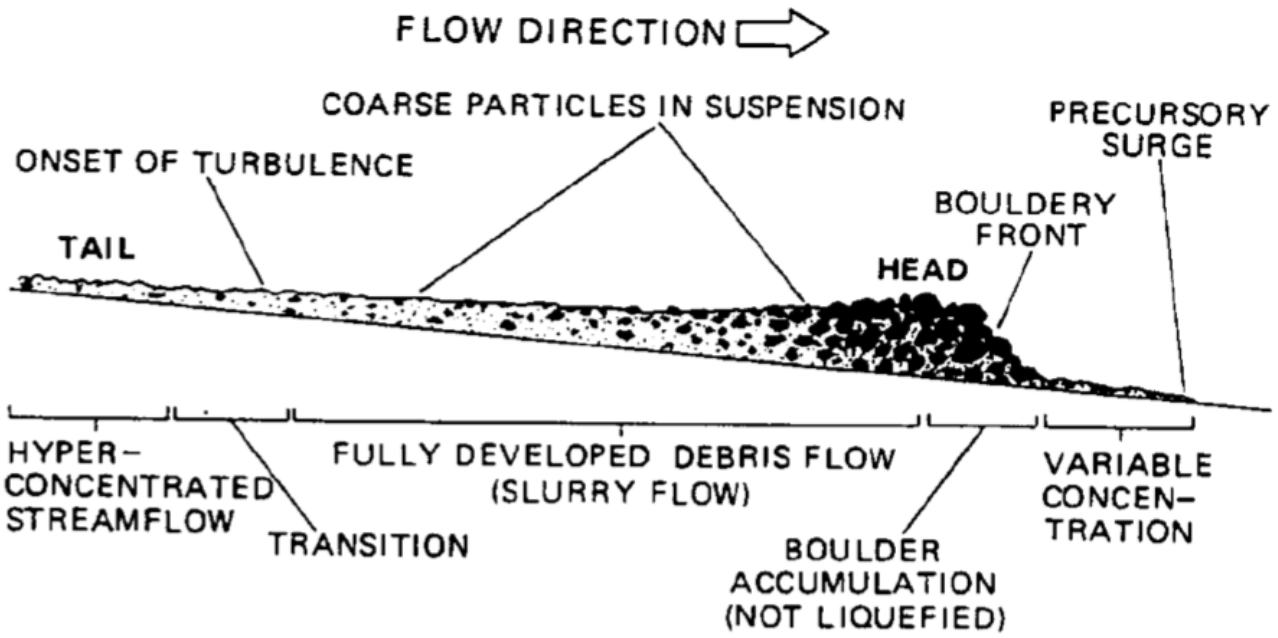

Figure 2.1 Cross-sectional schematic of a typical debris flow. The front of the flow contains larger soil particles interacting through particle-particle contact, and the tail consists primarily of the fluid phase with some suspended particles (Hungr 1999).

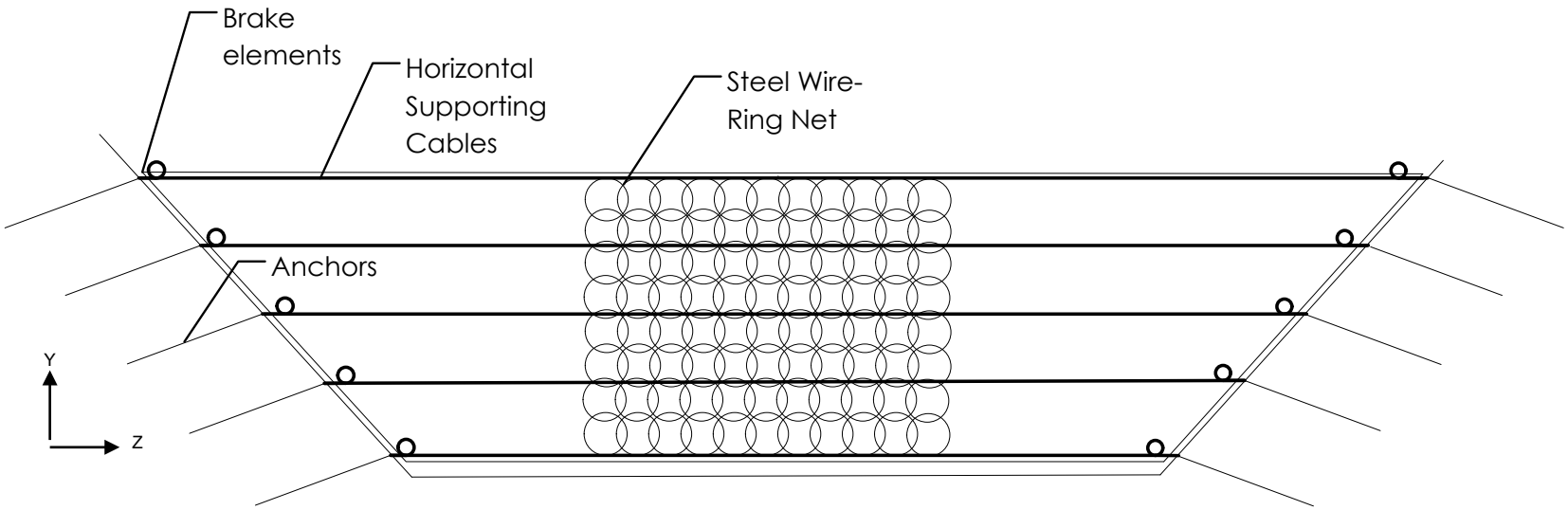

Figure 2.2 Schematic of a flexible ring-net barrier shown perpendicular to the anticipated flow path. The steel ring-net extends the width of the barrier and support cables are evenly spaced vertically.

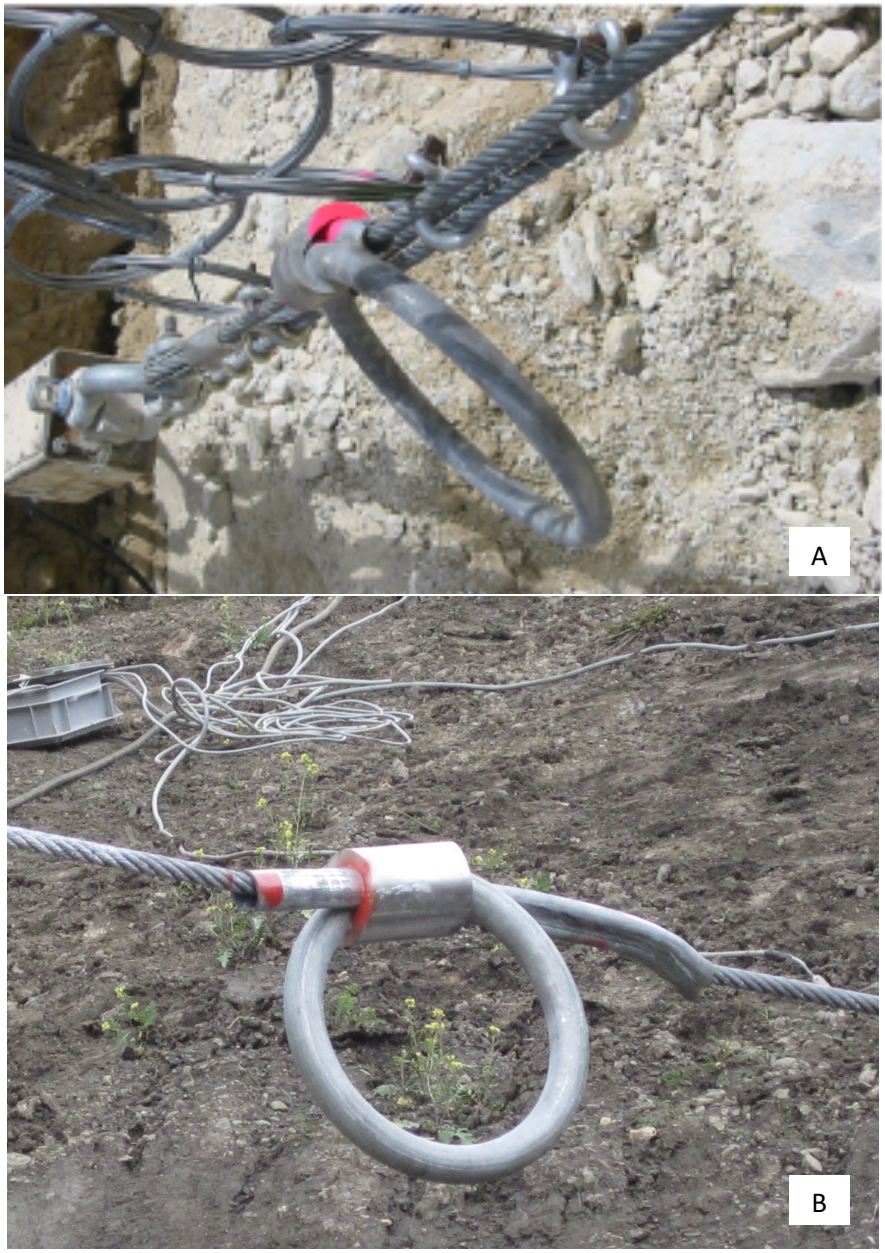

Figure 2.3 Photograph of an (a) undeformed brake element located on horizontal support cable (Wendeler et al. 2008). The aluminum sheath yields as the cable is stressed, allowing the cable to elongate, shown in (b).

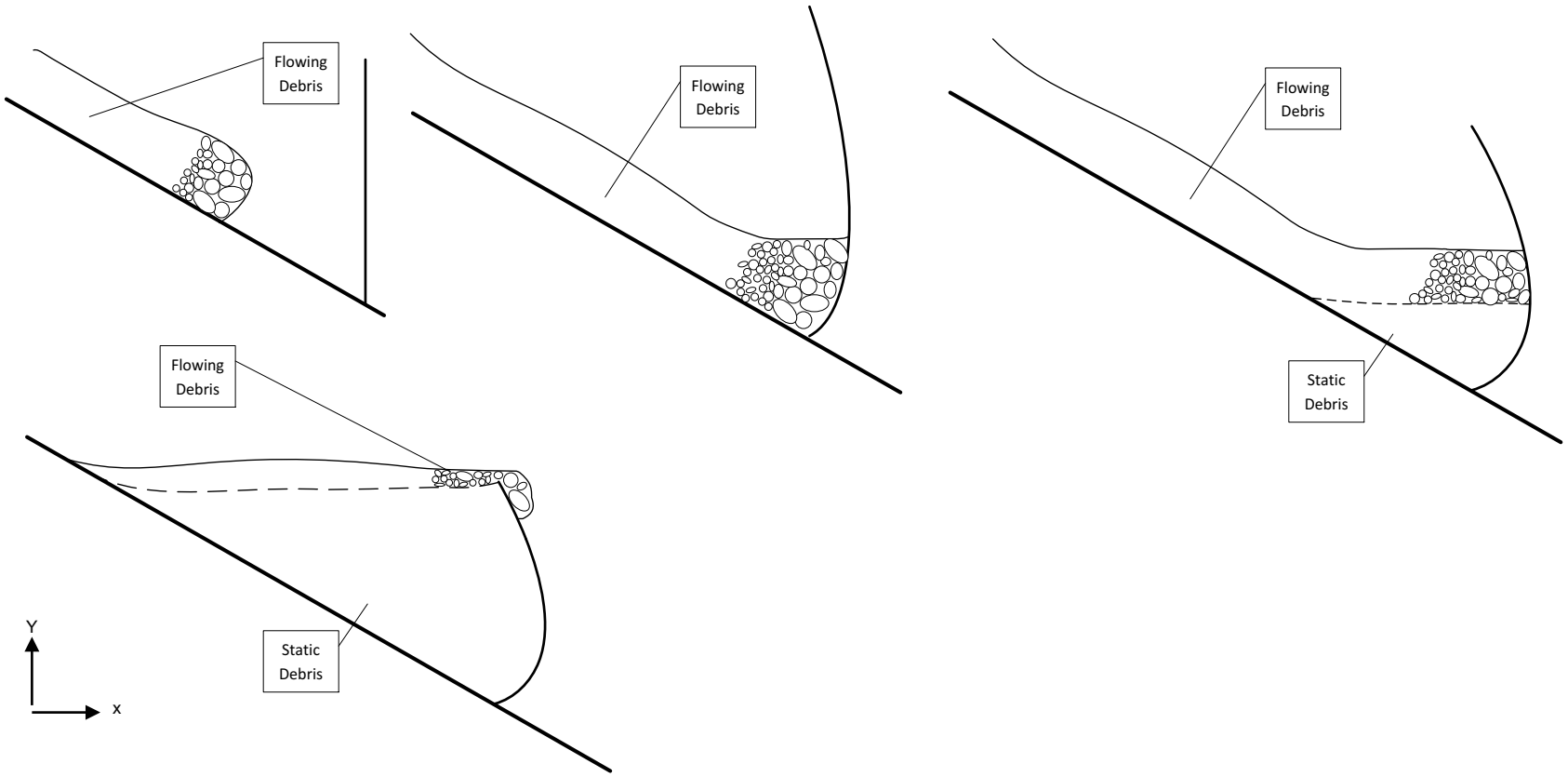

Figure 2.4 Schematics of a flexible ring-net barrier with different loading phases that develop during a debris flow: (i) debris flow impacts the barrier as a dynamic load; (ii) pore pressures in the flow drain through the permeable barrier and the load becomes static; (iii) a subsequent debris flow impacts the barrier that deposits on the existing debris; and (iv) storage capacity of the debris flow barrier is exceeded that allows material to overtop.

CHAPTER 3: MATERIALS AND METHODS

This study was conducted in two phases: (1) model verification via simulation of a full-scale experiment of a flexible ring-net barrier and (2) model assessment via parametric study. Data and information for a full-scale experiment were obtained from Ferrero et al. (2015) and used to verify the FEA conducted in ABAQUS. Comparisons were made between barrier deformation and cable tension measurements from the experiment. A key objective of the first phase was to develop and verify a new ABAQUS model of a flexible ring-net barrier. The parametric study incorporated the same ring-net barrier and was conducted to assess the influence of geotechnical and structural parameters on barrier response during loading. The results of the study were analyzed to determine which variables had an effect on the stresses in the cables and the final barrier deformation.

3.1 Field-Scale Experiment

A field-scale experiment described in Ferrero et al. (2015) was used to assess the debris flow barrier developed in ABAQUS via comparison to field data and an analytical model. A cross-section schematic of the field-scale experiment is shown in Figure 3.1. Details were available on design parameters of the flexible ring-net barrier and properties of the debris flow (Ferrero et al. 2015). In addition, Brighenti et al. (2013) developed an analytical model to assess barrier response to debris flow loading scenarios, which was subsequently evaluated in Ferrero et al. (2015). Thus, physical measurements and analytical simulations of barrier deformation (i.e., position along the centerline of the barrier) and cable tension were obtained from Ferrero et al. (2015) and used to verify the newly developed numerical model.

3.1.1 Barrier Configuration

The flexible ring-net barrier was located at the bottom of a channel (Figure 3.1) secured on three sides (left, right, and base) with rock anchors and soil nails. A design drawing of the barrier in the direction of flow is shown in Figure 3.2 and a summary of the barrier properties is in Table 3.1. The design drawing in Figure 3.2 was created for the current study and is based directly on the field-scale experiment. The bottom of the barrier was 14.85-m wide and the top was 19.72-m wide. The design height along the centerline was 5.2 m, but the barrier sagged under self-weight to a height of 4 m. The barrier was equipped with five load cells to measure tensile forces at each level of cables and barrier deflection was monitored via a photogrammetric acquisition system (Ferrero et al. 2015).

The barrier include the following structural elements that were considered in development of the finite element model: wire rings, cables, braking elements, and anchors. The five sets of cables were spaced approximately 1.3-m vertically on center, and each set included two parallel cables that spanned the width of the barrier (Figure 3.2). Each cable was a 6x19 steel cable with an ultimate tensile strength of 252 kN. Braking elements were included at the ends of each cable, adjacent to the ground anchors. Each braking element consisted of a 600-mm long aluminum (Al 6060) tube formed into a ring through which the steel cable passed. The braking elements were designed to yield at 60 kN and the combination of dual braking elements on a single cable allowed the cables to elongate up to 2 m when loaded. The flexible ring-net consisted of two superimposed metal ring nets. The primary net consisted of circular interlocking rings with a diameter of 0.35 m and acted as the main component for retaining debris. A secondary net was composed of hexagonal elements with an inscribed diameter of 0.08 m and retained finer debris while adding negligible strength to the structure. The secondary net was omitted from the finite element model as the simulated flow was large enough to be retained by the primary net.

3.1.2 Debris Flow Properties

The field site consisted of a 43-m long by 2-m wide channel at a slope angle of 40° (Figure 3.1) that expanded in width near the barrier The barrier was installed at the bottom of the channel, which also coincided with a change in ground slope from 40° in front of the barrier to approximately horizontal in back of the barrier. Properties of the debris flow are tabulated in Table 3.1. The debris was loose material ranging in particle size from 0.1 m to 1.5 m in diameter, with a total volume of 400 m^3 and an average total density was 1790 kg/m^3. The experiment initiated with debris released into the channel at the top of the 40° slope (Figure 3.8), The sudden release of material simulated the surge effect observed in a natural debris flow. A maximum flow velocity of 9 m/s and average flow velocity of 2.51 m/s were recorded during the experiment (Ferrero et al. 2015).

3.1.3 Analytical Model

The analytical model presented in Brighenti et al. (2013) was developed assuming (i) the debris flow force was equally distributed along the length of the support cables and applied normal to the net structure and (ii) the support cables were in equilibrium under large displacement. Dynamic pressure applied to the barrier was derived from Bernoulli's theorem and static pressure was calculated based on lateral earth pressure theory. The flow height, coefficient of earth pressure, mass density of flow, and angle of slope were considered in calculation of the impact pressures.

The total horizontal load on each cable was calculated based on cable height, and debris flow properties. An indirect load from deformation of adjacent cables on a given cable was also taken into account (Brighenti et al. 2013; Ferrero et al. 2015). Cable deformation in the positive x-direction as show in Figure 3.1 was calculated based on barrier properties and the total load on each cable. Finally, the tensile force, total elongation, and reaction forces were calculated based on the predicted cable deformation and stress-strain properties of the cables.

3.2 Finite Element Model

A three-dimensional (3D) finite element model was created in ABAQUS/Explicit 6.14 (Dassault Systèmes), which is capable of simulating high-speed dynamic events and large, nonlinear, quasi-static analyses, such as a mass impacting a flexible structure (SIMULA 2005; Gentilini et al. 2012). Abaqus/Explicit is efficient at solving highly discontinuous, high speed, dynamic problems. Additionally, the contact algorithm does not add any degrees of freedom, which keeps disk space small comparable to ABAQUS/Standard (SIMULA 2005).

The model contained 17042 elements and 55195 nodes, and was composed of 3D beam elements, 3D truss elements, axial connectors, and rigid bodies. The model was discretized into 11 steps and ran for 8.5 seconds; i.e., until velocity of the debris flow was 0 m/s. Outputs were collected every 0.2 s.

3.2.1 Finite Element Model Components

The finite element model is composed of two main components – the barrier and the debris flow. The barrier consists of support cables running horizontally across the barrier, braking elements connecting to the ends of each support cable, and series of interlocking rings which span the entirety of the barrier. The debris flow consists of a series of small blocks.

3.2.1.1 Support Cables

Cables were modeled as two-node, linear, 3D truss elements with a global element size of approximately 0.39 m and total number of elements ranging between 38 and 51 per cable (i.e., element number increased with cable length). The length of each set of cables increased with vertical position in the barrier and all were modeled with a 1.3-m vertical spacing (Figure 3.2). All cable sets included two cables; the lower four sets were spaced 10-mm vertically and the top set was spaced 5-mm vertically to ensure that both cables passed through the top row of rings. Each cable had a 20-mm-diameter cross section and a total of two braking elements - one

located at each boundary node. Steel properties selected for the cables included density = 7850 kg/m^3, Young's Modulus = 8.27 x 10^{12} N/m^2, and Poisson's Ratio = 0.3 (U.S. Navy 1976). Plastic deformation behavior of the cables was ignored as the cables were assumed to behave elastically due to tension forces below the ultimate tensile strength of steel (Ferrero et al. 2015, Sakash 2016).

A mesh verification test was conducted on the bottom cable to minimize the number of elements without sacrificing accuracy of the model. A body force of 10,000 kN was applied to the cable for 2.5 s, which allowed deformation to equilibrate and then deformation at the center of the cabled was output from the model. The test was repeated for different mesh densities until the change in deformation was negligible. A cable mesh of 44 elements was chosen to reduce computational time without limiting output accuracy. This mesh spacing was assumed optimal for all cables and was applied to all cables.

3.2.1.2 Braking Elements

The braking elements in the numerical model of the barrier system were simulated as non-linear axial connector elements. A separate FEA of an individual brake element was created to determine the force-deformation relationship to apply to the spring element that represented each brake in the barrier system FEA. Images of the FEA developed for an individual brake element in ABAQUS are shown in Figure 3.6. The brake element was simulated as a 1.5-mm-thick sidewall aluminum tube formed into a 350^o arc with a 300-mm radius (Figure 3.3a). The aluminum was simulated with density = 7200 kg/m^3, Young's Modulus = 68.9 GPa, Poisson's ratio = 0.33, and yield stress = 600 MPa (Matweb 2016). Displacement boundary conditions of 0.4 m and -0.4 m in the Z direction were applied to each end of the arc, which simulated activation of the braking element in the field.

The image in Figure 3.3b depicts a brake element after displacement was applied. The relationship between force and displacement at a node located near the end of the arc is shown

in Figure 3.4. The brake initially exhibited linear deformation and then yields at approximately 60 kN. Once the upper-bound force was reached, the aluminum ring continued to deform the allowable 0.6 m of deformation with no subsequent accumulation of force. The force-deformation behavior shown in Figure 3.4 was anticipated based on the braking elements described in Ferrero et al. (2015) and were used for all connector elements that simulated the braking elements in the barrier system FEA. A stop length of 1 m was assigned to each connector element, which represented the maximum elongation of a brake. The springs representing each brake element were modeled with a cable node on one end and a reference point on the other end. The reference point was assigned a fixed boundary condition and spaced 0.19 m from the cable node to represent the initial diameter of the brake loop.

3.2.1.3 Ring-Net

The ring-net simulated in the barrier system FEA consisted of 1531 individual rings. Each ring was designed to replicate an ultra-high strength steel-wire ring used in flexible ring-net barriers described in Escallon and Wendeler (2013) since information regarding the cross-sectional properties of the wire ring were not provided in Ferrero et al. (2015). The simulated wire ring was fabricated from 3-mm diameter wire wound seven times to create a 0.35-m diameter ring with a 21-mm cross-section diameter. Steel properties for the rings included density = 7850 kg/m^3, Young's Modulus = 210 GPa, Poisson's Ratio = 0.3, and minimum yield strength = 1770 MPa (Escallon and Wendeler 2013). Plastic properties were adopted from Escallon and Wendeler (2013).

Each ring was modeled in the barrier system FEA as a two node linear beam with 10 elements per ring and an approximate element size of 0.125 m. A mesh verification was performed on a section of 19 by 11 rings suspended from the top cable and a concentrated 1-kN load applied to each ring in the bottom row for 5 s. Deflections obtained from this simulation were recorded for a variety of ring meshes and an optimal mesh was determined at the point

when increasing the mesh density had no effect on initial deflection. The optimal mesh was determined to be 10 elements, which corresponded to a mesh spacing of 0.338 m.

The ring-net barrier was created in the FEA with rings loosely interlocked with up to four adjacent rings, which allowed individual rings to move with respect to each other (Figure 3.2). This freedom in movement of each ring simulated the flexible deformation characteristics of the barrier system. All rings overlapped approximately half a ring diameter with adjacent rings and gravity was applied to settle the entire ring-net into place as a first step in the analysis. After the ring-net achieved an at-rest position due to gravity, the bottom row of rings was fixed in space to simulate connection to the bottom cable. A zero displacement boundary condition was assigned to the side cables to represent the interaction between the cables and rings running along the sides of the barrier. This boundary condition allowed movement parallel to the channel sides.

3.2.1.4 Anchors

Ground anchorage systems were not simulated in the barrier system FEA. The anchors were assumed to experience negligible deformation relative to the barrier system and were simulated as a fixed boundary condition. Loads at the anchor nodes were extracted from the FEA following a given simulation for comparison to typical soil anchor data for a range of soils. This comparison was conducted to assess whether the anchor loads agreed with commonly designed ground anchorage systems in practice.

3.2.1.5 Debris Flow

A cross-sectional schematic of the debris flow and barrier system configuration for the FEA is shown in Figure 3.8. The debris flow event was simulated as a series of four surges that successively impacted the ring-net barrier. The debris flow mass was initially positioned 1 m upslope from the barrier and an initial velocity was applied to develop momentum in a given surge to impact the barrier. Each surge was 0.7 m in height to represent the measured flow

height in the field (Ferrero et al. 2013). The initial velocity applied to a flow surge was either 2.51 m/s or 9.0 m/s to capture the average and maximum velocities in the field study. The initial velocity was applied to a given surge every 1.1 s and an additional 3 s of simulation time was included following the final surge to capture full deformation and force development in the barrier. The first second of the analysis is considered the barrier settling period, as the ring-net is falling into place via gravity. The barrier settling period is not representative of any loading scenario and is not considered part of this analysis. All temporal results are consider 1 s to 8.5 s of simulation time. The final simulation time was 8.5 s and was defined through trial and error to be short enough to reduce computation time and long enough to allow the simulated debris flow to achieve a final velocity of zero.

Screenshots of the debris flow and ring-net barrier simulated in the FEA are shown in Fig. 3.6. The debris flow was modeled as a solid mass discretized into rectangles. The entire flow had a length of 8.7 m, width of 15 m, and height of 2.8 m (perpendicular to the slope). The front of the flow was simulated to have a vertical face (i.e., 50° from the channel slope) such that the debris face was parallel to the ring-net. The flow material was simulated with a density of 2260 kg/m^3 to approximate the mass of the debris flow in the field experiment. Young's modulus of the debris flow blocks was 750 GPa and Poisson's ratio was 0.3 to simulate a rigid mass (Gercek 2006).

The front of the debris flow consisted of 308 trapezoidal prisms and the rest of the flow was divided into 0.3-m tall by 0.35-m wide rectangular prisms that ranged in length from 2.0 to 2.6 m. Adaptive meshing was applied to the debris flow during barrier loading. This discretization was adopted to simulate the desired impact force on the ring-net barrier without increasing the computational cost of the model. Thus, the focus of the barrier system FEA was to simulate structural response of the barrier and not to simulate flow behavior of the debris flow. This simplified flow simulation was anticipated to be effective in capturing general behavior

of the barrier, which could later be expanded with more complex simulations of debris flows that can provide a variation in loading (Ashwood and Hungr 2016).

3.2.1.6 Flow Channel

The debris flow channel was modeled as a meshless analytical rigid shell. The channel surface was 15-m long, 20-m wide, and sloped 40° from the horizontal (Figure 3.5 and Figure 3.6). The channel sides were 5.5-m tall sloped 40° from horizontal and rotated 124° from the vertical axis. This positioning aligned the channel sides with boundary nodes of the cables.

3.2.2 Contact

A general contact algorithm was used to assign contact properties to the different components simulated in the model. Steel-steel interactions were a global property assignment, whereas steel-soil and soil-soil contacts were assigned individually. The steel-steel friction coefficient was 0.25 (Escallon and Wendeler 2013) and steel-soil friction coefficient was 0.25, corresponding to typical friction angles of silty sand, gravel, or sand mixed with silt or clay on steel (Fine 2016). A friction coefficient of 0.578 was given to soil-soil contact, corresponding to an internal angle of friction = 30^{o}, which is a typical friction angle of debris flows (Hungr 1995; Iverson 1997; Bringhenti et al 2013; Calvetti et al 2013) and was also used in the analytical model (Brighenti et al. 2013). A master-slave assignment was given to the soil-steel interaction, with the impacting soil as the master and the ring-net barrier as the slave.

3.3 Parametric Study

A parametric study was conducted to evaluate how debris flow characteristics and barrier properties influence the structural response of the flexible ring-net barrier. The following five variables were selected: (i) debris flow velocity; (ii) debris flow density; (iii) individual surge height; (iv) number of ring windings; and (v) number of brakes per cable. The first three

variables, velocity, density, and surge height of the debris flow, captured general characteristics of debris flows that can be expected to vary during the lifespan of a given barrier system. The last two variables focused on structural variables that may be considered in design.

3.3.1 Debris Flow Velocity

Calvetti et al. (2015) reported that the maximum impact force is a critical parameter for the design of flexible barriers. The primary variable that affects maximum impact force is the debris flow velocity. The flow velocity can be directly related to a variety of debris flow parameters (e.g., lower friction angle or steeper channel slope will increase flow velocity), and therefore, the influence of velocity on the barrier is relevant to an array of parameters that can affect flow velocity. The initial velocity of each surge was varied incrementally from 0.5 m/s to 12 m/s, which encompasses a range of reported debris flow velocities (Costa 1984; Coussot and Meunier 1996).

3.3.2 Debris Flow Density

The density of a given debris flow will impact the load generated on a barrier when velocity is held constant. An increase in density will result in greater momentum and larger impact forces. Characteristics such as debris composition, porosity, water content, specific gravity, and flow volume can influence the density of a debris flow. Density was varied between 1900 kg/m^3 and 2350 kg/m^3 to capture a typical range of debris flow density (Coussot and Meunier 1996; Iverson 2007).

3.3.3 Surge Height

The height of an individual surge was varied to evaluate the influence of impact area between the debris flow and barrier has on structural response of the barrier. Typical debris flow heights range from 0.8 m to 2.8 m (Wendler 2006; Wendler 2008). The debris flow surge height

ranged from 0.7 m to 2.8 m. As the surge height was altered, the overall flow height remained the same. Thus, varying flow height resulted in a change in the number of flow surges.

3.3.4 Number of Windings per Ring

The wire rings are the main component of the flexible ring-net barriers. Each ring is constructed from an individual wire wound multiple times to form a ring with a specified diameter. An increase in the number of windings will increase the overall ring thickness (i.e., cross-sectional diameter) (Escallon and Wendeler 2013). The cross-sectional diameter of a given ring was varied from 0.0075 m to 0.018 m, representing 5 to 12 windings, to assess the effect of ring thickness on structural response of the barrier.

3.3.5 Number of Brake Elements per Cable

Braking elements are included in a ring-net barrier system to dampen impact loads and provide flexibility to the structure. These braking elements are positioned on each cable, adjacent to the ground anchors. The number of braking elements is directly proportional to the barrier stiffness, such that an increase in brake elements will result in decreased stiffness (i.e., more flexibility) of the barrier and decreased impact force on the anchors (Leonardi et al. 2014). Increasing the number of braking elements will also increase the amount of potential deformation, which will increase volumetric capacity of the barrier. The number of braking elements on each cable was set equal to 0, 2, and 4.

Table 3.1 Summary of barrier material properties used in the benchmark example.

Barrier Properties		
Width at Base	14.85	m
Width at Maximum Height	19.72	m
Height at Centerline	4	m
Diameter of Cable	20	mm
Formation	6 x 19 + AM	
Strength Class	1770	N/mm^2
Ultimate Tensile Strength	252	kN
Type of Rings	ASM 3-4-350/500	
Ring Nominal Diameter	350	mm
Steel Wire Diameter	3	mm
Wire Strength Class	1380	N/mm^2
Ultimate Tensile Strength	9.5	kN

Table 3.2 Summary of debris flow properties used in the field-scale experiment.

Debris Flow Properties		
Height	0.7	m
Density	1790	kg/m^3
Friction Angle	40	^{o}
Slope Angle	40	^{o}
Flow Velocity	2.51	m/s
Flow Volume	400	m^3
Particle Size	0.1 - 1.5	m

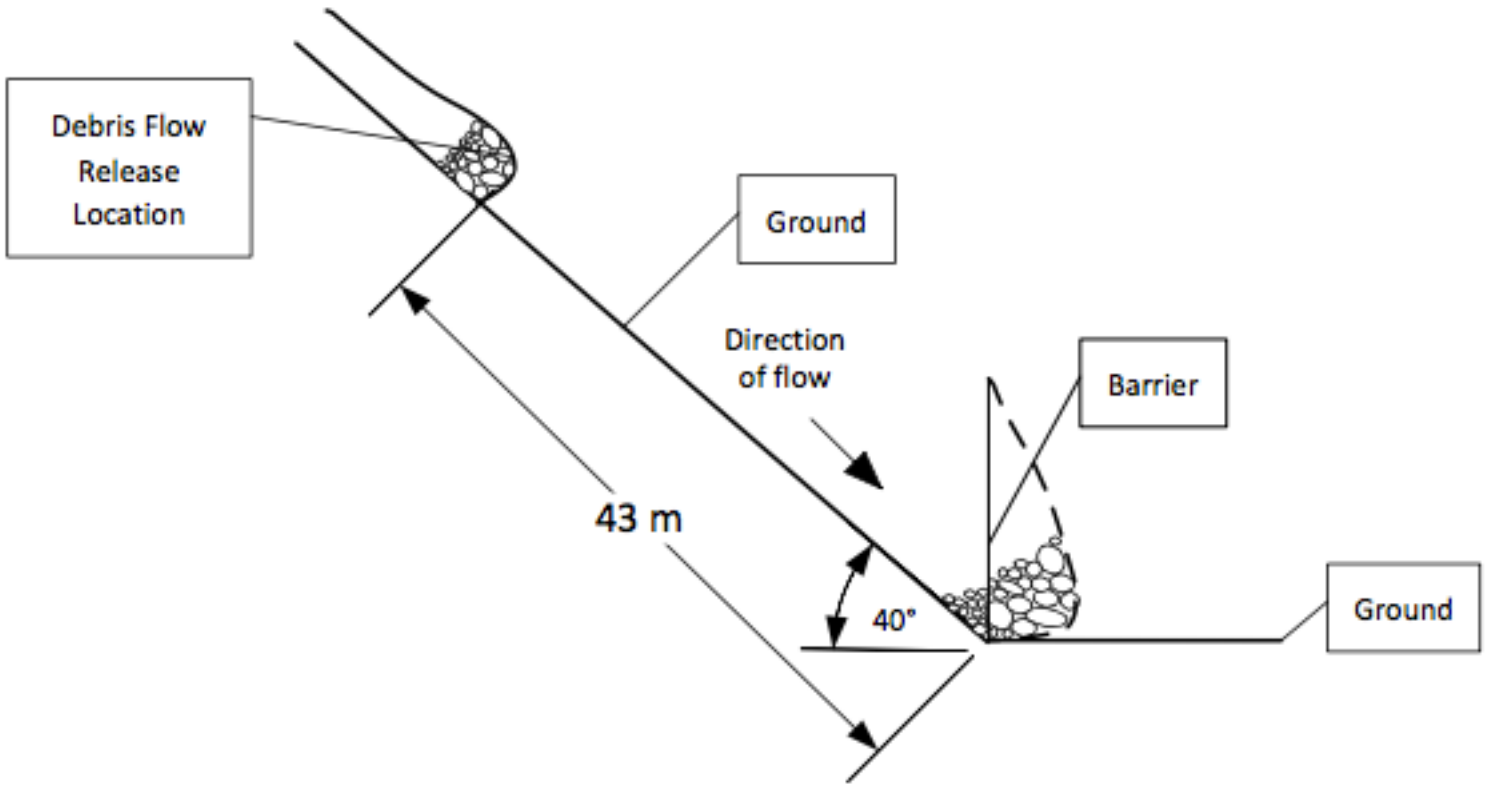

Figure 3.1 A schematic of the field test performed by Ferrero et al. (2015). The debris flow was released 43 m upslope from the barrier. The channel slope was 40° upslope from the barrier, and flat behind the barrier.

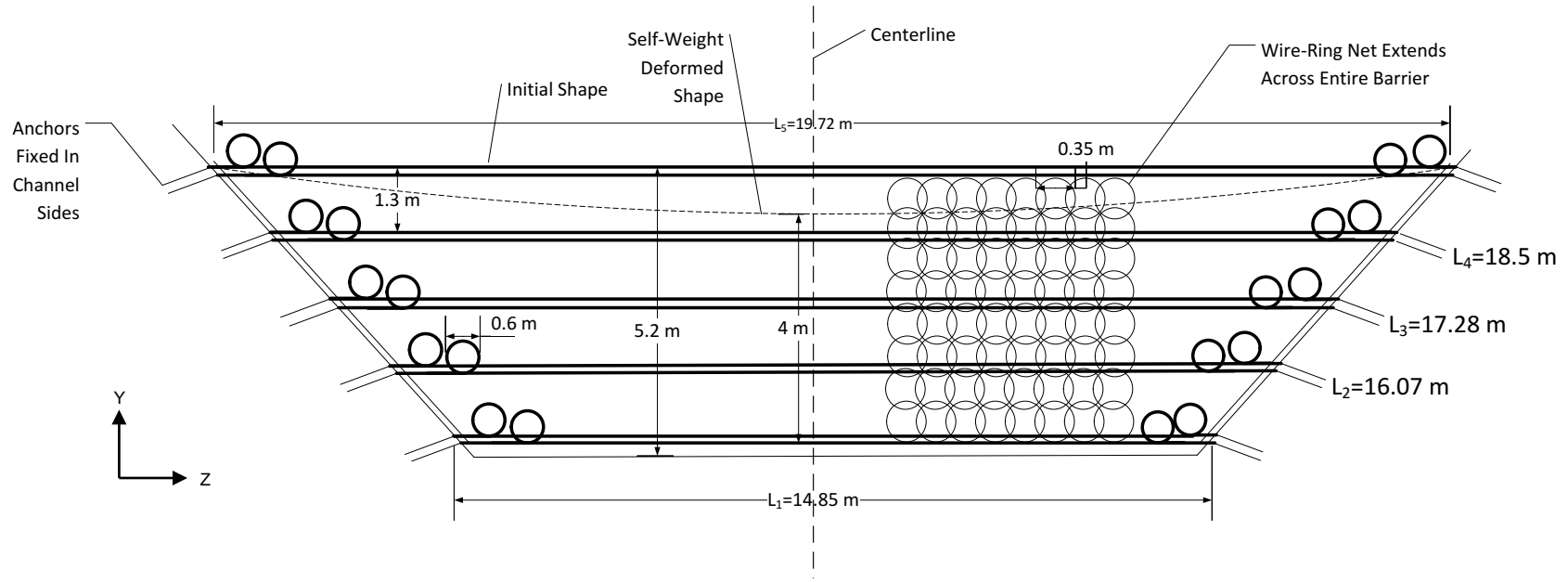

Figure 3.2 Schematic of the barrier used in Ferrero et al. The overall barrier height is 5.2 m and after deformation from self- weight is 4 m. The support cables have two brake elements each, a 1.3 m vertical spacing, with horizontal lengths depicted by L_n . The ring net consists of interlocking rings and spans the entire width of the barrier.

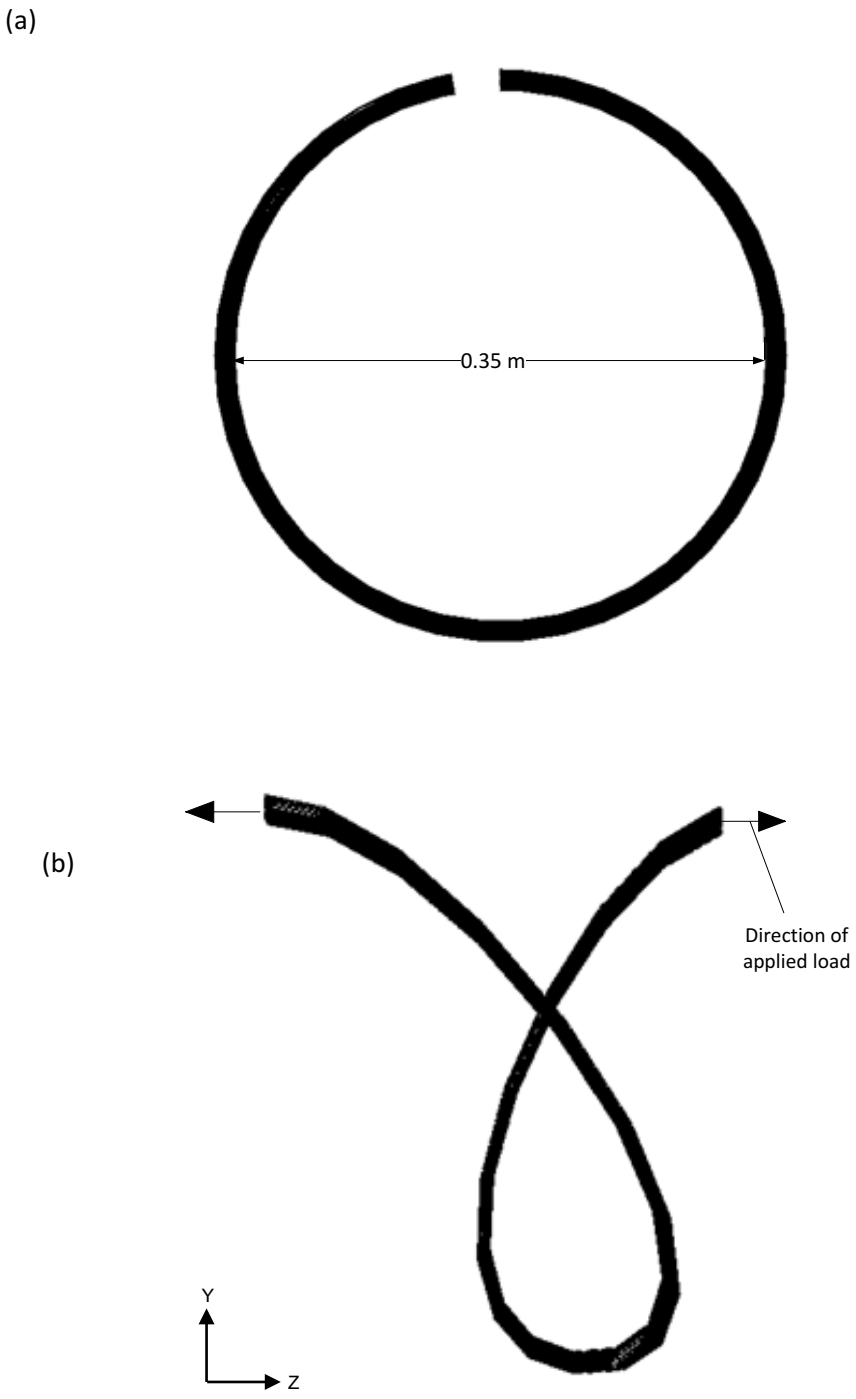

Figure 3.3 A FEA model of an individual brake element (a) before model is run and (b) deformed shape after deformation boundary condition is applied. Results from this model were used to determine force-deformation data to be used in the barrier model.

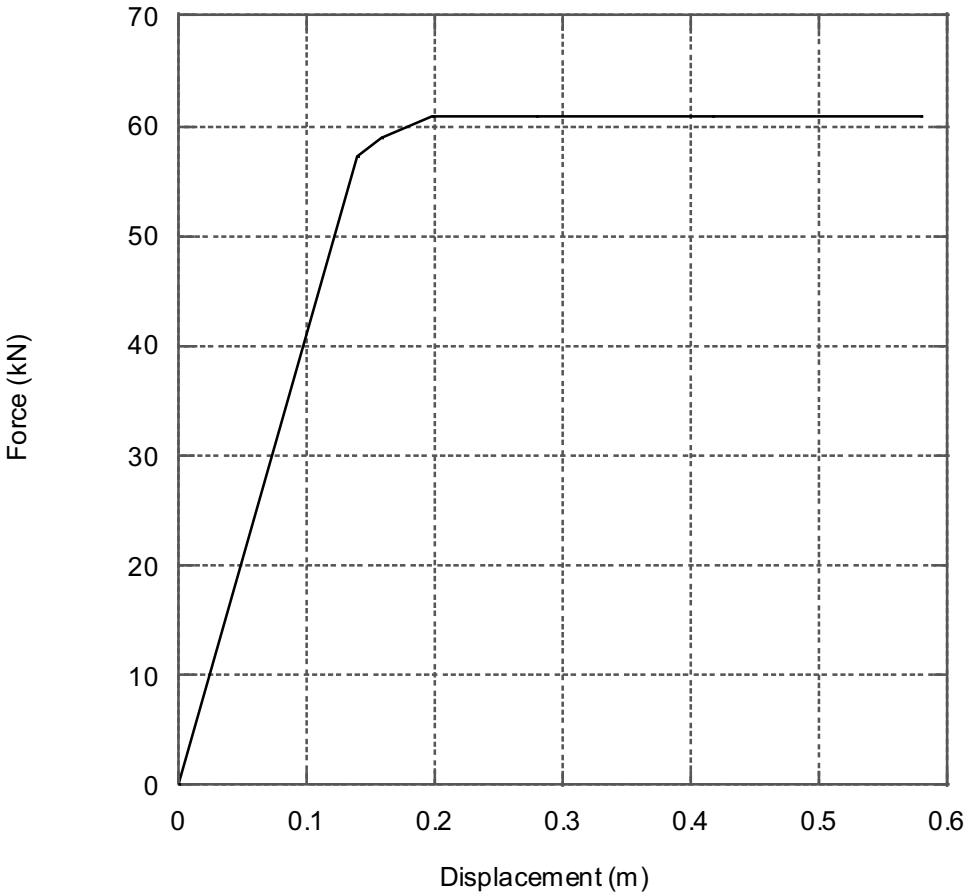

Figure 3.4 Force displacement curve for the brake element model which is applied to the brake elements in the barrier model.

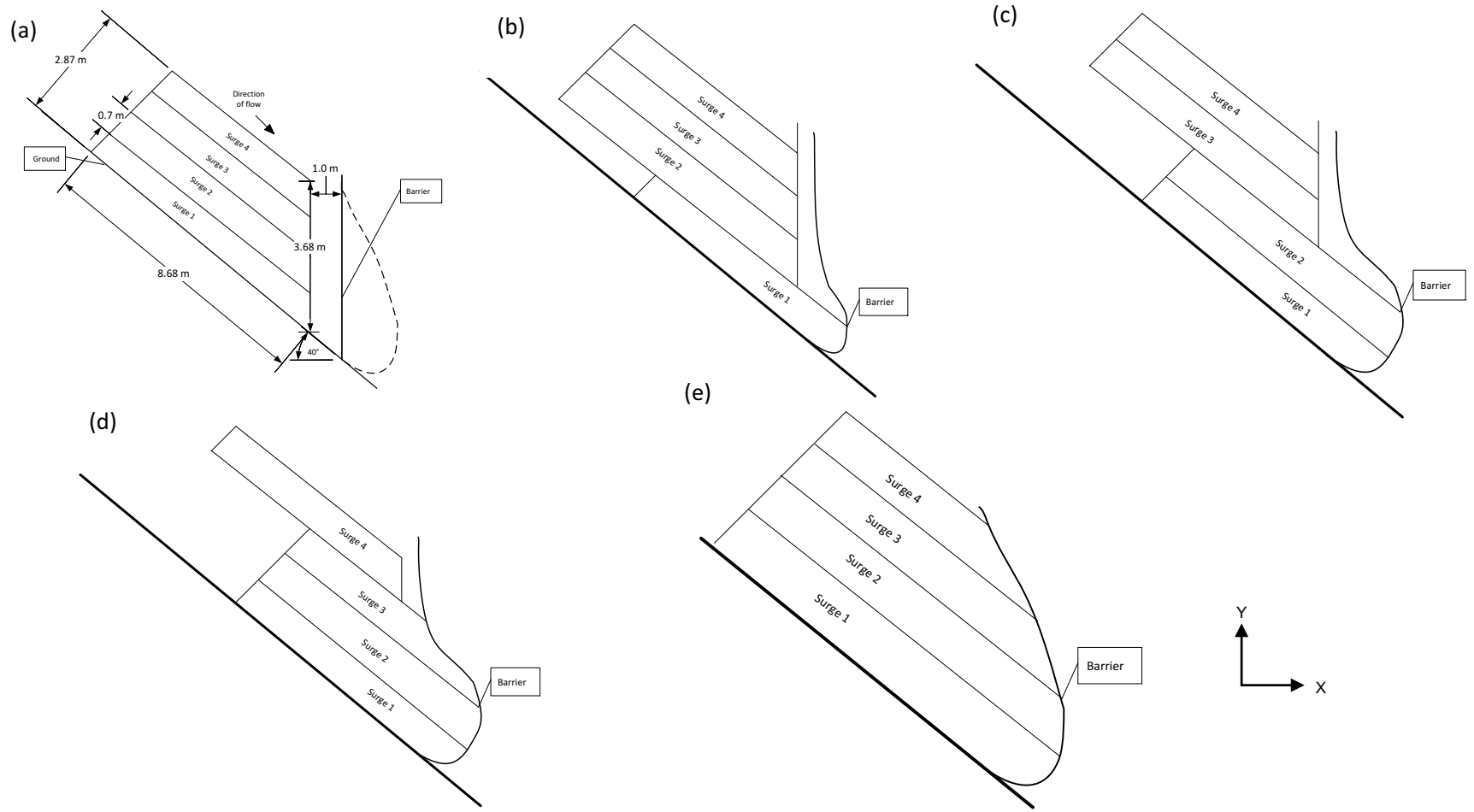

Figure 3.5 A schematic representing how the debris flow was modeled impacting the barrier using surges. (a) shows the initial barrier set up (b) is the initial surge impacting the barrier (c) is the second surge (d) is the third surge and (e) is the barrier after loading is completed.

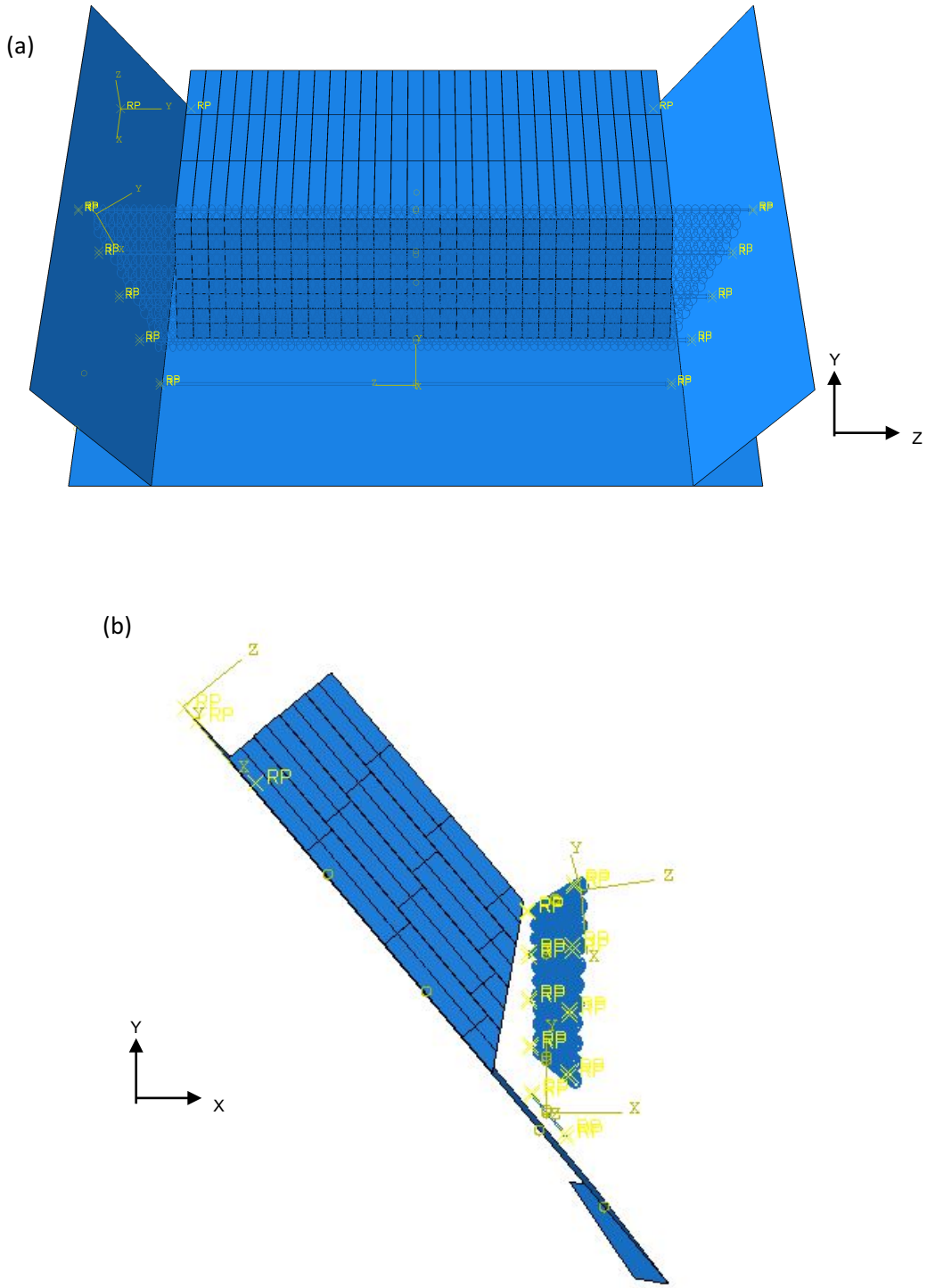

Figure 3.6 Abaqus model assembly showing (a) a front view and (b) a section view of the barrier system and debris flow. The debris flow is discretized into smaller block, shown in both (a) and (b). Each flow surge consists of two rows of blocks.

CHAPTER 4: RESULTS AND DISCUSSION

4.1 Benchmark Example

A schematic of the ring-net barrier with labeled structural components that are referenced throughout the benchmark analysis is shown in Figure 4.1. Cable sets were assigned numbers 1 through 5, with the set number increasing from the bottom cable set to the top of the barrier. Each cable set consisted of two cables labeled a and b, with a identifying the upper cable and b the lower cable of each cable set. Maximum principle stress and deformation in the X and Z directions were obtained for the center node of each cable for the benchmark analysis. Anchor sets were labeled from 1 to 5, which corresponded to cable sets, whereby anchor set numbers increased from the bottom to top of the barrier. Anchors were individually labeled to reference the left (L) or right (R) side of the cable they were attached to (Figure 4.1). For example, Anchor 1aL identifies the anchor on the left side of the barrier that coincides with Cable 1a. Anchors were represented in the model as fixed points and reaction forces were obtained for each anchor. Select rings were labeled A through E that were located at various heights along the center line of the barrier. Deformation in the X and Y directions were obtained for each select ring.

In the field-scale debris flow experiment conducted by Ferrero et al. (2015), horizontal deformation along the centerline of the barrier and cable tension were measured and also predicted with an analytical model (Bringhenti et al. 2013). Measured and predicted horizontal deformations for vertically-spaced locations along the centerline of the field-scale ring-net barrier experiment are shown in Figure 4.2. The magnitude of horizontal deformation at a given location along the centerline of the ring-net barrier increased with time, and the largest deformations were measured near the mid-height of the barrier. Height of the barrier reduced from approximately 4.3 m to 3.6 m (Figure 4.2b) due to pronounced barrier deformation in the direction of flow. Deformations predicted via the analytical model captured the general curved

shape of the deformed barrier, but under-predicted final horizontal deformation by approximately an order of magnitude.

Measured and predicted cable tensions from the full-scale ring-net barrier experiment are shown in Figure 4.3. Temporal variability in magnitude of the measured cable tension was attributed to dynamic loading caused during impact of the debris flow. Cable tensions predicted via the analytical model at cable heights of 1.3 m and 2.8 m generally agreed with field measurements (Figure 4.3). Cables located near the middle of the barrier (z = 2.8 m) had the largest measured and predicted tensions. The positive cable tensions measured at time zero were considered residual tension within the cables attributed to gravity acting on the cables.

The average measured debris flow velocity in the field experiment was 2.51 m/s and the maximum velocity was 9 m/s (Ferrero et al. 2015). For the benchmark analysis, velocities of 2.51 m/s and 9 m/s were used as impact velocities of the debris flow into the ring-net barrier.

4.1.1 Barrier Deformation

A schematic of a deformed ring-net barrier in the FEA is shown in Figure 4.4. Preliminary model assessments indicated that cables occasionally became stuck between the simulated debris flow layers and would not deform with the overall net. Thus, horizontal deformation predicted with the FEA was obtained from individual rings located along the barrier centerline to compare with the field measurements. The model simulation included a continuous slope downslope from the barrier, which was different from the approximately horizontal ground surface downslope in the field-scale experiment (Ferrero et al. 2015). A constant slope was used in the FEA to make the model numerically simpler. However, barrier deformations predicted in the FEA were modified to more appropriately compare with measured deformations. Vertical dimensions in Figure 4.4 identify the barrier height with respect to a datum, which was output via the FEA, and total barrier height from the lowest point of the deformed barrier. Deformation predictions from the FEA were adjusted to represent total barrier

height via re-establishing the datum at the vertical coordinate of Ring A (i.e., lowest ring on the barrier; Figure 4.1).

Predicted deformation along the centerline of the ring-net barrier and adjusted deformations to represent total barrier height are shown in Figure 4.5 for debris flow velocities of 2.51 m/s and 9 m/s. The unadjusted and adjusted barrier deformations show similar deformed shapes; however, overall barrier height increased in the adjusted deformations. The negative vertical coordinates at the base of the barrier following the height adjustment were due to rings above the bottom ring (Ring A, Fig. 4.1) progressing further downslope in the FEA at full deformation. The adjusted barrier heights are used subsequently for all comparisons to measured deformations of the field-scale experiment.

Final deformations along the centerline of the barrier measured in the field-scale experiment, predicted with an analytical model in Bringhenti et al. (2013), and predicted with the FEA in this study are shown in Figure 4.6a. Data from Figure 4.6 are reproduced as normalized barrier heights in Figure. 4.6b. Normalized heights with respect to initial height of the barrier were computed for physical measurements and analytical predictions, whereas the normalized heights for the FEA predictions were computed with respect to the height of the barrier after the settling period (i.e., application of gravitational force). The normalized barrier heights provide a comparison for deformation due only to debris flow loading. Deformations predicted with the FEA for both debris flow velocities (2.51 m/s and 9 m/s) closely represent the deformed shape of the barrier measured in the field. The FEA over-predicts deformation by approximately 0.5 m at a normalized height of 0.2 (Fig. 4.6b) and is a more accurate representation of overall barrier deformation when compared to the analytical model.

Images of the flexible ring-net barrier in the FEA are shown in Figure 4.2 for the following conditions: (a) initial model set-up; (b) end of barrier settling after application of gravity; (c) after the 1st debris flow surge; (d) after the 2nd debris flow surge; (e) after the 3rd debris flow surge and; (f) at the end of the model simulation after the 4th debris flow surge. The deformed shape

predicted via the FEA is consistent with the field study, whereby the largest horizontal deformations were observed near the middle of the barrier (Figures 4.6 and 4.7). Although the FEA overestimated barrier deformation along the centerline, the overestimate is conservative and a more practical prediction for evaluating horizontal deformation for design.

4.1.2 Induced Cable Tension

Temporal trends of cable tension measured in the field-scale experiment, predicted via the analytical model, and predicted via the FEA in this study are shown in Fig. 4.8. Cable tensions predicted in the FEA are in general agreement with both the measured tensions and the tensions from the analytical model.

Cable tensions were computed as the product of the cable cross-sectional area and maximum principle stress predicted in the FEA at the center node of a given cable. A moving average cable tension is shown in Figure 4.8 (and throughout the parametric analysis) and is computed as the average of predicted tensions for the previous, current, and subsequent time steps. In general, cable tensions predicted for both cables in a given cable set (e.g., Cable 1a and Cable 1b in Figure 4.8a) exhibited similar temporal trends and had comparable magnitude. Cable tensions predicted at the end of the model simulations range from 1 kN for Cable Set 1 at the base of the barrier to approximately 400 kN for Cable 2b. The majority of the predicted tensions in Cable Set 2, 3, and 4 ranged between 50 and 70 kN. The largest cable tension in Cable 2b was located in the vicinity of Ring B (Fig. 4.1), whereby the pronounced downslope movement coincided with the large predicted tension in the cable.

The residual cable tension observed in measurements from the field-scale experiment in Ferrero et al. (2015) (e.g., 49 kN to 115 kN in Fig. 4.3) were subtracted from subsequent tension measurements to create a starting tension of 0 kN. The same approach was used for cable tensions predicted with the analytical model. Zeroing the cable tension yielded what is referred to as induced cable tension, which was more comparable between the FEA and field

measurements. Residual cable tension adjustments were not needed for predictions from the analytical model.

The time of impact for the field-scale experiment was considered equal to 0 since deformation and tension measurements increased immediately with increasing time (e.g., Fig. 4.3). Measured tensions in the cables and predicted tensions via the analytical model (Ferrero et al. 2015) were shifted by an equivalent elapsed time prior to loading in the FEA such that temporal trends of tensions could be compared directly.

Although variability exists in the predicted and measured cable tensions (cable 4c), overall the FEA was capable of accurately predicting cable tensions for the field-scale debris flow experiment (Figs. 4.8a, 4.8b, and 4.8d). Thus, from a practical perspective, the ability to accurately predict the maximum cable tension is useful for sizing appropriate structural components when designing flexible ring-net barriers.

4.1.3 Downslope Angle Analysis

An analysis was completed in FEA to assess the influence of downslope angle on horizontal deformation and cable tension. The downslope angle was simulated as a continuous 40° slope in model simulations discussed previously. An additional FEA was conducted with the downslope angle made to be horizontal to more directly represent the downslope conditions of the field-scale experiment (Figure 3.1). The FEA with horizontal downslope angle was conducted with a debris flow velocity equal to 2.51 m/s.

Final barrier deformations along the centerline of the barrier predicted with the FEA for a 40° slope, flat (i.e., horizontal) slope, and the final deformation from Ferrero et al (2015) are shown in Figure 4.9. The general shape of the final deformed barrier was similar for both slope considerations, and the 40° slope led to deformations that were approximately 0.2 m greater than deformations predicted with the flat slope. The model with the flat downstream slope more accurately matched with table the deformations found in the field test when compared with the

40° slope. This shows that the flat slope is a more applicable configuration to the field test and that downslope geometry impacts the final deformation result.

Temporal relationships of tension in Cable Set 1 through 4 predicted via the FEA considering a 40° slope and flat slope, compared to the measured tensions are shown in Figure 4.10. The magnitude of predicted cable tensions was comparable for both slope considerations for Cable Sets 2, 3, and 4. However, tensions in Cable Set 1a for the 40° slope were approximately an order of magnitude greater than tensions for 1b of the same simulation. Larger tensions for Cable Set 1 were attributed to blocks simulating the debris flow directly impacting the cable, whereas occasionally debris flow blocks had a tendency to slide over cables and yield lower cable tensions, as shown by lower tensions in cable 1b. Tensions in the flat slope configuration were in agreement with the 40° slope scenario as the flat slope tensions were approximately average of the two.

The downslope angle analysis indicated that comparable predictions of deformation and cable tension were obtained for flat and 40° slopes behind the ring-net barrier. The 40° slope was numerically simpler as a single plane could be created with the barrier and flow simulated on the slope. In contrast, the flat slope required a change in boundary geometry and also impacted the modular block flow used to simulate the debris flow. Although considering experiment geometry in the FEA model yielded more accurate deformation results (Fig. 4.9), using a simplified geometry resulted in a reasonable prediction of barrier deformation. This opportunity to simplify model geometry led to reduced computation time and was less prone to computational error. Thus, the 40°-slope configuration was used in the parametric study.

4.1.4 General Discussion

General trends are seen through all analyzed models during barrier loading. Figure 4.3 shows temporal distributions of ring deformation for Rings A – E (Fig. 4.11A) and cable tensions for cable 2a – 4a (Fig. 4.11b) for the 2.51 m/s simulation. Each surge is called out on the figure

as well as time of impact for the surge. It is noted that there is an approximate delay of 0.5 s between the surge and the impact. Surges are released every 1.1 s (i.e 1.1 s for Surge 1, 2.2 s for Surge 2, 3.3 s for Surge 3, and 4.4 s for Surge 4).

There is minimal deformation to the rings during the first surge. Surge 2 and Surge 3 causes the majority of the deformation, and Surge 4 causes minimal additional deformation (Fig. 4.11a). The lack of any deformation during Surge 1 shows that the initial surge did not activate the braking elements. Surge 2 and 3 occurred as the brakes were elongating, and Surge 4 did not cause any additional deformation. Deformation of the rings occur around the same time period (from 2.4 – 3.4 s) meaning that the net deforms as a single unit.

Figure 4.11b shows the cable tensions over time for the same model simulation. There is some increase in tensions throughout the loading process but there is a prominent increase in tension when the surge of approximately the same height impacts the barrier. Though the cables help absorb the load of surrounding impacts, the greatest tension increase is seen when surge hits a similar elevation of the cable. This is most notable from the continual increase in stress of the lower cables even during the later surges.

4.2 Parametric Study

A parametric study was performed to assess barrier response to different geotechnical and structural parameters. Flow velocity, flow density, and surge height were geotechnical variables, and the number of brake elements per cable and cross-sectional area of the rings were structural variables selected for analysis. All simulations were conducted with the 40° downslope configuration (Figure 3.1 and Figure 2.1). Parameter values used in the study were chosen to represent anticipated ranges encountered in field conditions.

4.2.1 Barrier Performance Metrics

Metrics used to assess performance of a flexible ring-net barrier include maximum retention capacity of the barrier (Geobrugg 2016), maximum impact force on the barrier (Leonardi et al. 2014; Calvetti et al. 2015), and deformation and stress in the horizontal reinforcement cables (e.g. Ashwood and Hungr 2016; Ferrero et al. 2015; Wendeler et al. 2006; Wendeler et al. 2007; Wendeler et al. 2008). Stress in the cables has been considered a limiting factor when evaluating performance of a flexible ring-net barrier.

In this parametric study, performance of a simulated ring-net barrier was evaluated with consideration to barrier deformation, maximum equivalent plastic strain (PEEQ) of the rings, and tensile forces in the horizontal cables. Overall barrier deformation was chosen to assess changes in geometrical configuration of the barrier during debris-flow loading that can influence retention capacity. Similar to the benchmark example, barrier deformation was quantified via deformation of Rings A through E since the ring-net barrier maintained a smooth deformed shape following debris flow loading.

Individual rings of ring-net barrier are key structural elements that interact to retain debris. Although the ring-net cables are the main supporting elements with regards to force, the debris flow mass is retained by the ring-net and failure of individual rings would release debris and propagate a global failure of the barrier system. An advantage of the ring-net barrier system is the ability to restore retention capacity and reuse the barrier following removal of debris. Reuse of the barrier is dependent on longevity and of the structural components, which the rings are a critical component. Equivalent plastic strain of five select rings (A through E; Fig. 4.1) was used to determine if stress-strain behavior in these rings was approaching a state of failure. Equivalent plastic strain is a scalar way to describe the strain occurring when the material undergoes plastic deformation. The PEEQ obtained for each ring was plotted against stress-strain data from a manufactured ring described in Escallon and Wendeler (2013) to better understand of how each geotechnical and structural variable impacted individual rings.

The horizontal reinforcement cables represent the primary structural elements of the barrier (Ferrero et al. 2015) and are used as a key performance metric in barrier studies (e.g. Wendeler et al. 2006, Wendeler et al. 2007; Wendeler et al. 2008). An assessment of tension developed in the two cables of each two-cable set (Figure 4.8) indicated that tensions were comparable (e.g., Cable 3a and Cable 3b in Figure 4.8). To reduce the amount of model simulation results analyzed, only the "b" cable of each cable set was evaluated in the parametric study. Additionally, Cable Set 1 was not included in the parametric study since cables in Cable Set 1 often became pinched between blocks of the first debris flow surge and the ground surface. Furthermore, the top cable was not included as this cable supported the ring-net barrier and temporal trends in tension were not consistent with other cables. Thus, tensions in Cable 2b, Cable 3b, and Cable 4b were evaluated in the parametric analysis.

Tensile forces developed in horizontal cables of a ring-net barrier must be dissipated into ground anchors, which are also a key component of a barrier system design (Ashwood and Hungr 2016; Leonardi et al. 2014; Volkwein et al. 2014; Calvetti et al. 2015). Ground anchors are designed for site specific conditions to determine anchor type, grout material, grout length, soil adhesion, and number of anchors, among other factors. The purpose of this parametric study was to assess response of a barrier system and not develop a specific design. A ground anchorage system was assumed to exist that was capable of retaining the maximum tension developed in the cables. A generalized analysis of a tie-back anchor in sand was performed to validate this assumption (Das 2013). Accounting for soil parameters in the benchmark study (Ferrero et al. 2015), a grouted anchor, 0.3-m diameter by 2-m long, with an adhesion of 70 kPa (Rajapakse 2015) can dissipate an ultimate cable tensile force of 252 kN. Thus, a reasonably sized ground anchor is capable of dissipating maximum cable tensions that would develop in the flexible ring-net barrier evaluated in this study.

4.2.2 Parametric Study Results

The geotechnical and structural parameters chosen for the study are described in Table 4.1 and summaries of the modeling results are tabulated in Table 4.2. The geotechnical parameters – debris flow velocity, debris flow density, and surge height – were chosen to capture characteristics of a debris flow that are anticipated to vary between unique flow events. The structural parameters – number of ring windings and number of cable brakes – were chosen to investigate how aspects of certain design elements impact barrier performance.

4.2.2.1 Debris Flow Velocity

Ring Deflection. Final horizontal deformation of Rings A through E for debris flow velocities of 0.5, 2.51, 9.0, and 12.0 m/s are shown in Figure 4.12. The final horizontal deformation of the barrier was similar for all four debris flow velocities, and maximum deformation ranged between 1.6 and 1.8 m. The maximum deformation always was observed near the middle of the barrier and the final barrier heights were approximately 3 m for all considered debris flow velocities.

Cable Tension. Temporal trends of cable tension in Cables 2a, 3a, and 4a are shown in Figure 4.13 for the four debris flow velocities evaluated. An increase in velocities corresponded to larger tension generated on initial impact; however, final cable tensions in a given cable (e.g., Cable 2a) were similar in magnitude for all debris flow velocities. Final cable tensions for all cables reached but did not exceed 60 kN, with the exception of Cable 2a. Tensions in cable 2a increased to approximately 100 kN. Regardless of debris flow velocity, braking elements were activated but not fully elongated, which implies that braking elements are critical to a barrier system regardless of the anticipated debris flow velocity.

PEEQ. Maximum equivalent plastic strains for Rings A through E are shown in Figure 4.14 for the four debris flow velocities. A maximum allowable strain level for the steel rings is plotted in Figure 4.14. Maximum allowable strain was taken from a stress-strain curve of the

rings was provided in Escallon and Wendeler 2013. The PEEQs were all below the maximum allowable strain, with the exception of Ring A (lowest ring in the barrier) for the 12 m/s debris flow. This scenario can be considered representative of a worst-case where a high velocity flow impacts the barrier. Furthermore, the magnitude may be an artifact of how the debris flow was simulated, whereby the first surge was a single block that impacted the lower part of the barrier (i.e., Ring A) with all available kinetic energy.

4.2.2.2 Density

Ring Deflection. Final horizontal deformation of Rings A through E for debris flow densities of 1900, 2100, 2260, and 2360 kg/m^3 are shown in Figure 4.15. An increase in debris flow density yielded an increase in horizontal deformation (1.5 m to 1.9 m) of the barrier and decrease in final height (≈ 2.8 to 2.6 m) of the barrier. The largest horizontal deformation corresponded to the highest debris flow density (2350 kg/m^3). However, the final deformed shape of the barrier as similar for all densities, with maximum deformation occurring at mid-height of the barrier.

Cable Stress*.* Temporal trends of cable tension in Cables 2a, 3a, and 4a are shown in Figure 4.16 for the four debris flow densities evaluated. In general, cable tension was not affected by debris flow density. Tensions predicted in Cable 3a and 4a were essentially identical and independent of debris flow density. However, there was approximately a one order of magnitude range in cable tension for Cable 2a, whereby the smallest tension (28 kN) corresponded to a density of 1900 kg/m^3 and the highest cable tension (122 kN) corresponded to a density of 2350 kg/m^3. Cable stress remains under the ultimate tensile stress of the steel (252 kN as discussed in Chapter 3) in all densities and all cables with the exception of Cable 2a during the 2100 kg/m^3 test. All residual stress, with the exception of Cable 2a for 2350 kg/m^3, after the debris flow is restrained are an order of magnitude lower than the maximum allowable tensile stress.

PEEQ. Maximum equivalent plastic strains for Rings A through E are shown in Figure 4.17 for the four debris flow densities. There is minimal trend between PEEQ of the rings and the density of the debris flow. With exception to a density of 1900 kg/m^3 strains remain at or below the maximum allowable strain for the ring.

4.2.2.3 Surge Height

Ring Deflection. Final horizontal deformation of Rings A through E for debris flow surge heights of 0.7 1.4, and 2.5 m are shown in Figure 4.18. The maximum horizontal deformation (≈ 1.75 m) of the barrier was not affected by height of an individual debris flow surge (Figure 4.18). However, the height at which the maximum horizontal deformation occurred as well as final height of the barrier decreased with decreasing surge height. This observation was attributed to thinner surge heights concentrating the initial impact and subsequent static force lower in the total height of the ring-net barrier. Regardless of the different surge heights considered, the total debris flow mass remained the same, which yielded similar final barrier deformation.

Cable Stress. Temporal trends of cable tension in Cables 2a, 3a, and 4a are shown in Figure 4.19 for debris flow surge heights of 0.7, 1.4, and 2.5 m. The total model simulation time decreased with increasing surge height since less time was required with fewer surges mobilized toward the ring-net barrier. Although differences between model simulation were observed with regards to the time of impact, there were not considerable differences in the magnitude of cable tension in any of the three cables evaluated (Figure 4.19). The largest debris flow surge height of 2.5 m did yield the largest tension in Cable 3a, which is located at the mid-height of the barrier. This larger cable tension coincided with a single, large debris flow mass that impacted the barrier with the force more focused at the height of Cable Set 3.

PEEQ. Maximum equivalent plastic strains for Rings A through E are shown in Figure 4.20 for the three different debris flow surge heights. There was no correlation between surge

height strain in the rings, and with exception of the 1.4-m surge height model, the ring PEEQ was below the maximum allowable strain.

4.3.3 Structural Parametric Study Results

Model simulations of the ring-net barriers were conducted to assess the effects of two structural parameters: number of brakes per cable and number of ring windings. In these simulations, the geotechnical properties of the debris flow were held constant to isolate the structural parameters. All simulations were conducted with debris flow surge heights of 0.7 m, flow velocity = 2.51 m/s, and flow density = 2260 kg/m^3.

4.3.3.1 Number of Brakes per Cable

Ring Deflection. Final horizontal deformation of Rings A through E are shown in Figure 4.21 for ring-net barrier model simulations that considered 0, 2, and 4 braking elements per cable. An increase in the number of braking elements increased the total potential deformation of a given cable, and as expected, model simulations indicated that larger horizontal deformation corresponded higher number of braking elements. As the number of brake elements increased, deformation increased in the horizontal direction and the final height of the barrier reduced (Figure 4.21). The ring-net barrier simulated with zero braking elements shows less than 1-m of horizontal deformation, which represents a stiff response due to the lack of braking elements that allow elongation of the barrier as loading increased.

Cable Stress. Temporal trends of cable tension in Cables 2a, 3a, and 4a are shown in Figure 4.22 for ring-net barriers with 0, 2, and 4 braking elements per cable. The cable tensions in simulations with 2 and 4 brake elements increased to approximately 60 kN and remained constant, which was anticipated due to the activation force of the braking elements set at 60 kN. However, cable tensions in the barrier simulation with zero braking elements yielded cable tensions > 5000 kN, which were larger that the steel cable yield strength reported in Ferrero et

al. (2015). Higher cable tensions were anticipated in the simulation with zero braking elements, and the models show the efficacy of the braking elements in allowing elongation of the ring-net barrier to decrease the force transferred to the cables.

PEEQ. Maximum equivalent plastic strains for Rings A through E are shown in Figure 4.23 for the ring-net barriers with 0, 2, and 4 braking elements per cable. The PEEQ in individual rings increased with an increase in the number of braking elements. This relationships was attributed to the increased amount of deformation (Figure 4.21) that developed in ring-net barriers simulated with 2 and 4 braking elements per cable. Zero strain was predicted for the barrier with zero braking elements since deformation was inhibited and all loading from the debris flow was carried by the cables (Figure 4.22). However, the larger barrier deformations for 2 and 4 braking elements per caused strain to develop in the ring-to-ring contacts of the ring net, which yielded higher PEEQs. Overall, the PEEQ was less than the maximum allowable strain of the steel rings for all simulations with varying braking elements.

4.3.3.2 Number of Ring Windings

Ring Deflection. Final horizontal deformation of Rings A through E are shown in Figure 4.24 for ring-net barrier model simulations that considered varying strength rings. The strength of the ring was varied via the number of windings per ring (5, 7, 10, and 12), whereby a single winding corresponds to a single, thin steel cable that is looped to form a ring. Thus, the simulation with 5 windings per ring includes rings formed via looping the thin steel cable 5-times to form a single ring. The final horizontal deformation of the ring-net barrier was the largest for the lowest number of ring windings due to a lower overall strength ring-net barrier. However, final horizontal deformation for the four different ring windings only varied within a small range (i.e., 1.5 m and 1.75 m) since the cables are the main structural element in the ring-net barrier and absorb the majority of the load. The rings primarily are designed to retain the debris flow.

Cable Stress. Temporal trends of cable tension in Cables 2a, 3a, and 4a are shown in Figure 4.25 for ring windings of 5, 7, 10, and 12. There were no systematic trends observed between the number of ring windings and cable tension in any of the cables evaluated. Considering that the ring-net is designed to restrain debris and not designed as a load bearing component of the net, the lack of any trend between ring windings and cable tension was anticipated.

PEEQ. Maximum equivalent plastic strains for Rings A through E are shown in Figure 4.26 for the ring windings of 5, 7, 10, and 12. In general, the PEEQ decreased with an increase in the number of windings since the rings with a higher number of windings had larger cross-sectional diameters. Rings with larger cross-sectional diameter will experience less stress for an equivalent force, which will yield lower strains for similar moduli used to represent the strength of the steel rings.

4.2.3 Discussion of Geotechnical Parameters

The geotechnical parameters, debris flow velocity, density, and surge height, were selected as variables in the parametric study to assess how different debris flow characteristics could impact a given flexible steel, ring-net barrier. In general, model simulation results suggest that there were no correlations between debris flow parameters and performance metrics of the ring-net barriers (i.e., barrier deformation, cable tension, or equivalent plastic strain).

A compilation of all temporal trends of cable tension predicted in model simulations for the three debris flow variables (i.e., velocity, density, and surge height) is shown in Figure 4.27. All simulations with varying debris flow characteristics yielded final cable tensions ≈ 60 kN, which was the required activation force to mobilize the braking elements. These model simulations emphasize the importance of including braking elements in ring-net barrier design. The braking elements act to reduce the total load acting on a barrier via allowing elongation and larger barrier deformation.

A compilation of final horizontal deformation and height of the barrier for all model simulations completed for the three debris flow parameters is shown in Figure 4.28. Final profiles of the ring-net barriers had comparable shapes, with maximum horizontal deformation ranging between 1.5 m and 2.0 m and final barrier height ranging between 2.5 m and 3.2 m. Regardless of the debris flow velocity or height of individual surges, the final static load from the debris flow in these simulations was. However, an increase in debris flow density increased the mass acting on the barrier, which increased the final static load. Considering that the magnitude of horizontal deformation was observed to increase with increasing density (Figure 4.15), barrier deformation appears more related to the static load acting on the barrier after the debris flow has been retained versus the dynamic, impact force of the debris flow.

A compilation of equivalent plastic strain in Rings A through E for all model simulations completed with the three debris flow variables is shown in Figure 4.4. In general, the different geotechnical properties of the debris flow had minimal influence on the equivalent plastic strain. Increasing the debris flow velocity modestly increased PEEQ; however, this increase was not consistent among all rings or all flow velocities, and was considered non-representative of an actual correlation. Additionally, most of the predicted PEEQs remained below the maximum allowable strain of the rings, which implies that for practical purposes the rings of the ring-net barrier system were not at risk of failure. The select, elevated PEEQ predictions may also be attributed to numerical errors in the FEA, considering the complexity of the model that consisted of thousands of individual rings (i.e., large number of elements and nodes). Thus, regardless of elevated PEEQ may be predicted for select rings, the overall integrity of the ring-net barriers was maintained in all simulations.

The two performance metrics of barrier deformation and cable tension yielded similar observations for the simulated ring-net barriers. In simulations where the static load acting on a barrier increased, tension in the cables remained approximately constant throughout the analysis. Cable tensions initially increased to 60 kN, which was the required activation force of

the braking elements, and remained at approximately 60 kN until the end of the simulation. The braking elements are crucial to barrier performance as even in model simulations with the lowest impact forces (e.g., lowest initial velocity, lowest flow density, and smallest surge height), the braking elements were activated. Furthermore, braking elements did not reach maximum elongation, as the cable tensions did not exceed 60 kN. This latter observation indicates that the braking elements had additional elongation and loading capacity. The additional capacity translates to the ability to absorb and retain subsequent debris flow events prior to cleaning the debris and repositioning the ring-net barrier with new braking elements.

4.2.4 Discussion of Structural Parameters

The assessment of the number of braking elements on the cable tension and barrier deformation accentuated the importance of including braking elements in a flexible steel, ring-net barrier. The model simulation completed with zero braking elements yielded a peak cable tension > 5000 kN (Fig. 4.22), which was two orders of magnitude larger than the tensions induced with two or more braking elements per cable. The large increase in the cable tension in the model with zero braking elements illustrates how the brakes can dissipate the load from a debris flow. Based on steel properties in Ferrero et al. (2015), the ultimate tensile strength of the steel cables used in their design was 252 kN. Without braking elements included in the design, cable tensions would surpass the ultimate strength and likely fail under the model simulation conditions evaluated herein.

The zero braking element model can also be used to assess potential cable tensions in the event that braking elements are not replaced after a flow event. If a debris flow event had occurred and subsequently there was additional retention capacity within the barrier or if retention capacity was restored via excavation, there could be a scenario where subsequently loading would be analogous to the barrier loading simulation with zero braking elements. Subsequent loading could increase cable tension above the maximum allowable tension of the

cables and result in failure of the barrier system. Thus, the assessment of braking elements provides observation relationships that support the importance of maintaining functional braking elements in a flexible steel, ring-net barrier.

No relationship existed between the number of ring windings and the barrier deformation, or the cable stress (Fig. 4.24 and Fig. 4.25). This is because the purpose of the ring net is to restrain the debris and not to absorb the load from the debris flow. It was noted as the number of windings, and thus the cross-sectional area of the individual rings, increased the equivalent plastic strain in the rings decreased. Rings with a larger diameter will experience less stress given an equivalent force than rings with a smaller diameter, as stress is equivalent to force over area. Thus, more windings will undergo smaller strains given the same load. In the study of braking elements, the PEEQ increases with increased deformation (Fig. 4.23). In previous models the increase in deformation was not large enough to induce additional strain in the rings. However, the ring net became strained when deformations varied from 0.8 m to 2.2 m. Even in the four brake scenario, the strains did not exceed the maximum allowable strain, however, as the number of brakes continue to increase the anticipated strains in the rings will increase. Thus, if the designed deformations become large enough, rings could be at risk of strain failure.

Table 4.1 A summary of the parameters chosen for the parametric study.

Parameter		Values used	Parameter Description
Geotechnial Parameters	Flow Velocity (m/s)	0.5, 2.51, 9, 12	Initial velocity of the debris flow. Parameter is applied to the back boundary of the debris flow mass in the FEA model. The flow is released at the applied velocity.
	Flow Density (kg/m3)	1900, 2100, 2260, 2350	Density assigned to the debris flow mass in the FEA. This relates to the combined density (i.e. a composite of the fluid, solid, and air phases) of a debris flow.
	Surge Height (m)	0.7, 1.4, 2.8	The height of the debris flow at time of impact, represented by the height of the layer impacting the barrier in the FEA model. The total mass of the debris flow remained the same regardless of surge height such that as the surge height decreased, the number of flows increased (i.e. the 2.8 m surge height had only one surge, whereas the 0.7 m surge height had 4 surges.
Structural Parameters	Number of braking elements	0, 2, 4	Braking elements are located on the horizontal support cables. Number of braking elements refers to the total number of elements found on each cable (i.e. a cable having one braking element on each end of cable has two braking elements)
	Number of ring Windings	5, 7, 10, 12	Cross-sectional area of the rings can vary depend on the number of times the wire has been wound around to form the ring. The wire strand is 3 mm in diameter and the properties do not change but increasing the number of times the wire is wound to create the ring will increase the strength and cross-sectional area of the ring.

Table 4.2 Summary of the effect that each parameter has on barrier performance (i.e. barrier deformation, cable tension, and equivalent plastic strain).

Parameter		Values	Effect on Barrier Performance		
			Barrier Deformation	Cable Tension	Equivalent Plastic Strain (PEEQ)
Geotechnical Parameters	Flow Velocity (m/s)	0.5, 2.51, 9, 12	Initial velocity had little impact on the final deformation of the barrier. Maximum deformations varied from 1.6 m to 1.8 m.	Increasing velocity saw larger tensions upon initial impact however final cable tensions for all cables reached but did not exceed 60 kN.	There was no direct correlation between the debris flow velocity and the strain experienced in the rings.
	Flow Density (kg/m3)	1900, 2100, 2260, 2350	Increasing debris flow density results in an increase of barrier deformation.	Cable stress is not affected by debris flow density.	There is minimal trend between PEEQ of the rings and the density of the debris flow.
	Surge Height (m)	0.7, 1.4, 2.8	The maximum deflection of the barrier is not affected by the height of the individual surge, having a final deformation of approximately 1.75 m	There is no consistent trend with cable tensions and surge height.	There was no direct correlation between the number of surges in a debris flow and the strain experienced in the rings.
Structural Parameters	Number of braking elements	0, 2, 4	As the number of brake elements increased, deflection increased in the horizontal and vertical directions.	Cables stress for the tests with two and four brake elements increase to 60 kN and then remain constant. The barrier without any brake elements had cable stresses reach over 5000 kN	PEEQ in individual rings increased with the number of braking elements.
	Number of ring Windings	5, 7, 10, 12	The number of windings per ring had no effect on the deformation of the cable.	There is no correlation between the number of ring windings and the stresses experienced in the cables.	The plastic equivalent strain decreases with increasing number of windings.

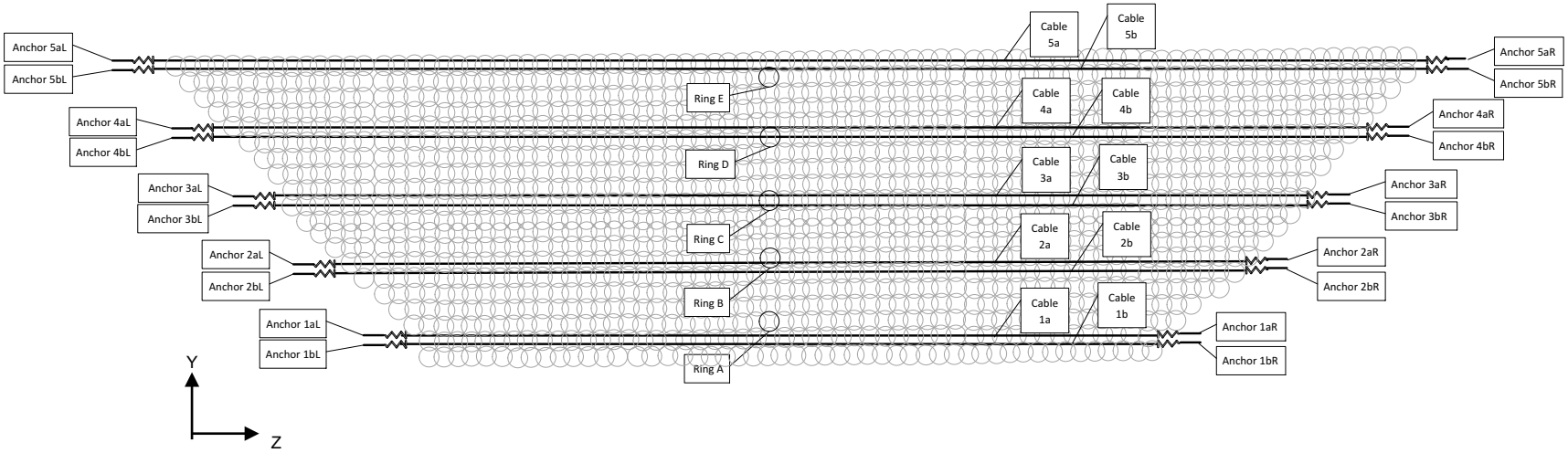

Figure 4.1 Labeled components of the barrier referenced in the benchmark and parametric study. Drawing is not to scale.

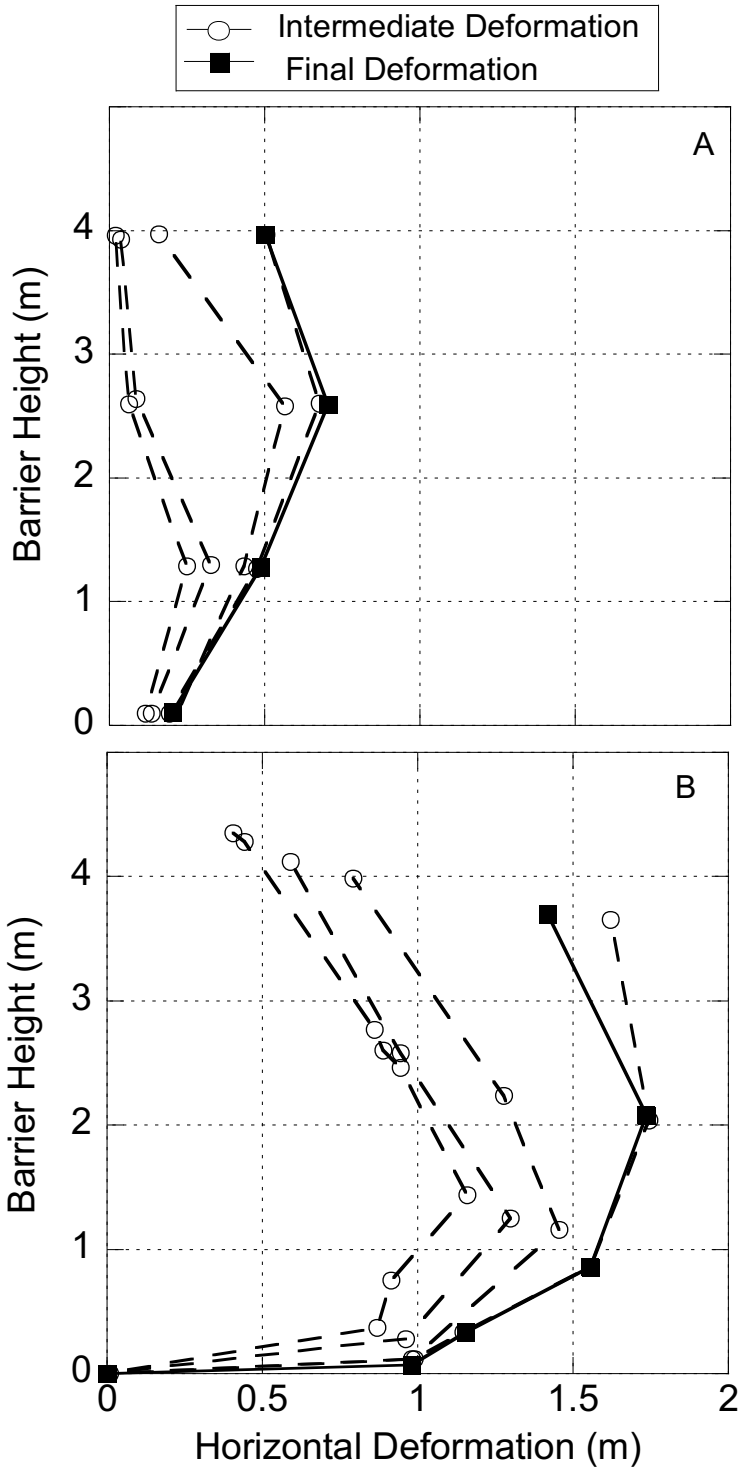

Figure 4.2 Plots of barrier deflection against vertical cable coordinate taken along the centerline of barrier for different elapsed times as (a) predicted in the analytical model and (b) measured in the field-scale experiment. from Ferrero et al 2015. Each line represents a different time step. Deformation is assumed to increase with an increase in time.

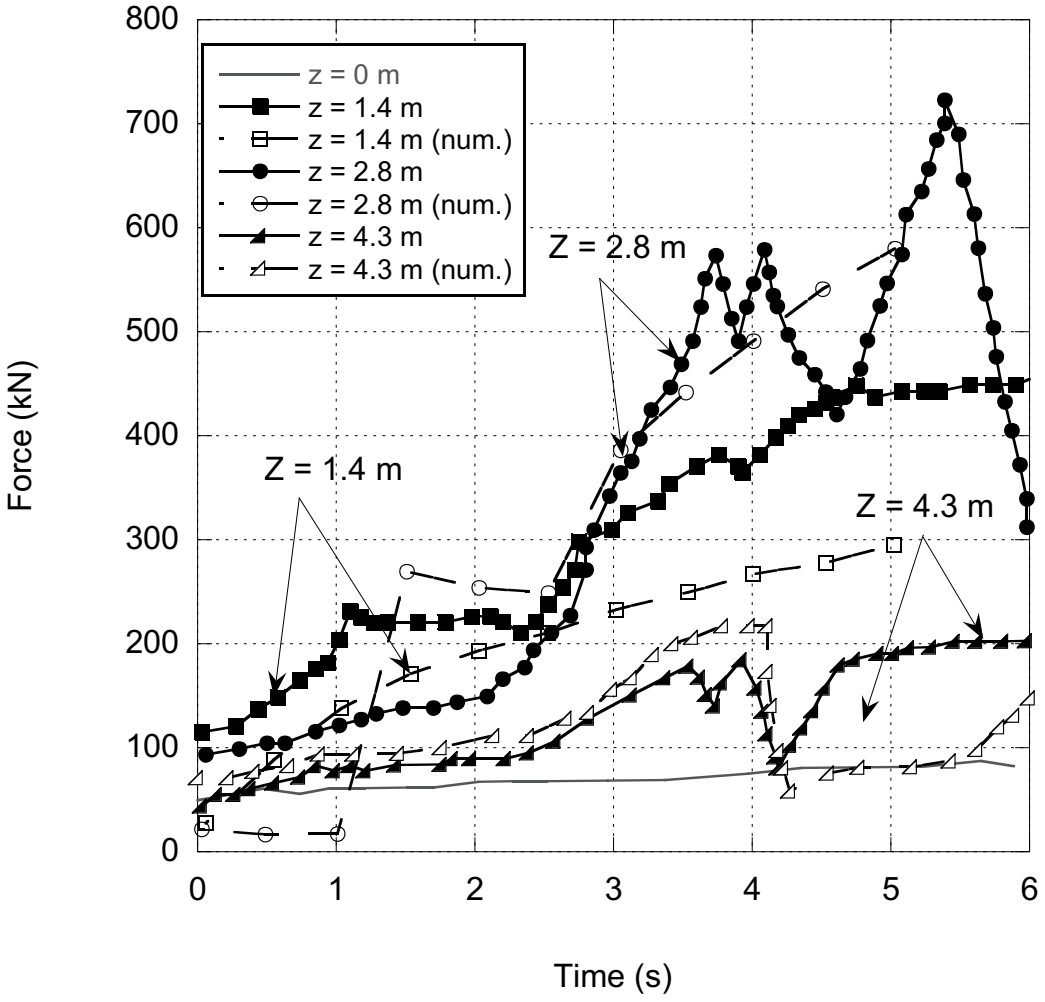

Figure 4.3 Tension forces developed in cables during the loading process in field test and calculated from analytical model taken from Ferrero et al 2015.

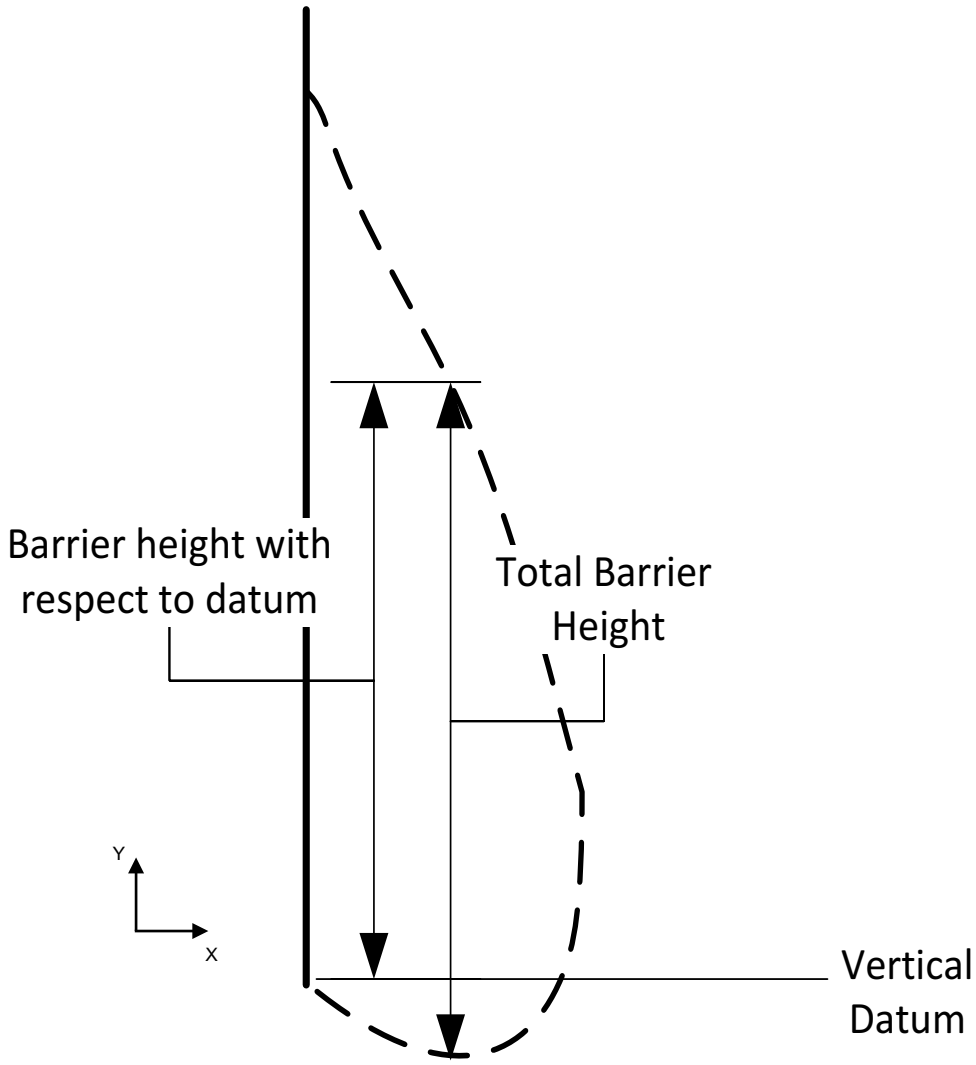

Figure 4.4 Adjustment from the barrier height with the respect to the datum vs the total barrier height. The deformation below the vertical datum was added to the heights provided by Abaqus to generate total barrier height.

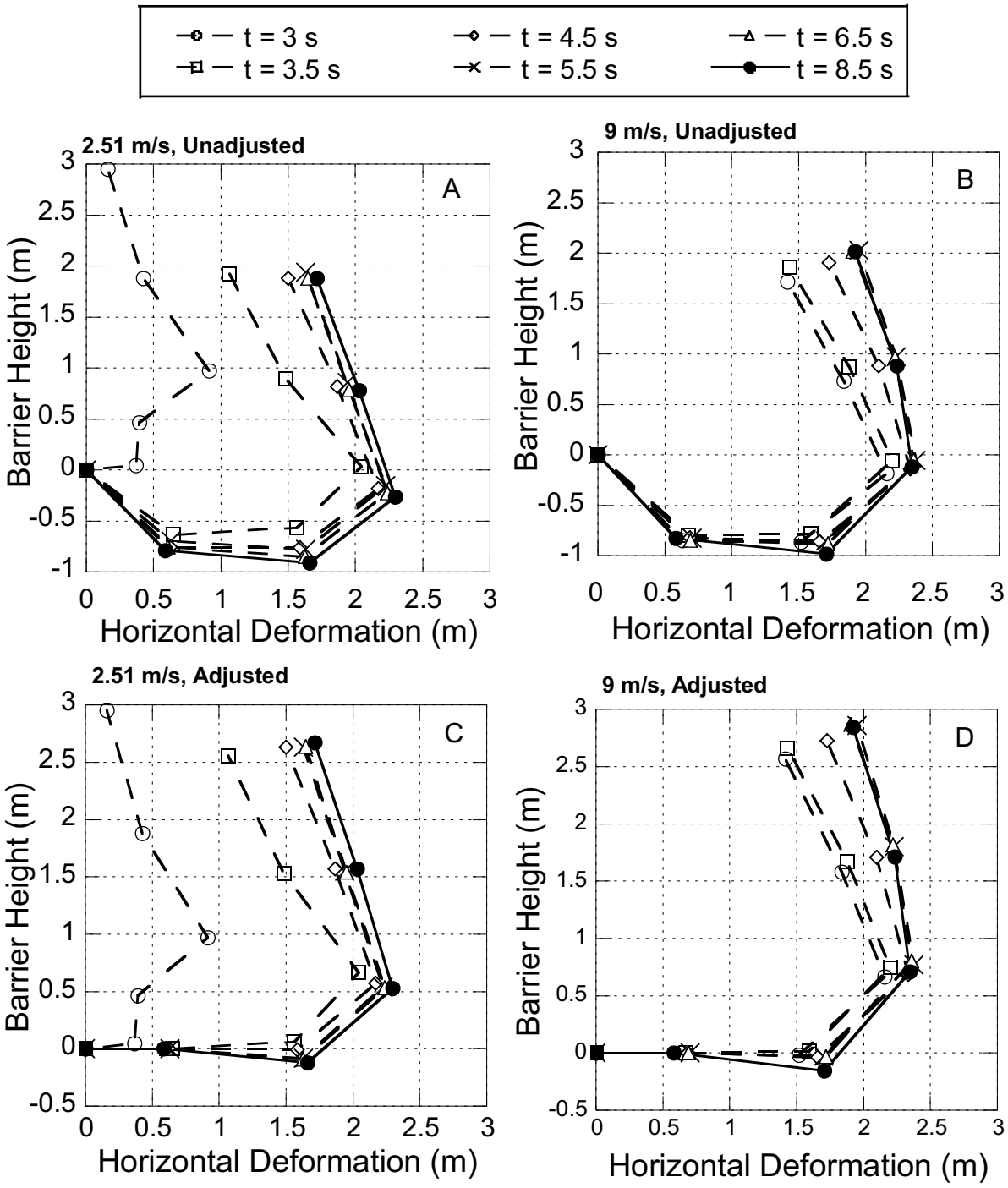

Figure 4.5 Predicted deformation of the ring-net barrier from the finite element analysis for the following considerations: (a) debris flow velocity of 2.51 m/s; (b) debris flow velocity of 9 m/s; (c) adjusted deformation for debris flow velocity of 2.51 m/s; and (d) adjusted deformation for debris flow velocity of 9 m/s.

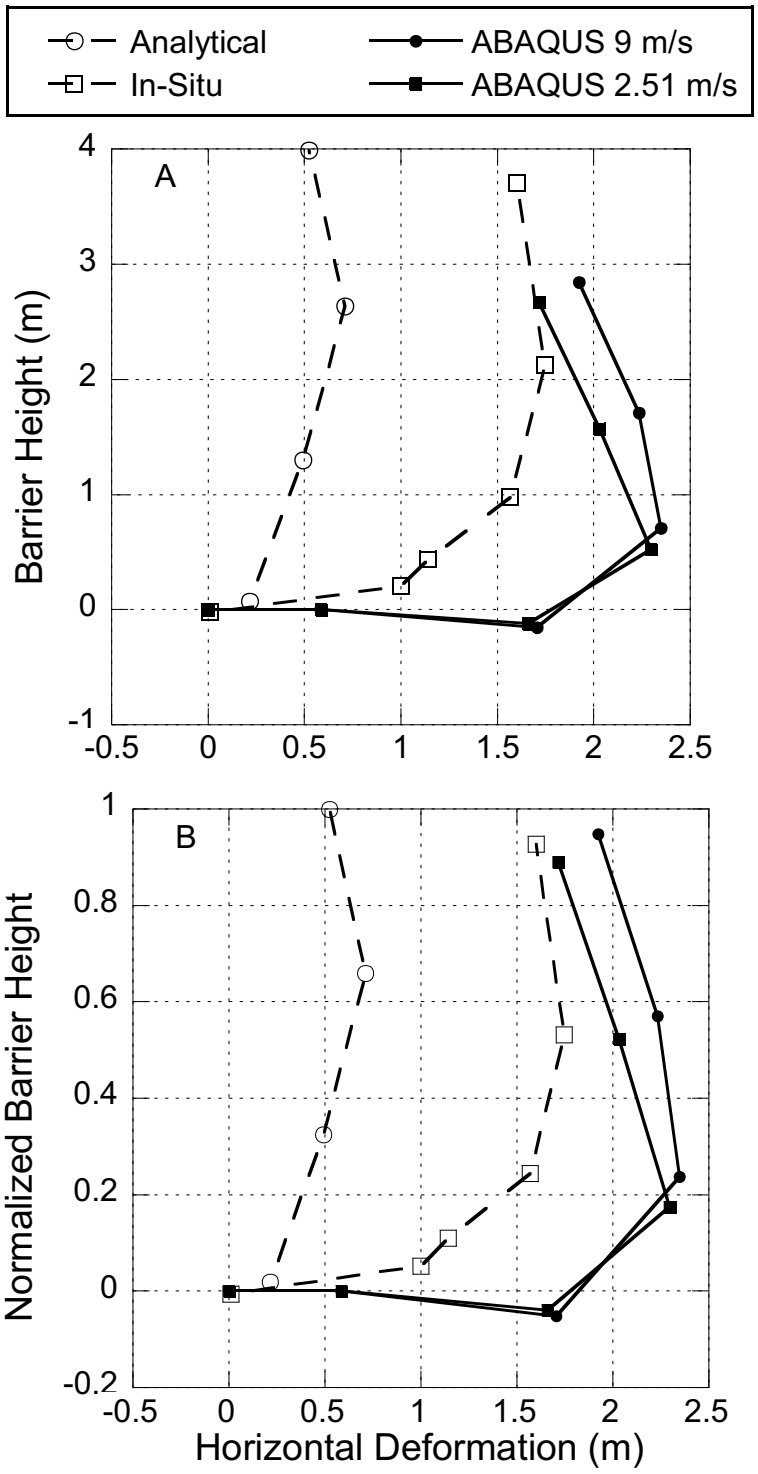

Figure 4.6 Final deformation of the ring-net barrier as measured in the field and predicted with the analytical model (Ferrero et al. 2015) and predicted with the finite element analysis for both 2.51 m/s and 9 m/s. The height of the barrier is normalized with respect to the initial height of barrier.

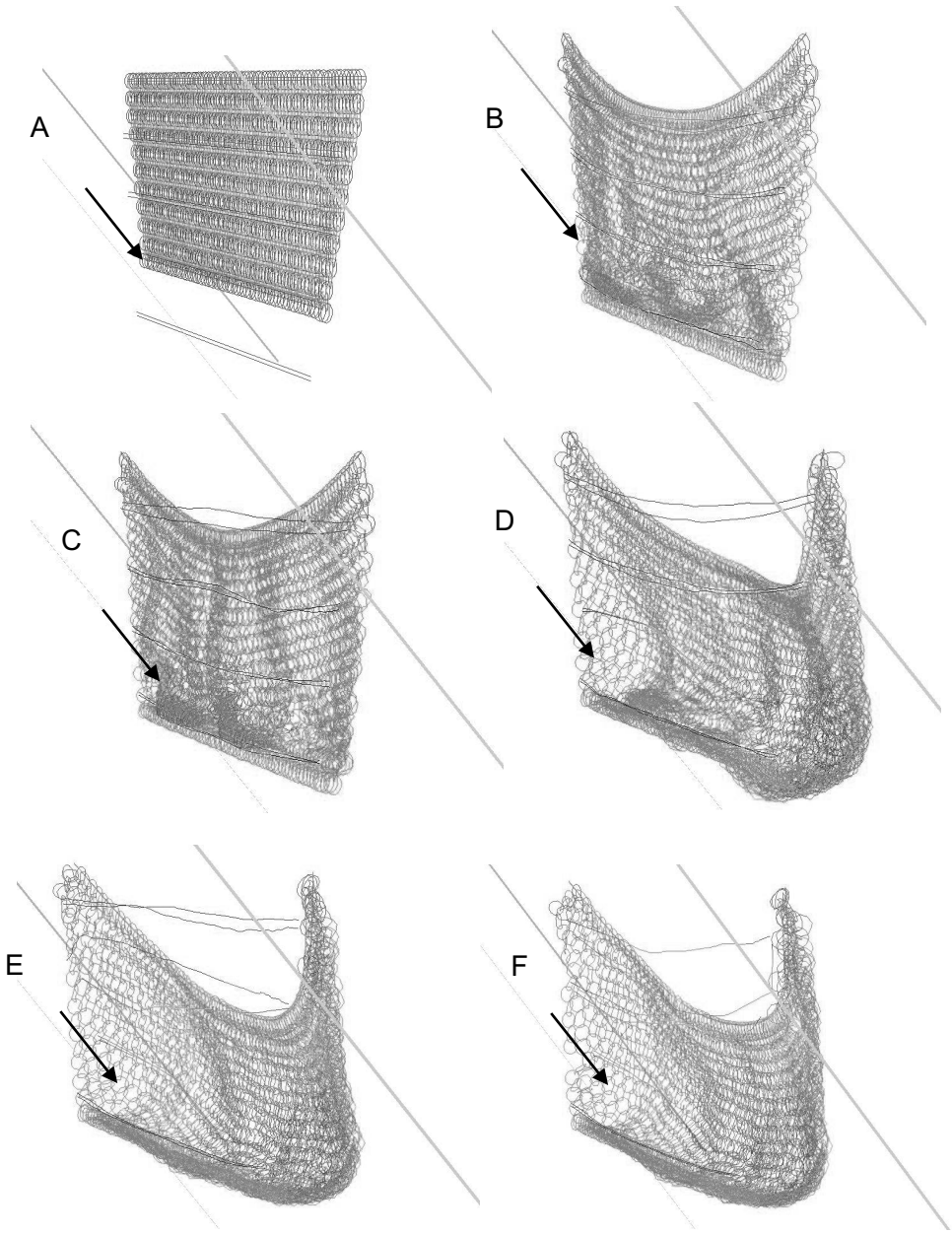

Figure 4.7 Deformation of the barrier throughout the model. Images are at (a) the beginning of the model showing initial model set-up, (b) at the end of the barrier settling period, (c) after the first debris flow surge (d) after the second debris flow surge (e) after the third debris flow surge and (f) at the end of the model, after the 4th debris flow surge. The arrow represents the direction of flow.

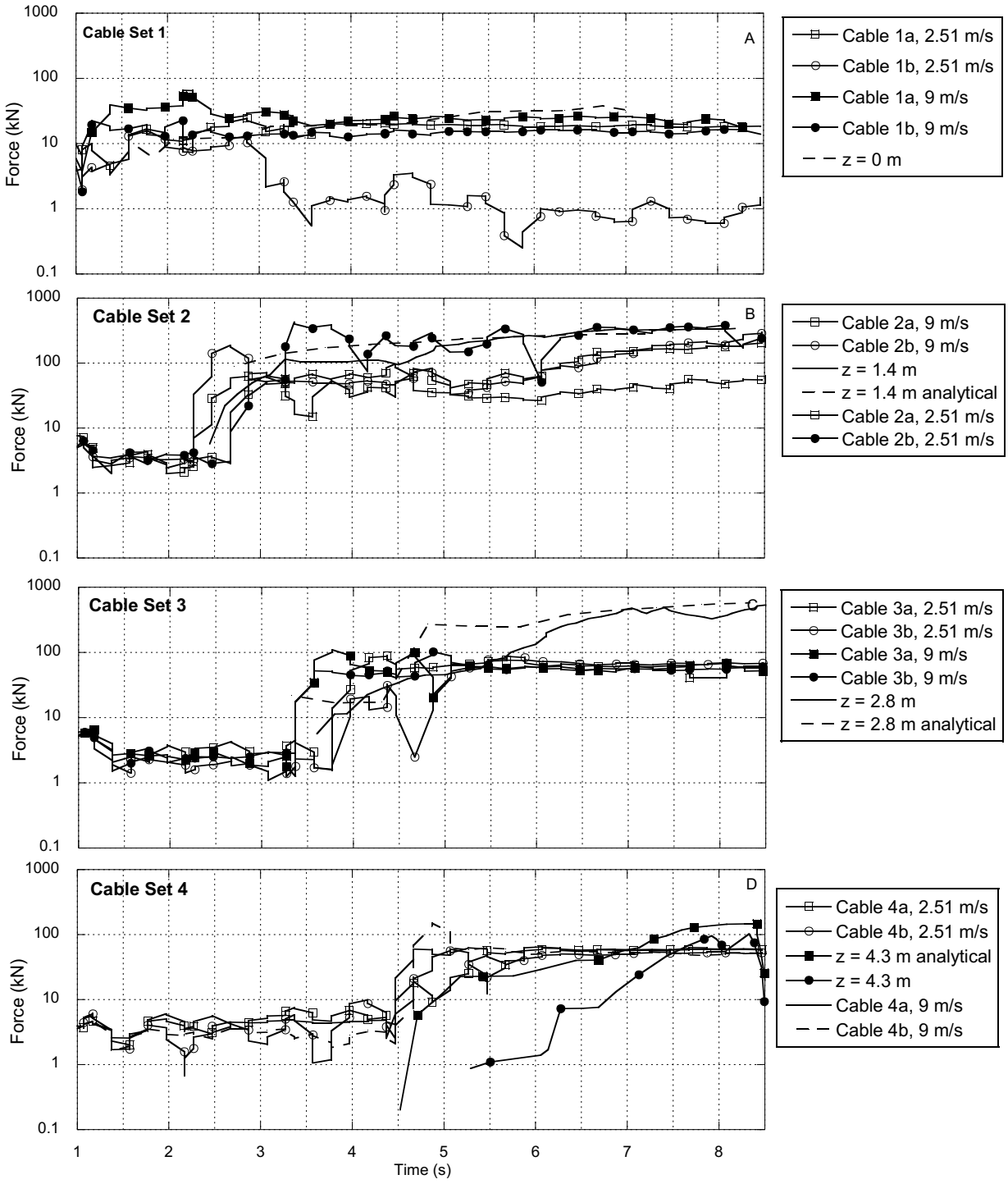

Figure 4.8 A comparison of cable tensions for the FEA model 2.51 m/s and 9 m/s simulation, the calculated tensions in the analytical model, and the measured tensions in the field model. Each cable Set is represented in a graph with (a) Cable Set 1; (b) Cable Set 2; (c) Cable Set 3; and (d) Cable Set 4. Cable tension is plotted through time elapsed during the respective test.

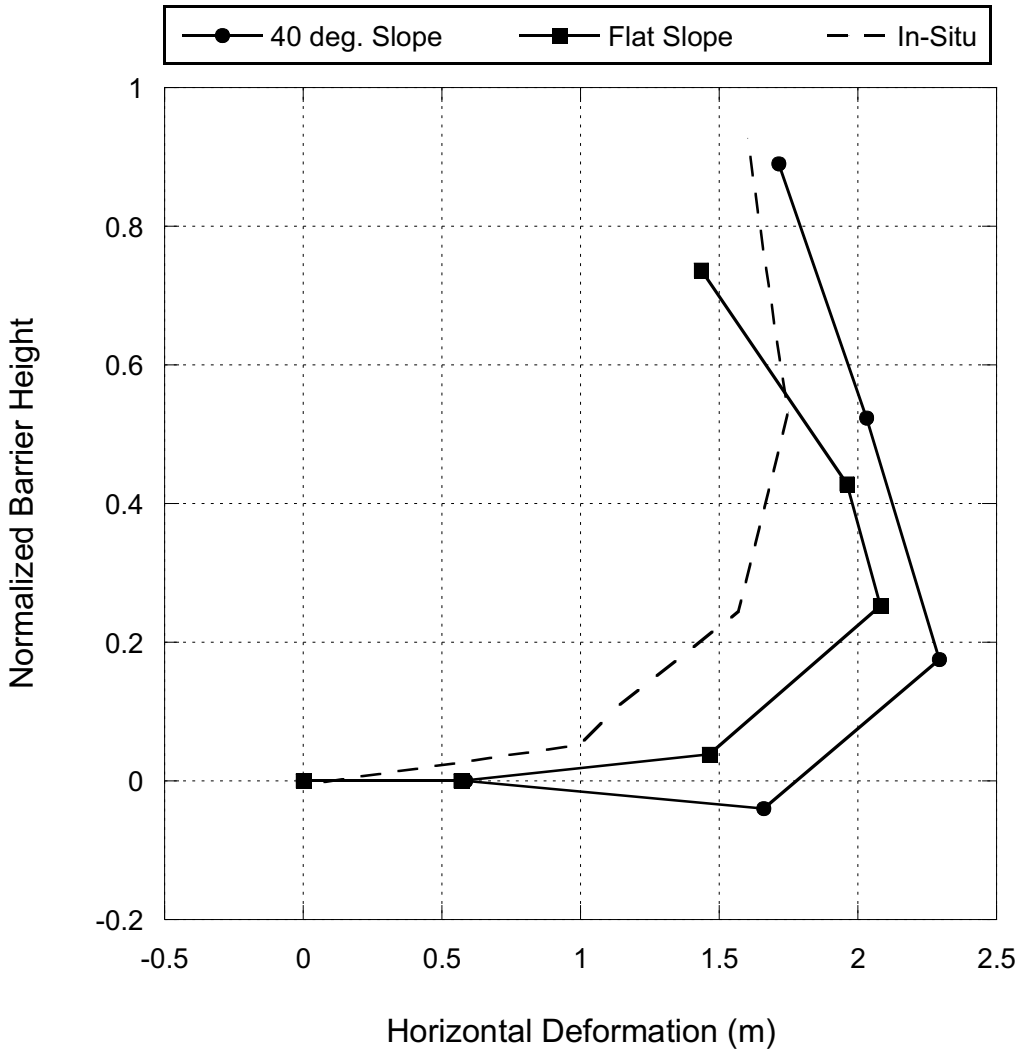

Figure 4.9 Comparison of the affect the downslope topography has on the final deformation. FEA model simulations for a barrier located on a flat slope and on the 40^{o} slope are plotted against the final deformation from Ferrero et al. 2015.

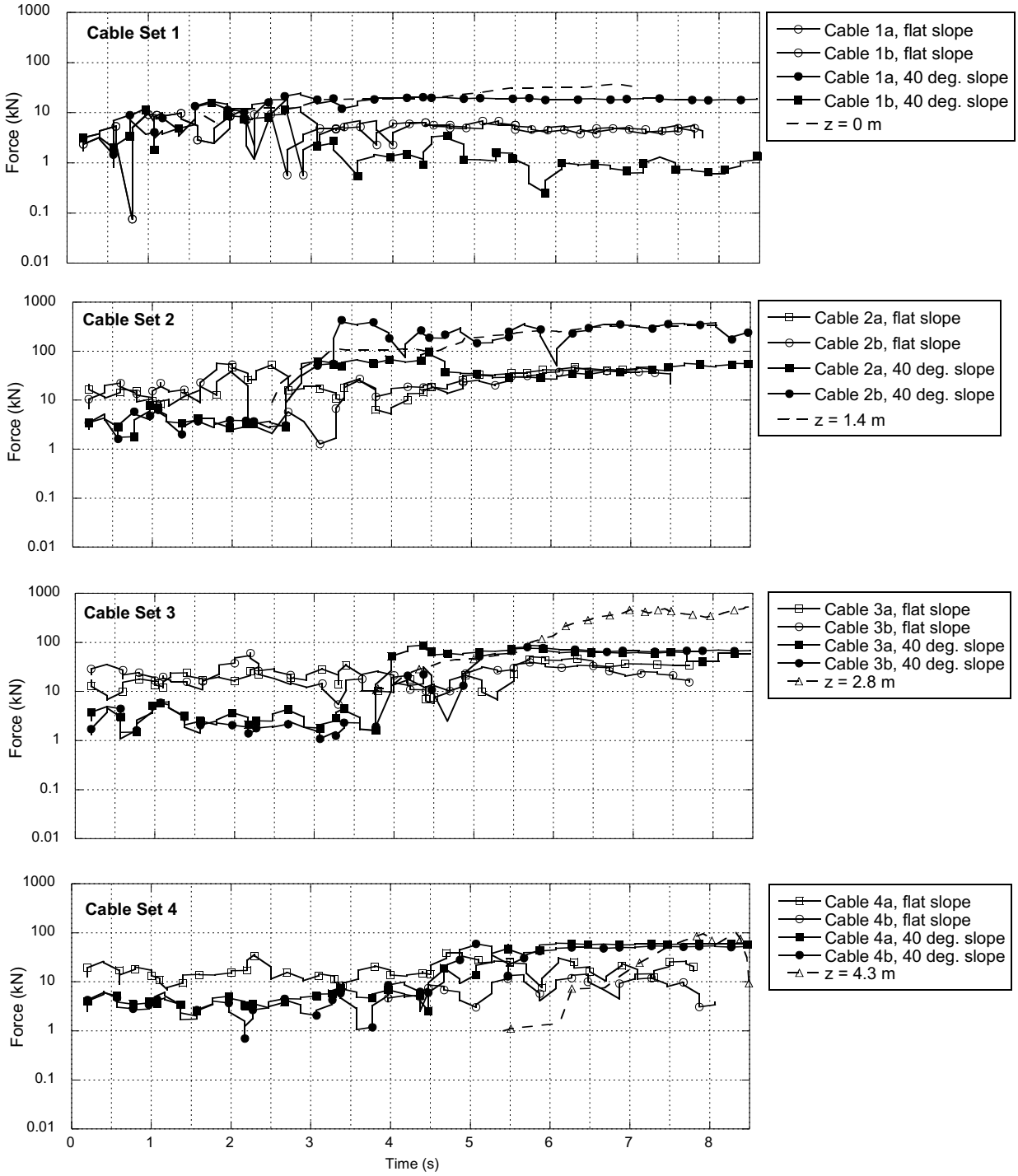

Figure 4.10 A comparison of cable tensions for the 2.51 m/s FEA models with the barrier located with the topography downstream of the barrier having a 40^{o} slope and with a flat topography downstream of the barrier. Each cable Set is represented in a graph with (a) Cable Set 1; (b) Cable Set 2; (c) Cable Set 3; and (d) Cable Set 4.

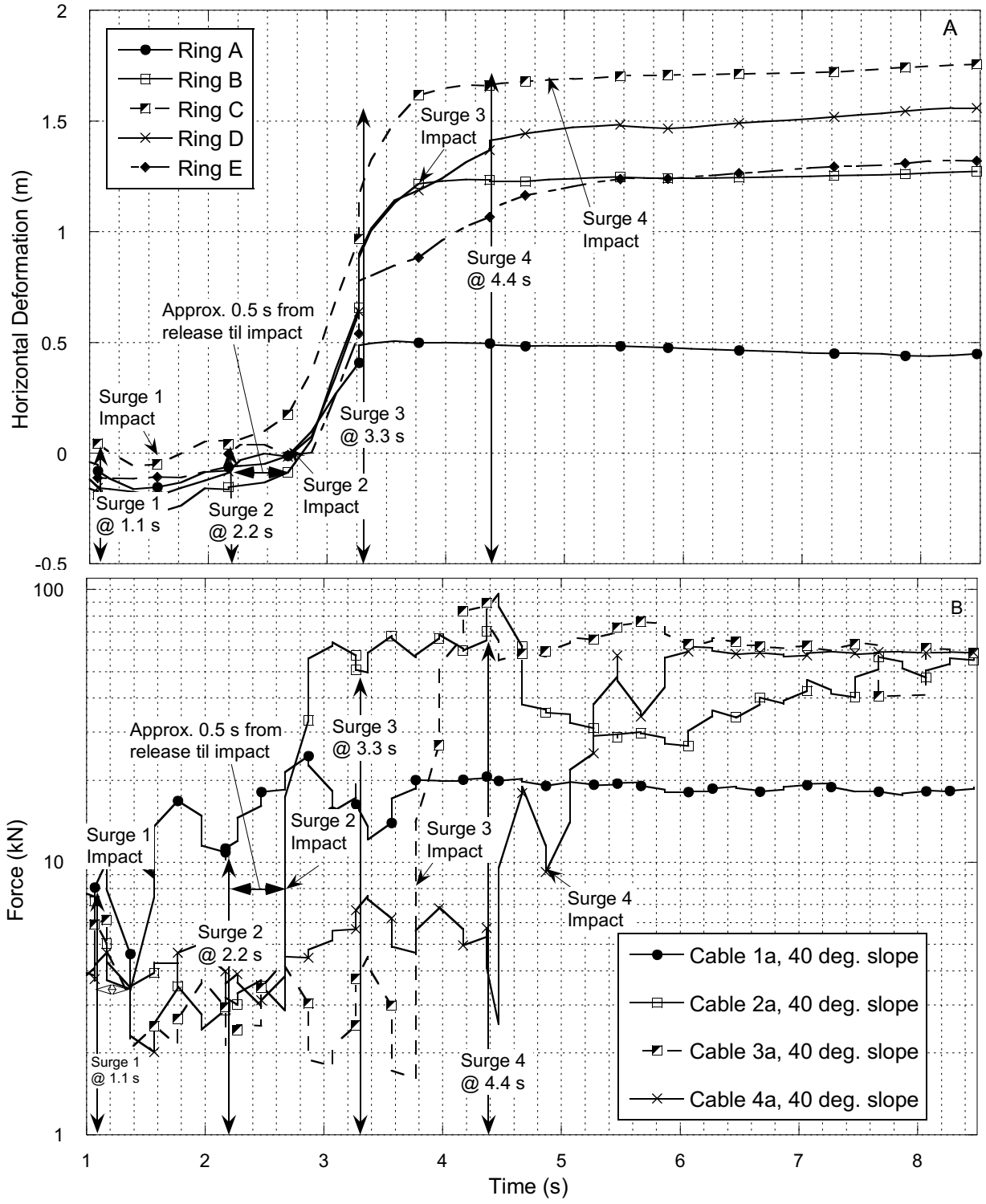

Figure 4.11 A comparison of (a) the horizontal deformation of the rings over time and (b) the cable tension over time. The time of each surge release and the time of impact is called out on each graph. It is noted that there is an approximate 0.5 s delay from surge release to surge impact. Matching symbols on the graphs represent roughly the same vertical coordinate.

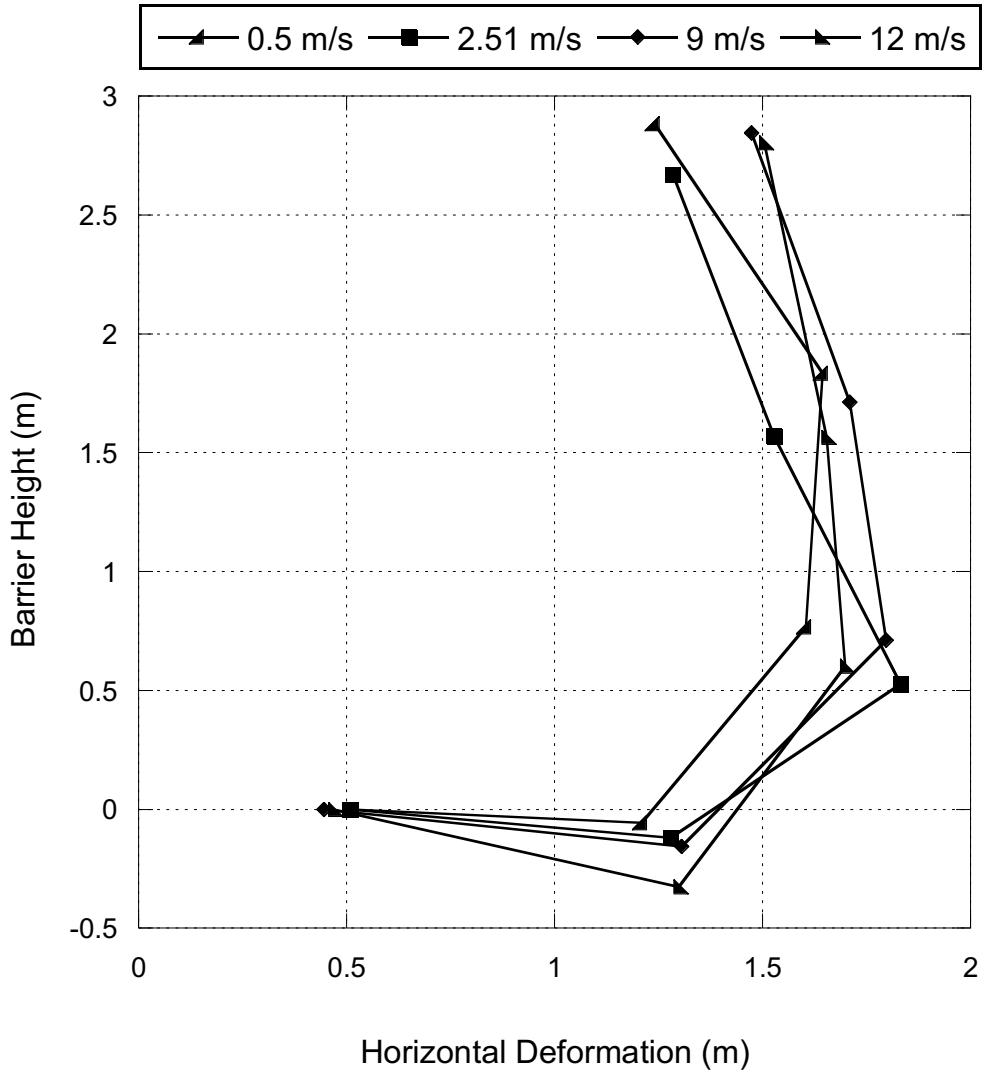

Figure 4.12 The final deformed shape of the barrier for each velocity simulation. Final deformation was taken along the centerline from Rings A through E.

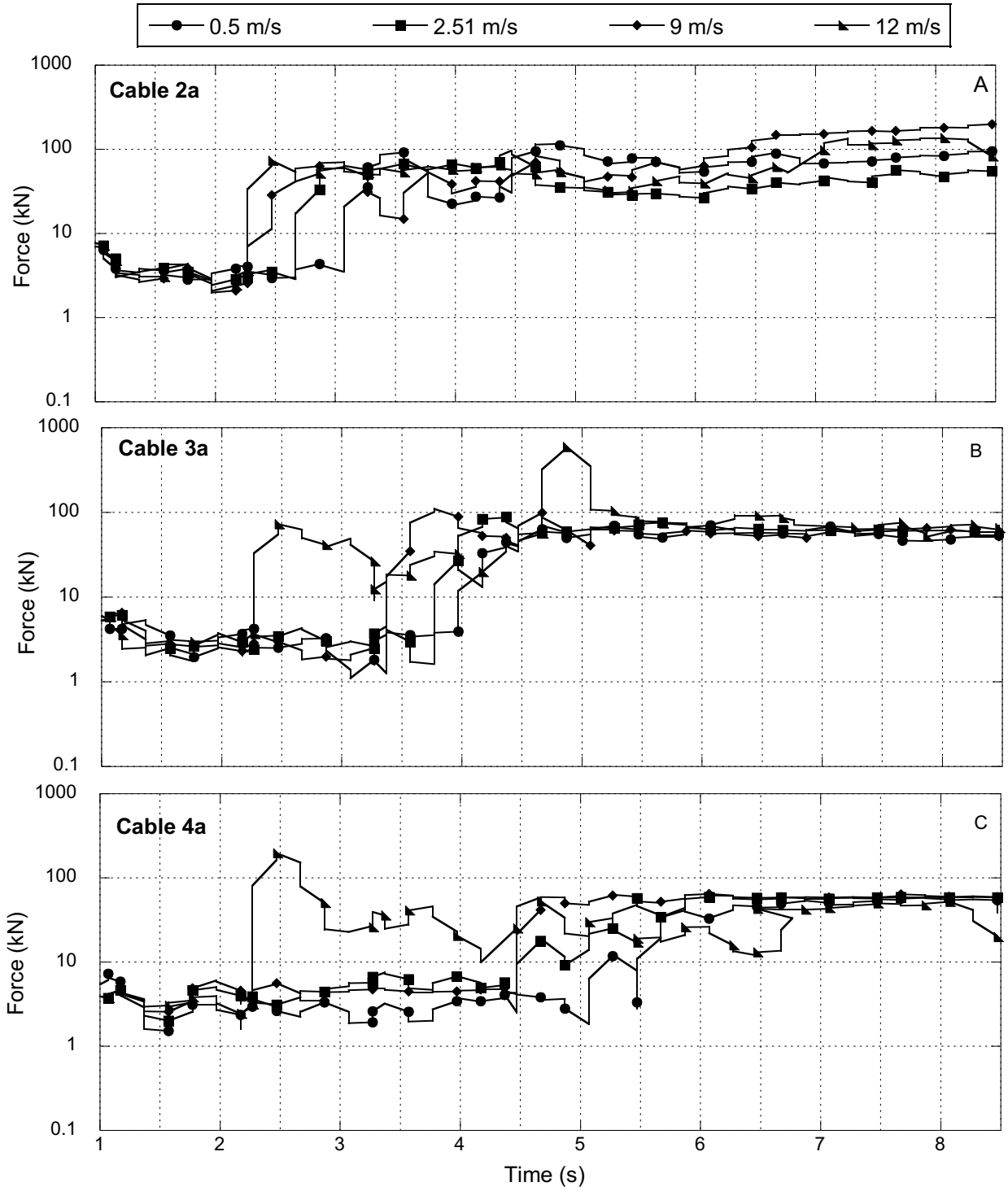

Figure 4.13 A comparison of cable tension over time in (a) Cable 2a: (b) Cable 3a; and (c) cable 4a for each of the velocity simulations. Tensions for each simulation (i.e. 0.5 m/s, 2.51 m/s, 9 m/s, and 12 m/s) for each respective cable are plotted together to compare the affect each velocity has on the induced tension.

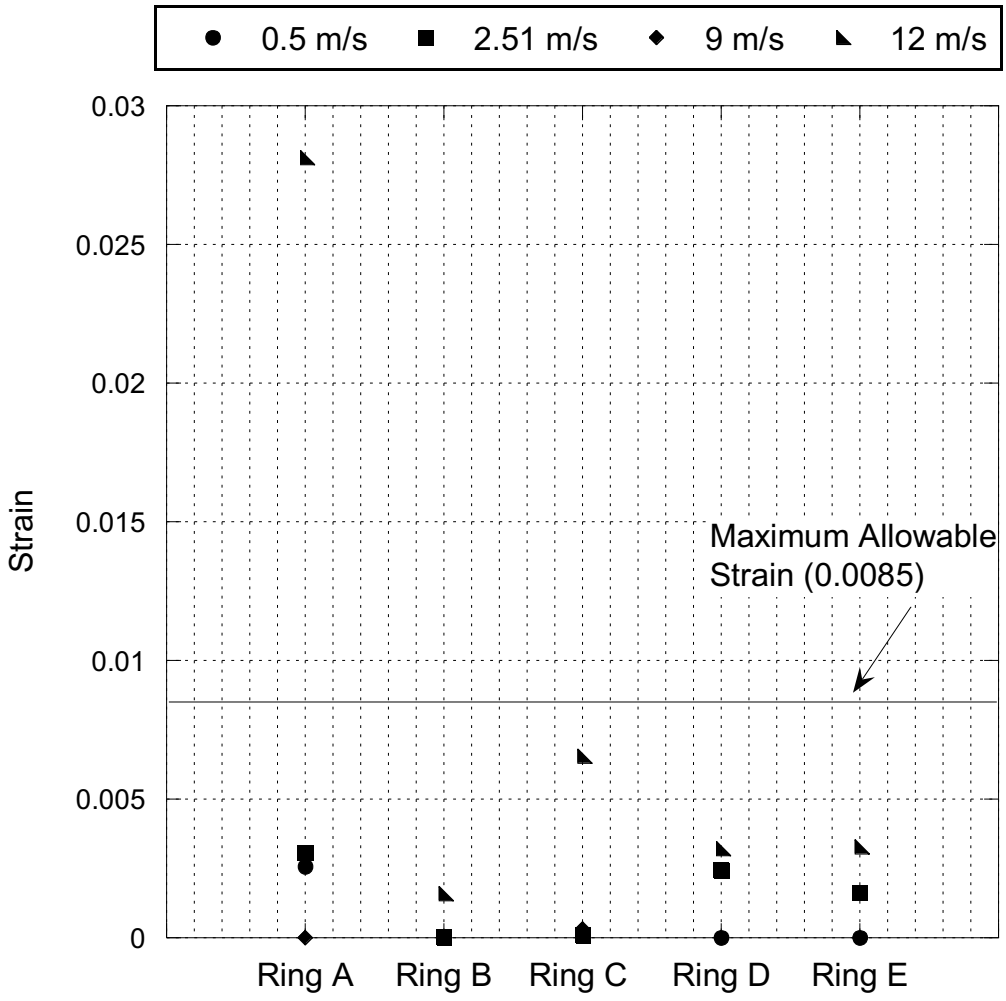

Figure 4.14 A comparison of equivalent plastic strain values taken along the center-line of the barrier for each velocity simulation. Maximum allowable strain of the steel (0.0085) is denoted by a horizontal line across the plot.

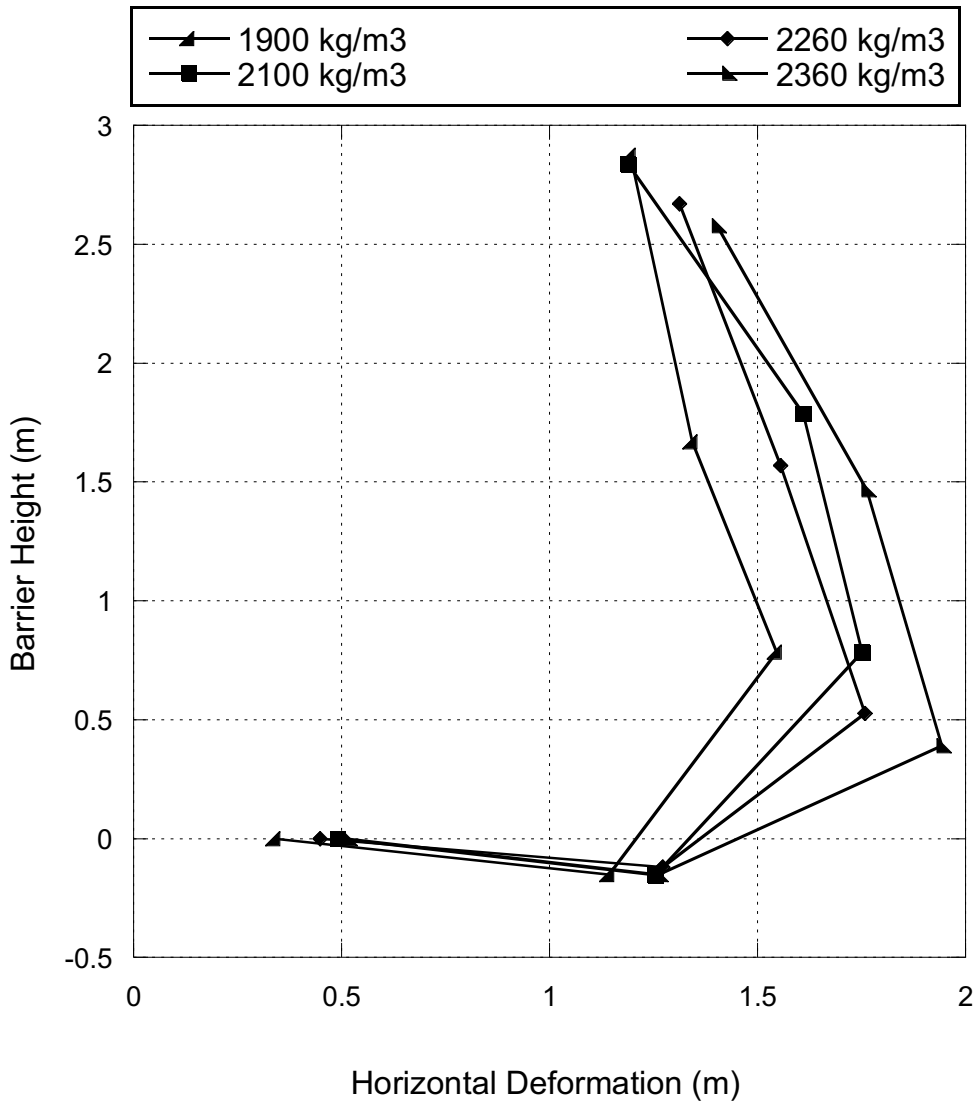

Figure 4.15 The final deformed shape of the barrier for each density simulation. Final deformation was taken along the centerline from Rings A through E.

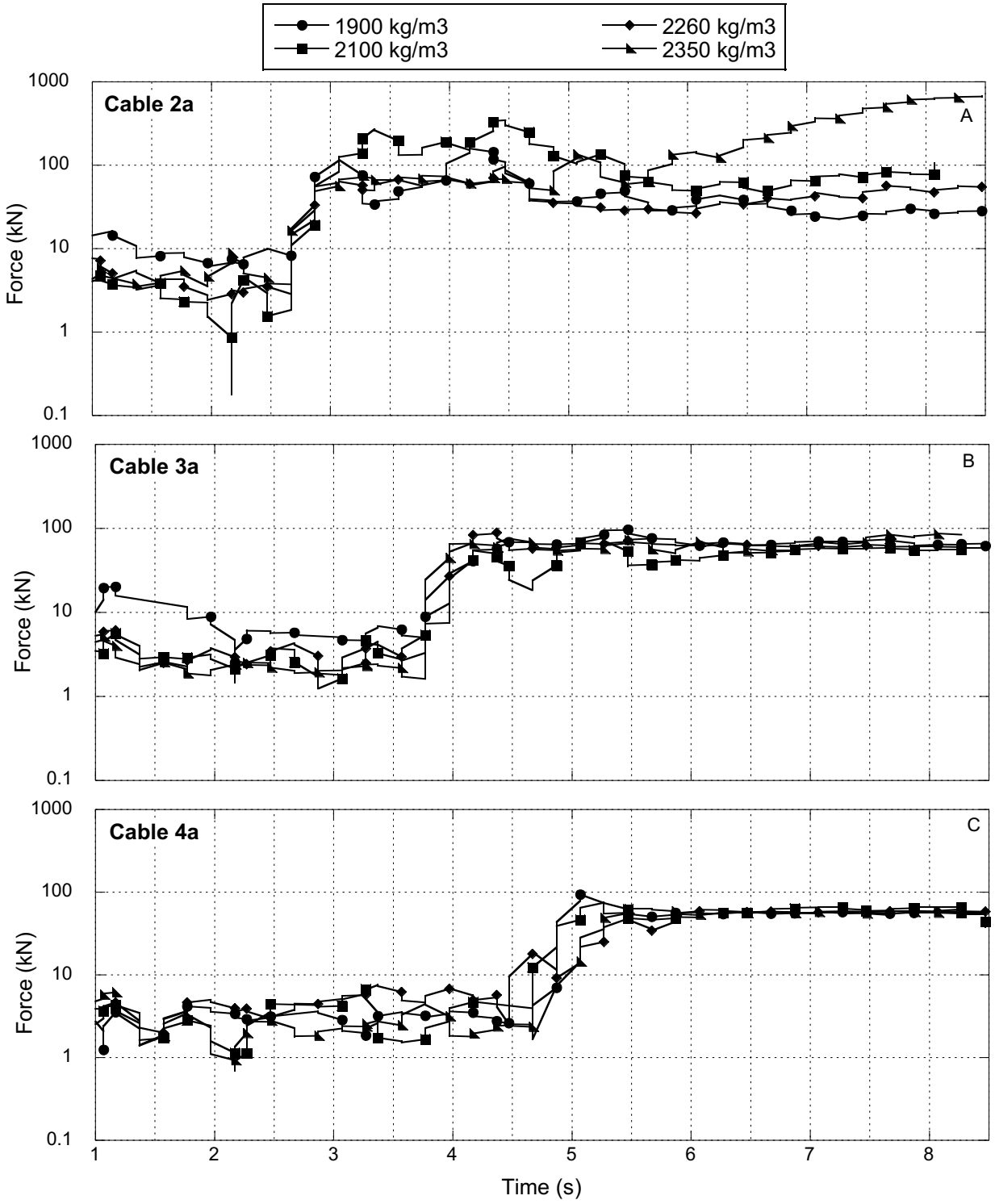

Figure 4.16 A comparison of cable tension over time in (a) Cable 2a; (b) Cable 3a; and (c) cable 4a for each of the density simulations. Tensions for each simulation (i.e. 1900, 2100, 2260, and 2350 kg/m^3) for each respective cable are plotted together to compare the affect each density has on the induced tension.

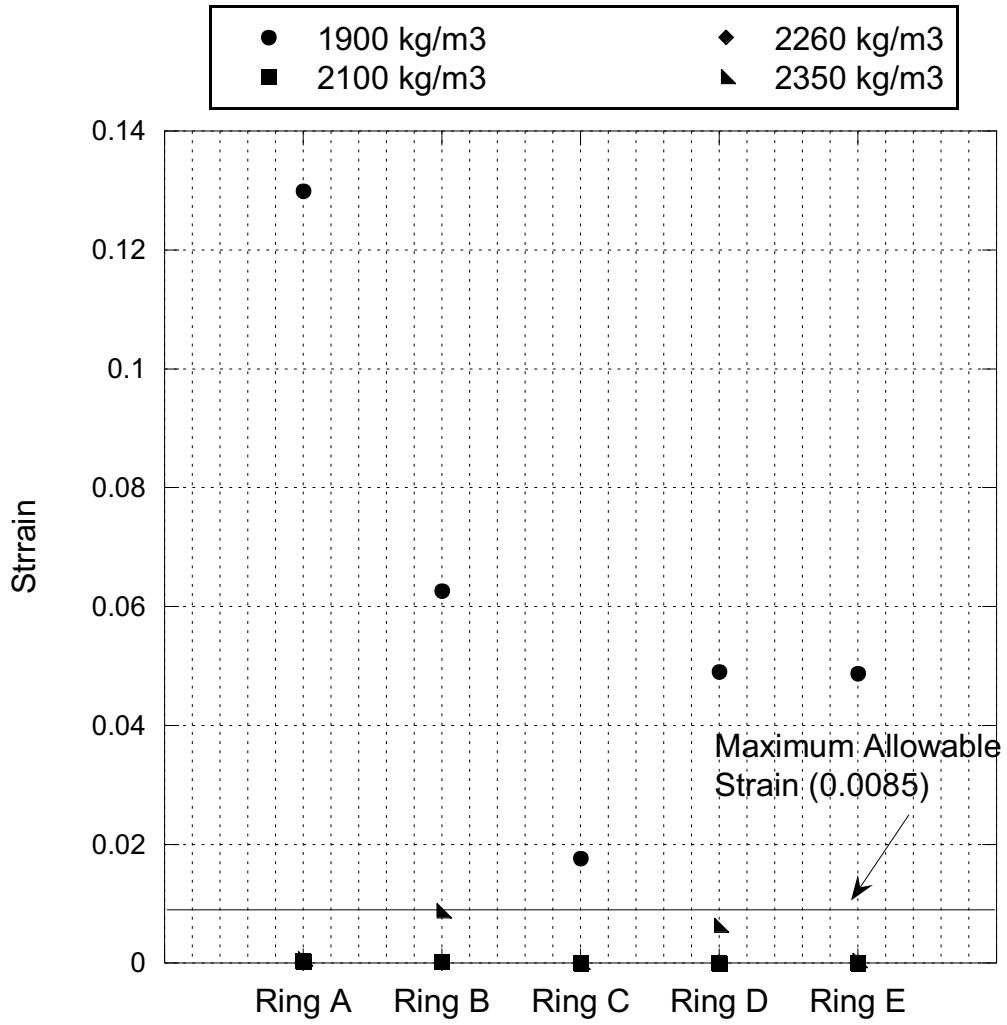

Figure 4.17 A comparison of equivalent plastic strain values taken along the center-line of the barrier for each density simulation. Maximum allowable strain of the steel (0.0085) is denoted by a horizontal line across the plot.

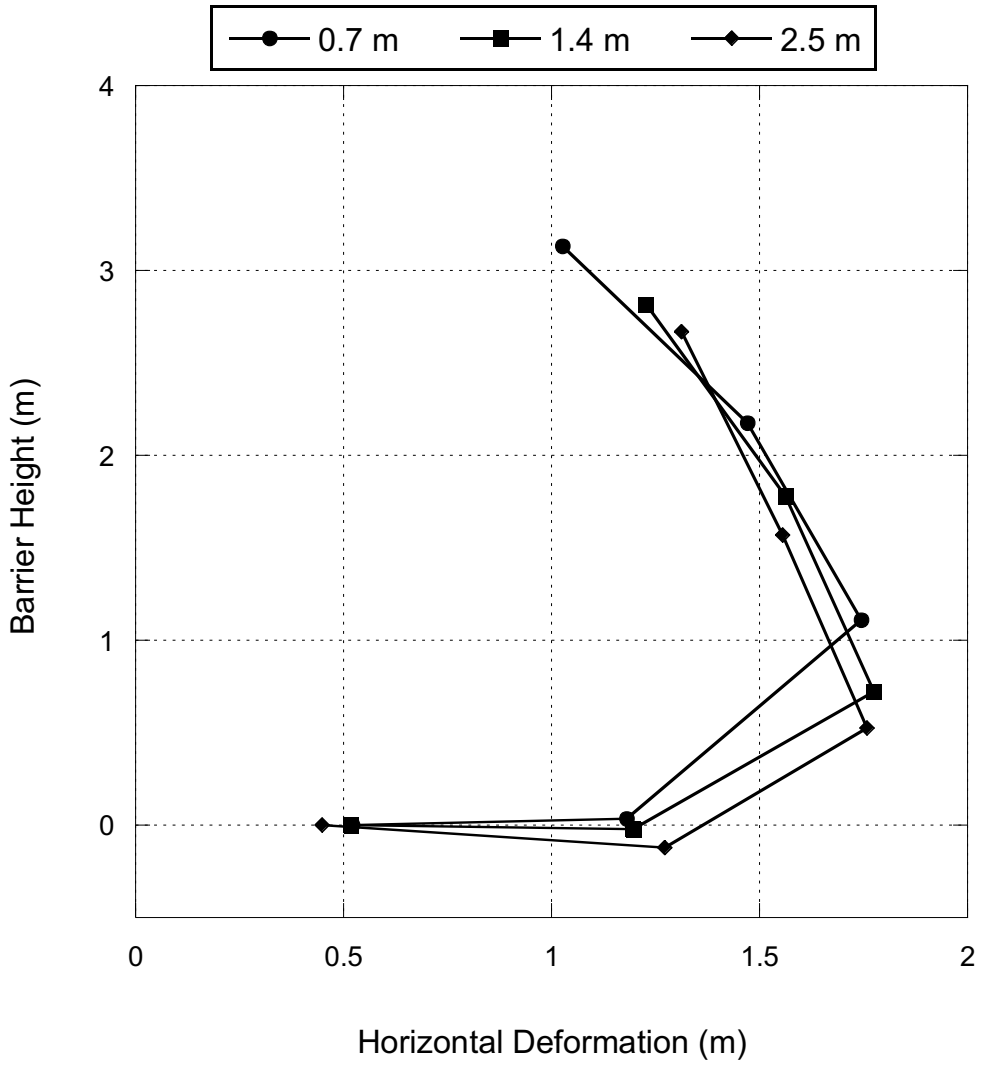

Figure 4.18 The final deformed shape of the barrier for each surge height simulation. Final deformation was taken along the centerline from Rings A through E.

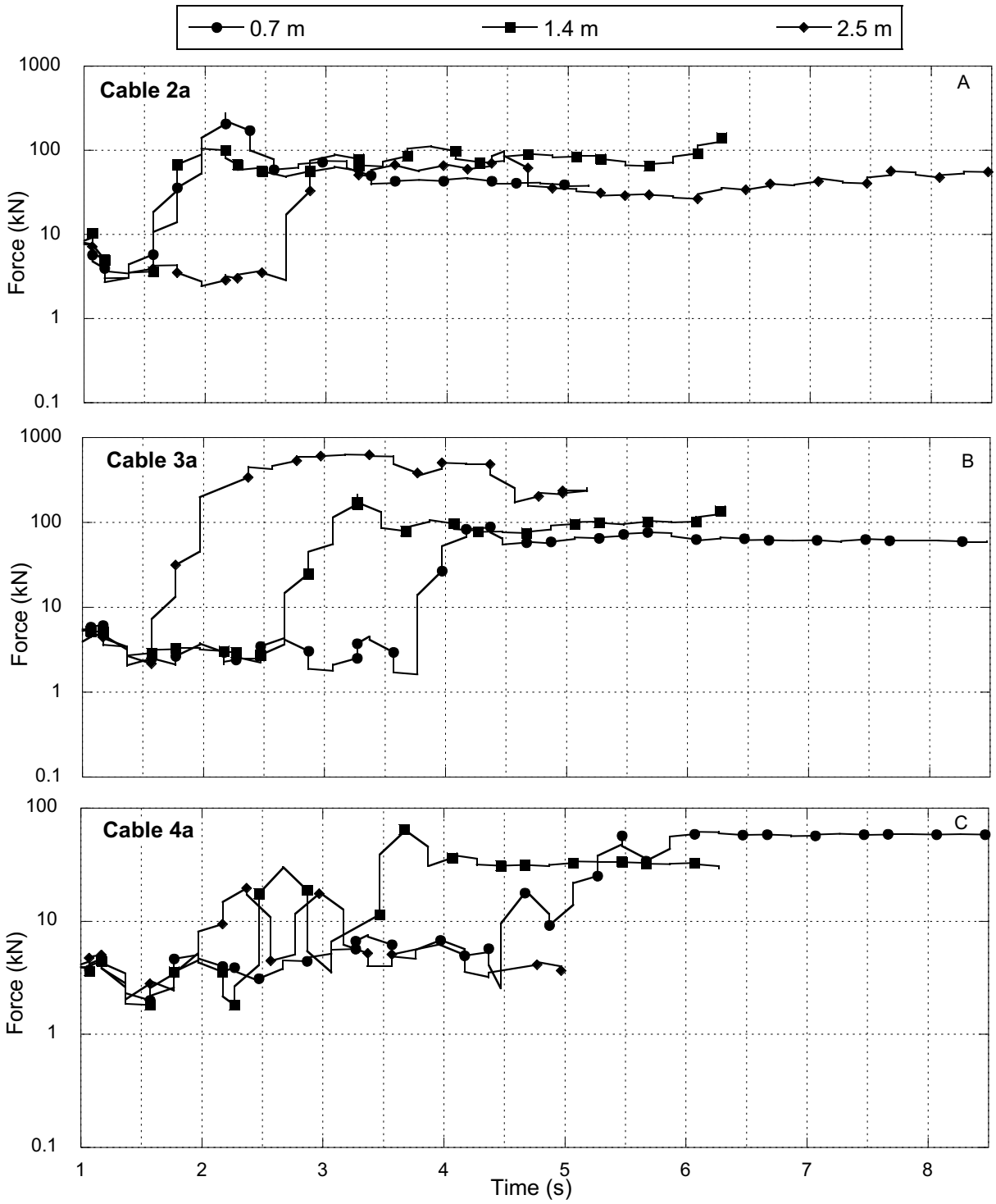

Figure 4.19 A comparison of cable tension over time in (a) Cable 2a; (b) Cable 3a; and (c) cable 4a for each of the surge simulations. Tensions for each simulation (i.e., 0.7, 1.4, and 2.8 m) for each respective cable are plotted together to compare the affect that surge height has on the induced tension.

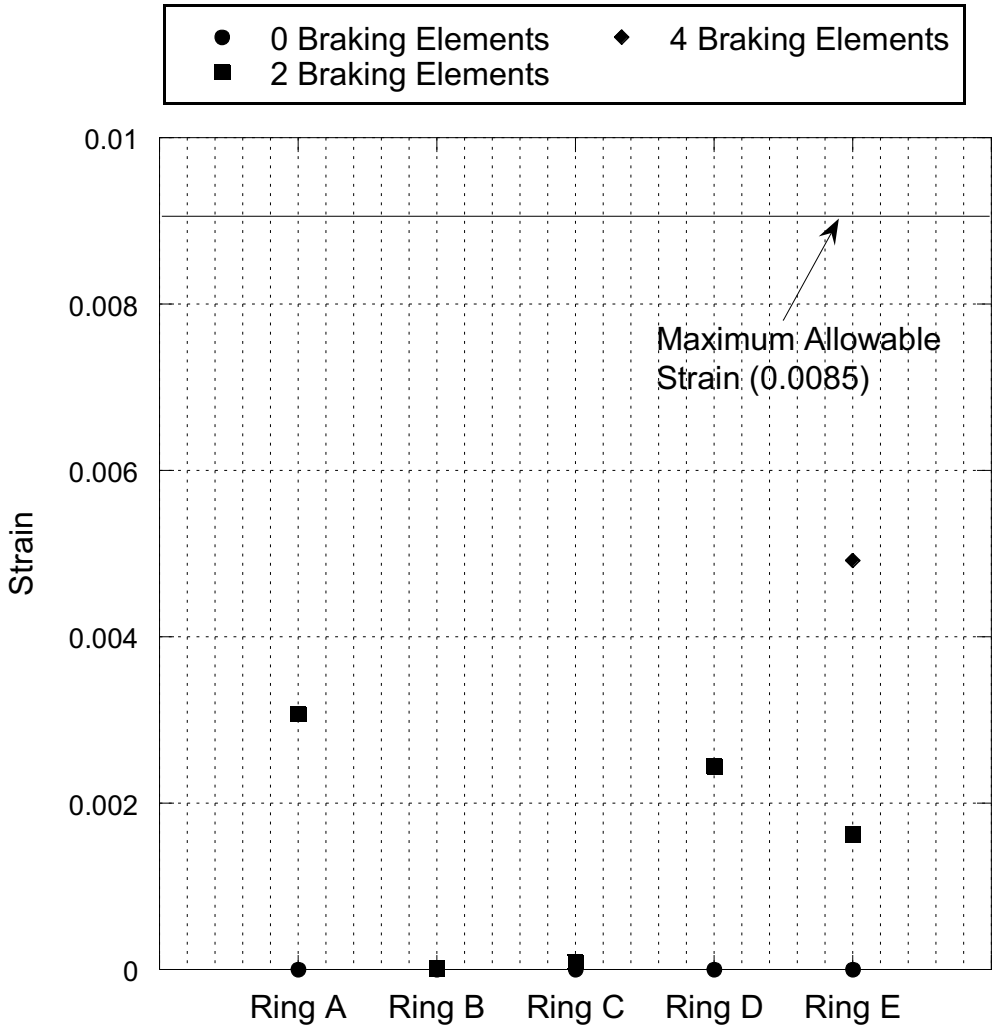

Figure 4.20 A comparison of equivalent plastic strain values taken along the center-line of the barrier for each surge height simulation. Maximum allowable strain of the steel (0.0085) is denoted by a horizontal line across the plot.

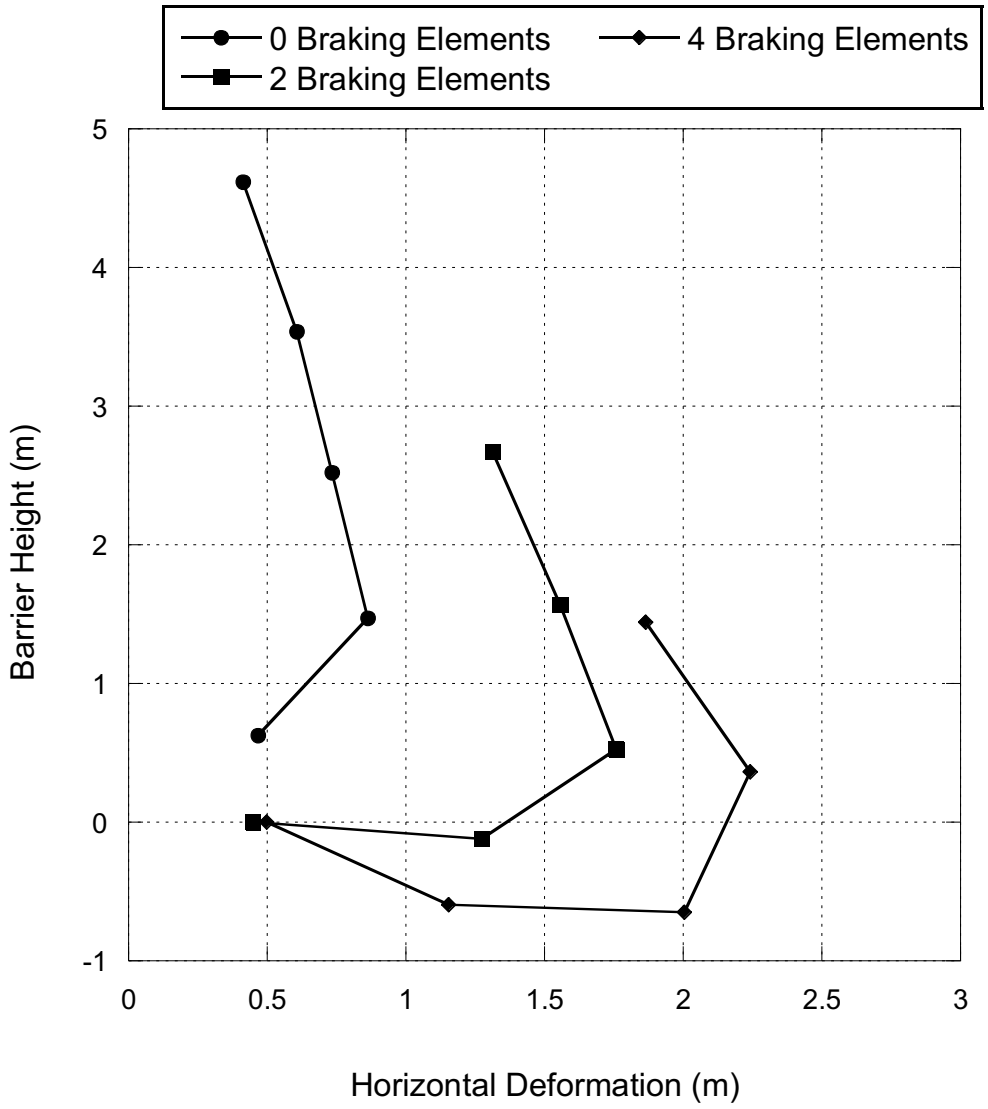

Figure 4.21 The final deformed shape of the barrier for each braking element simulation. Final deformation was taken along the centerline from Rings A through E.

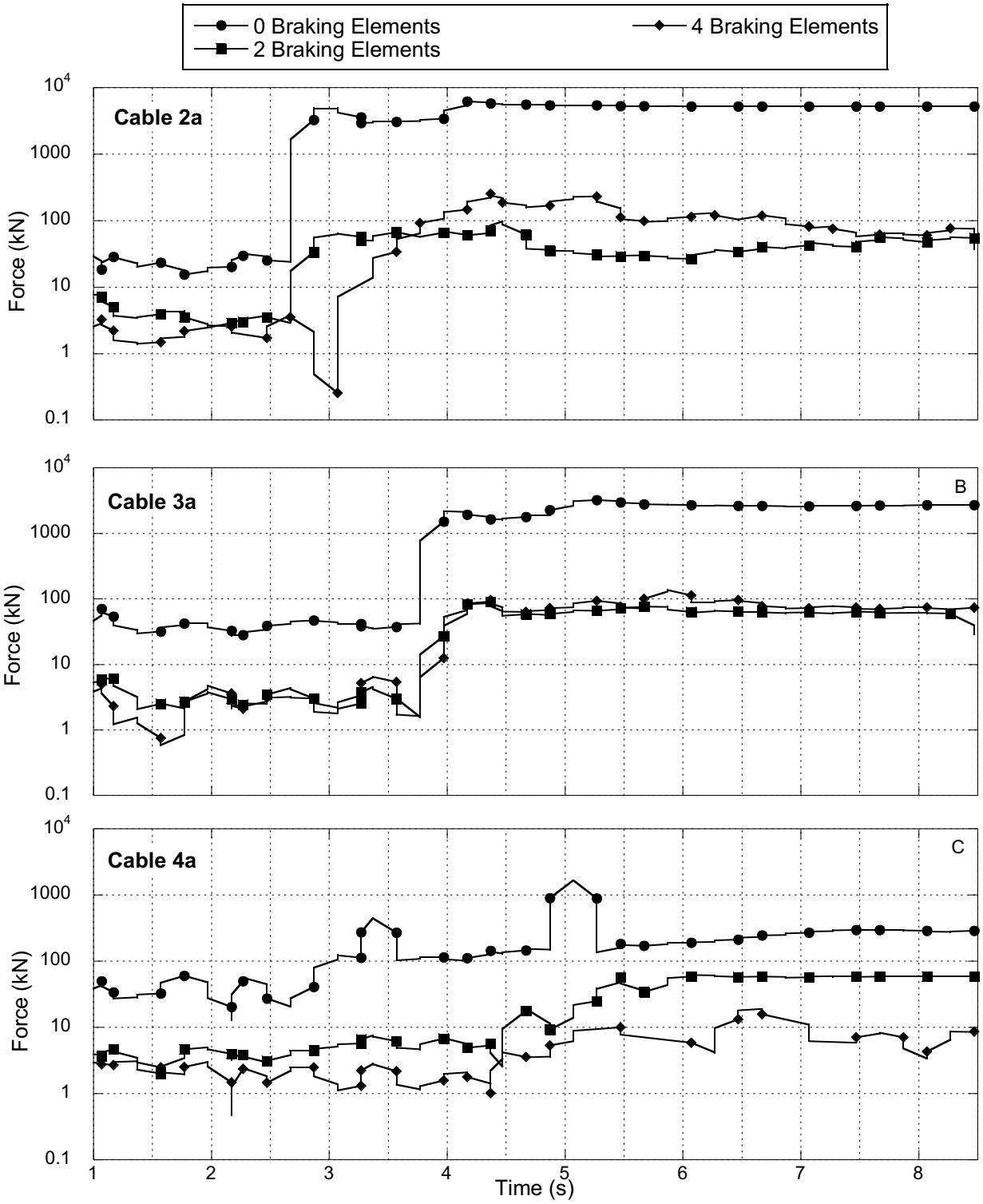

Figure 4.22 A comparison of cable tension over time in (a) Cable 2a; (b) Cable 3a; and (c) cable 4a for each of the braking element simulations. Tensions for each simulation (i.e., 0, 2, and 4 elements) for each respective cable are plotted together to compare the affect that brake elements have on induced cable tensions.

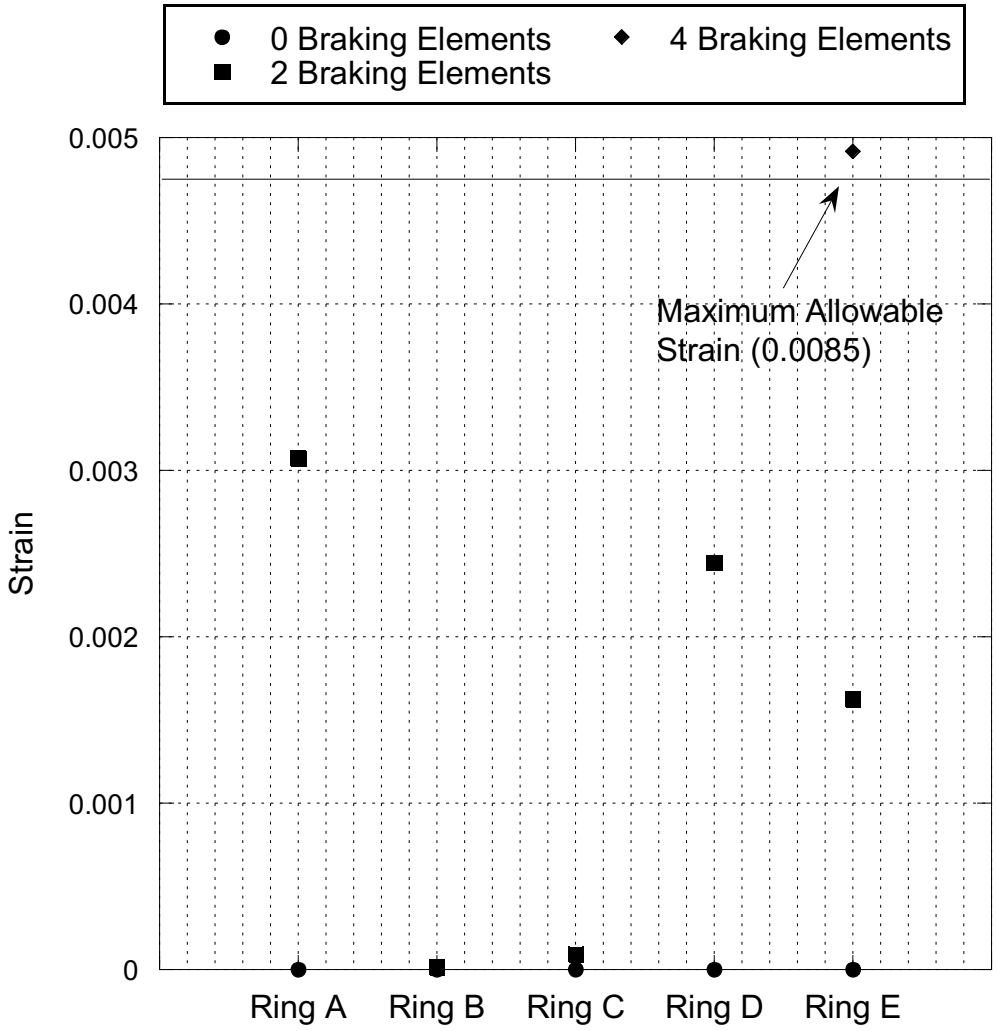

Figure 4.23 A comparison of equivalent plastic strain values taken along the center-line of the barrier for each braking element simulation. Maximum allowable strain of the steel (0.0085) is denoted by a horizontal line across the plot.

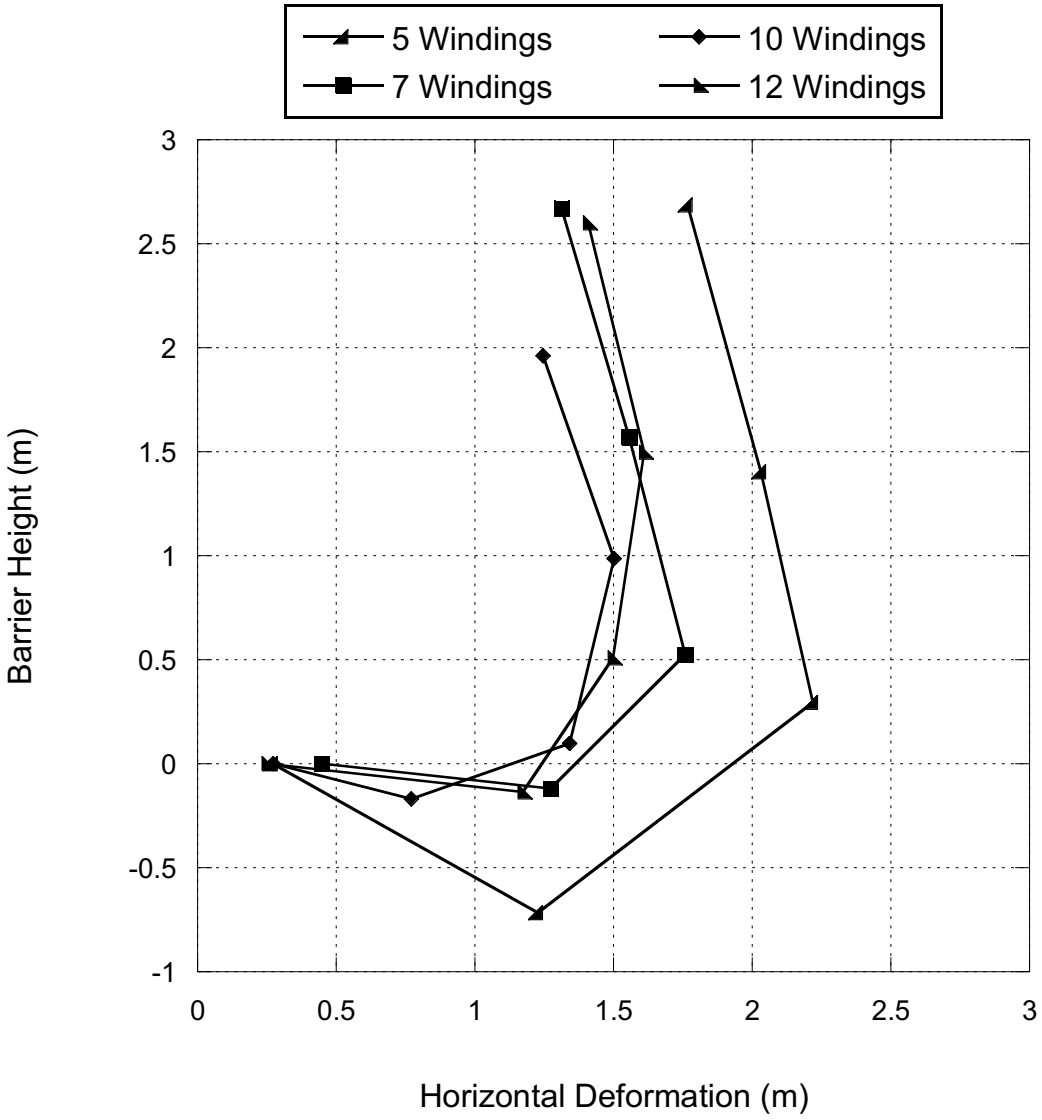

Figure 4.24 The final deformed shape of the barrier for each ring winding simulation. Final deformation was taken along the centerline from Rings A through E.

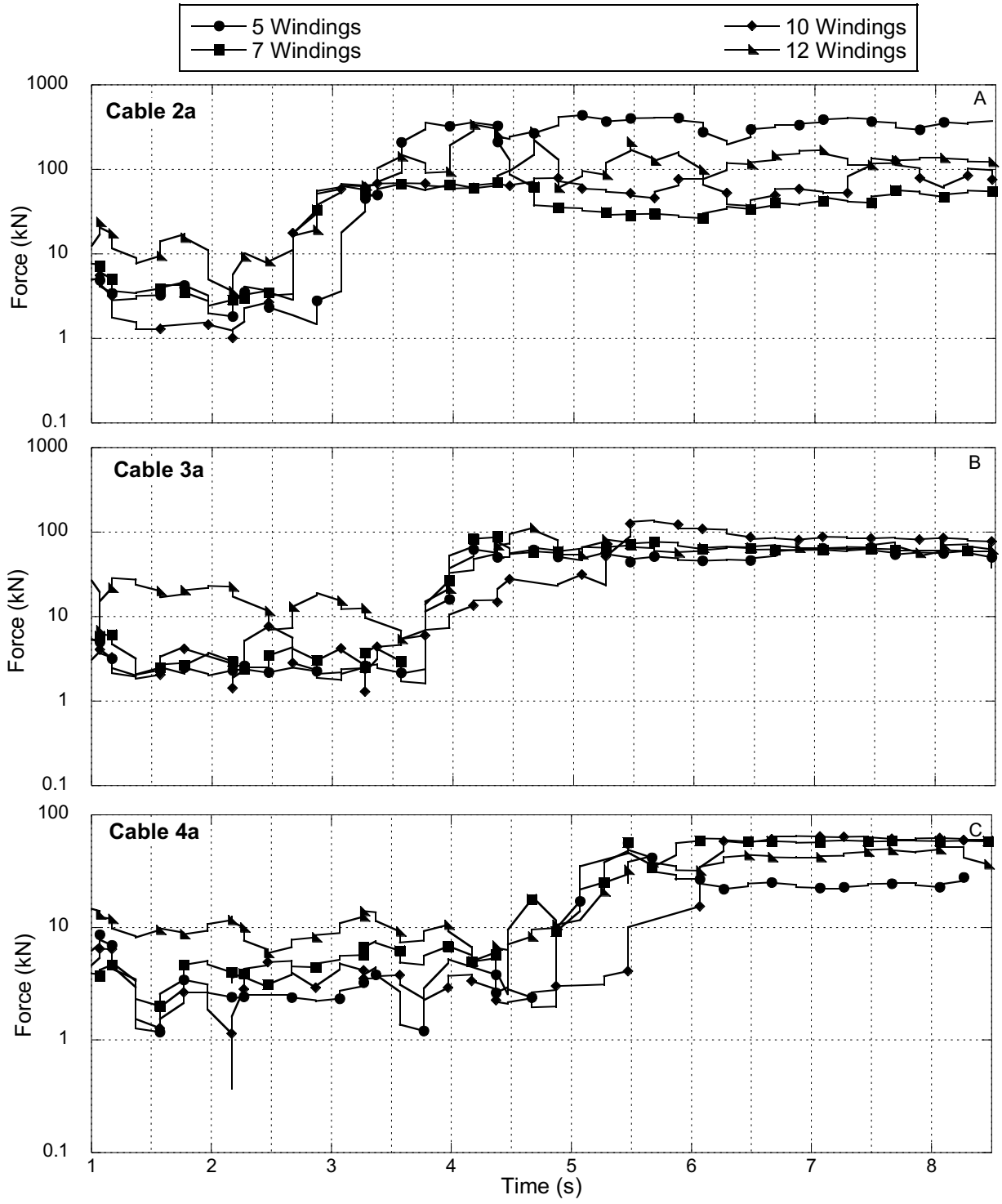

Figure 4.25 A comparison of cable tension over time in (a) Cable 2a; (b) Cable 3a; and (c) cable 4a for each of the winding simulations. Tensions for each simulation (i.e., 5, 7, 10, and 12 windings) for each respective cable are plotted together to compare the affect that the cross-sectional area of the individual rings have on induced cable tension.

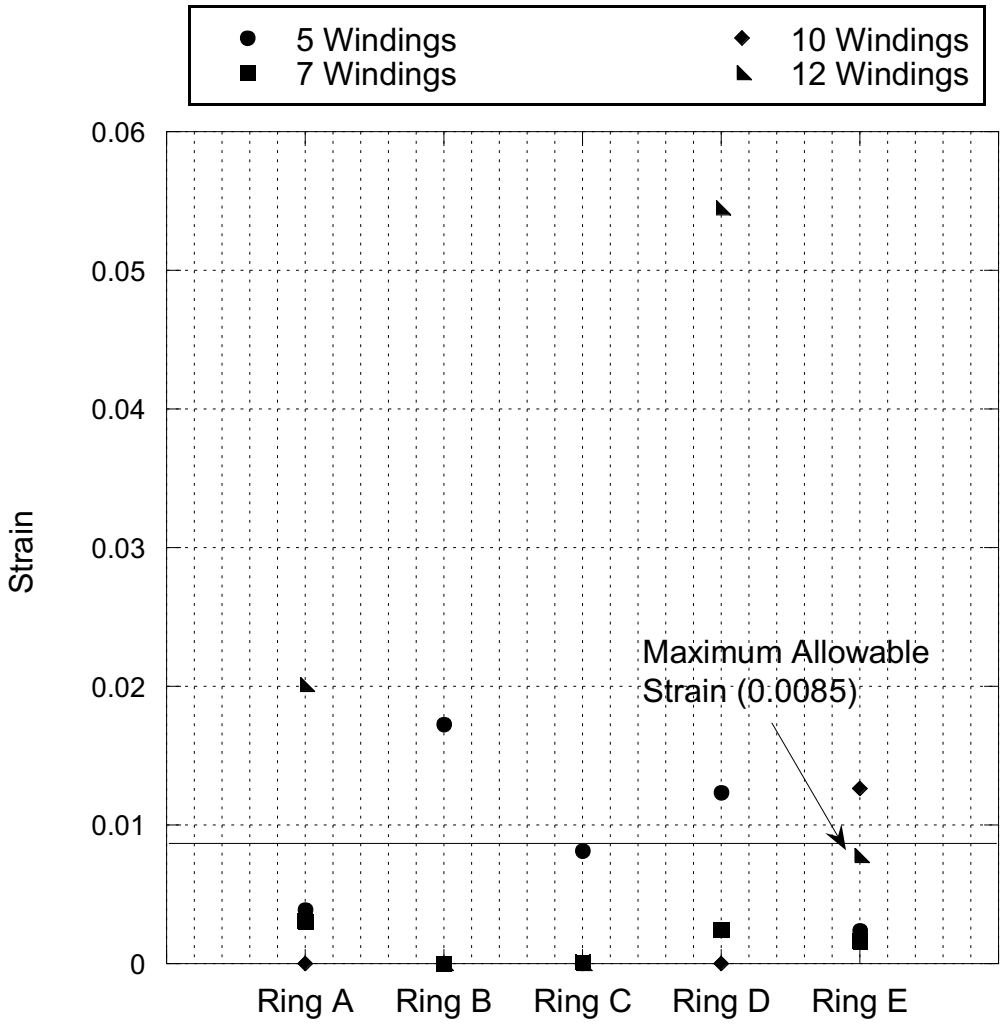

Figure 4.26 A comparison of equivalent plastic strain values taken along the center-line of the barrier for each ring winding simulation. Maximum allowable strain of the steel (0.0085) is denoted by a horizontal line across the plot.

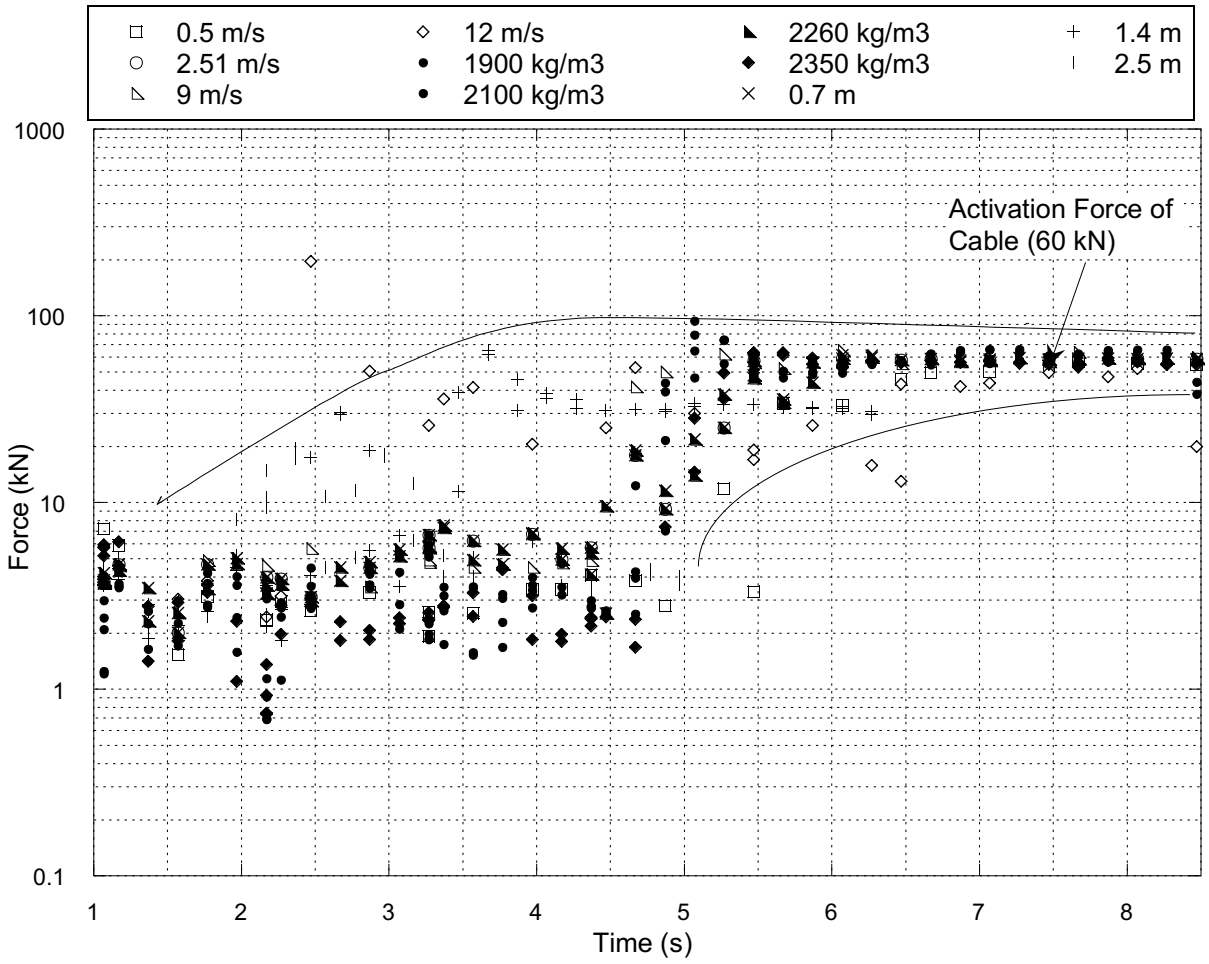

Figure 4.27 A comparison of cable tension results the geotechnical parameters analyzed. Tension is plotted for all cables studied (i.e., Cable 2a, Cable 3a, and Cable 4a) and geotechnical parameters (i.e. velocity, density, surge height). Tensions start around 5 kN and increase to approximately 60 kN.

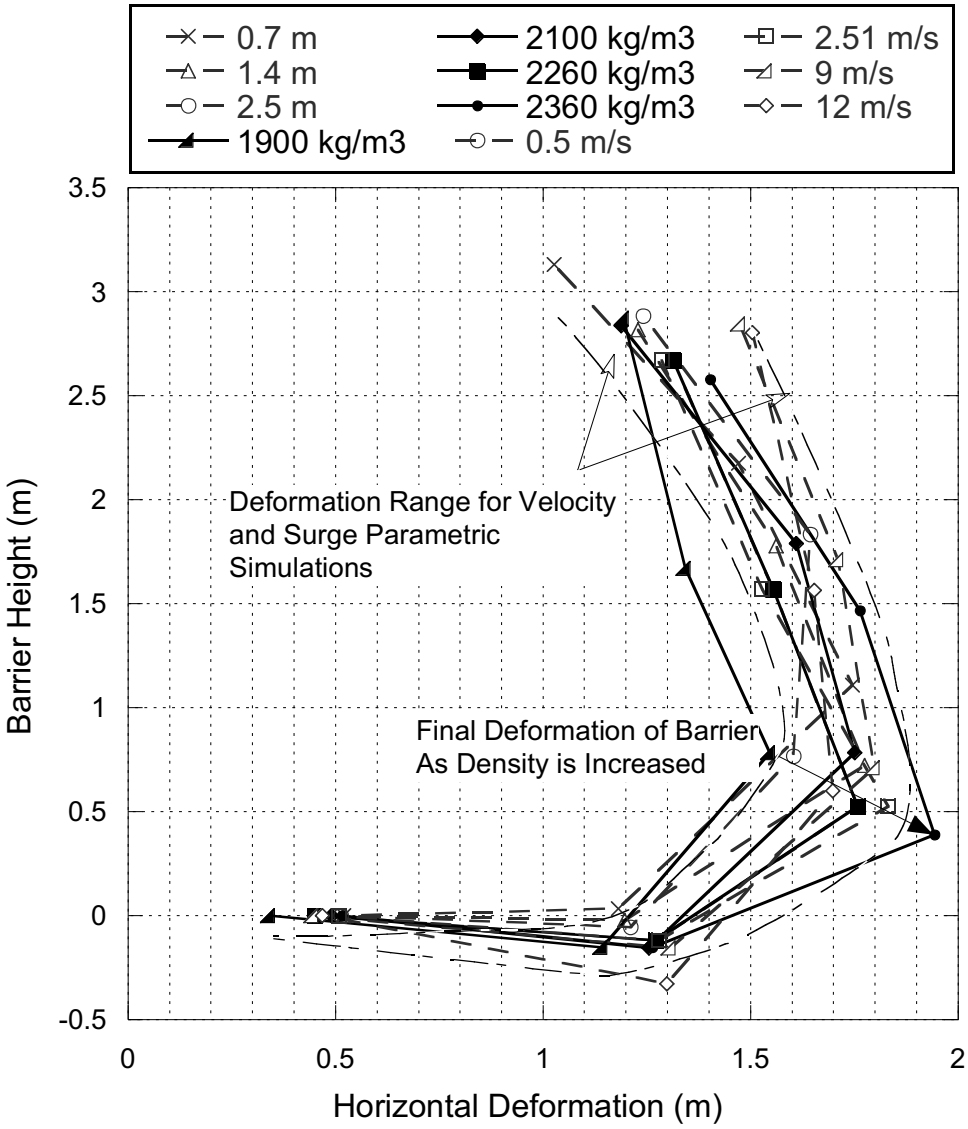

Figure 4.28 A comparison of final barrier deformation for all geotechnical parameters analyzed (i.e. velocity, density, surge height). Final deformation is not affected by velocity or surge height, as maximum deformations fall between 1.5 m and 1.7 m with no consistent trend. Increasing density is shown to increase surge height and the maximum deformation progression for each density simulation is called out.

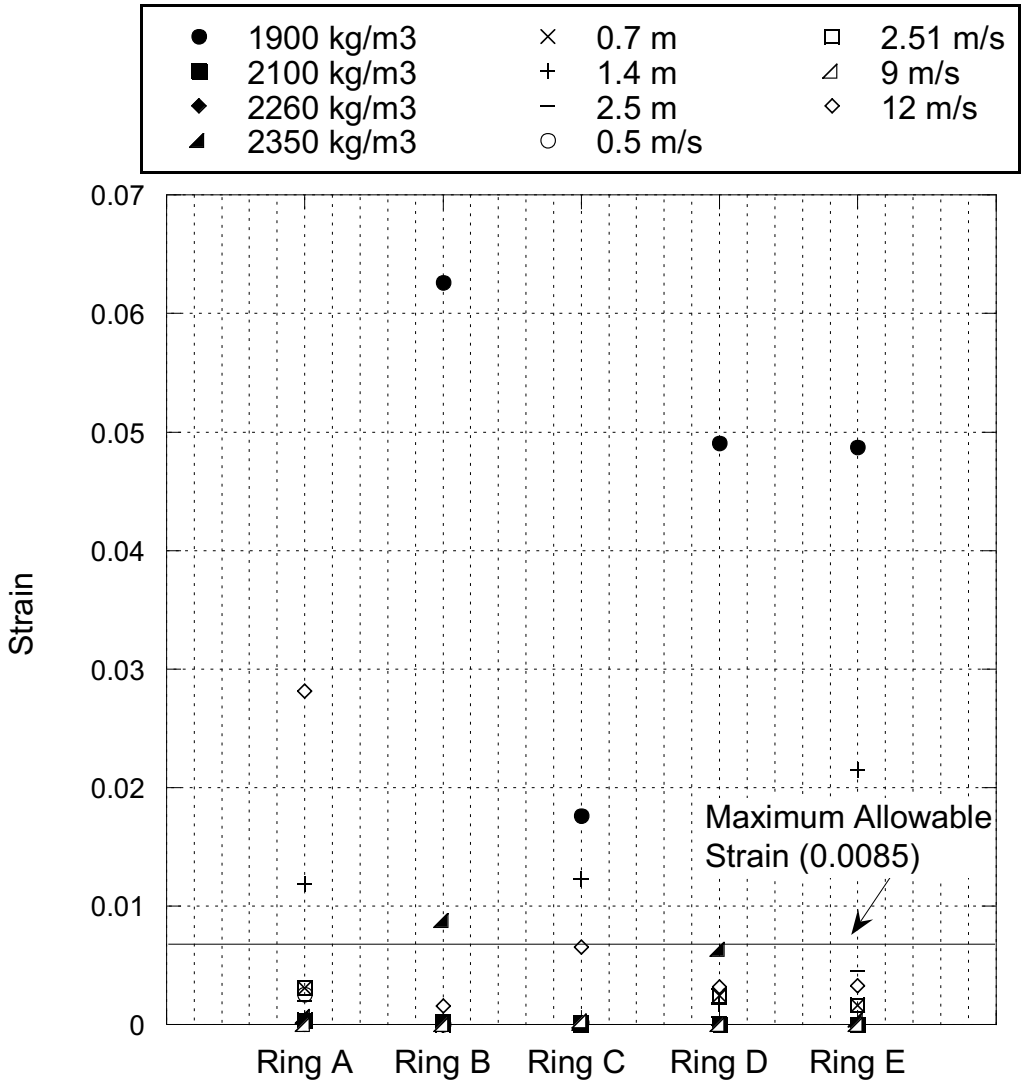

Figure 4.29 A plot of all equivalent plastic strains for the geotechnical parameters analyzed (i.e. velocity, density, and surge height). The majority of strains are shown to fall below the maximum allowable with Rings B – C of 1900 kg/m^3 and Ring B of 2350 kg/m^3 exceeding strains of 0.0085.

CHAPTER 5: SUMMARY AND CONCLUSIONS

A finite element model (FEM) of a flexible ring-net barrier was developed to simulate the coupled interactions of a debris-flow impacting the barrier and deformation of the barrier. Barrier deformation and stresses induced in the cables predicted with the FEM were comparable to the in-situ field test performed by Ferrero et al. (2015). The FEM yielded a closer prediction of final barrier deformation to actual barrier deformation as compared to an analytical model developed by Brighenti et al. (2013). Induced cable tensions predicted by the FEM were comparable to measured tensions and tensions predicted via the analytical model.

A parametric study of the flexible ring-net barrier was conducted using the FEM to assess geotechnical and structural engineering parameters. Results from the FEM simulations indicated that the loading induced by the debris flow, more so that the debris flow properties, contributed to the stress and deformation response of the barrier. The parametric study results also emphasized the importance of braking elements overall barrier performance. The braking elements act as load-reduction mechanisms that allow the barrier to deform upon loading while reducing tension developed in the cables.

There are several benefits to using a FEM to simulate the coupled interaction of debris-flow loading and structural response of a ring-net barrier. Modelling individual components of the barrier allowed for a more customized model to be developed to represent a complex process scenario. Although in this study deformation was evaluated at the center of the barrier, the FEM can yield deformation for any location in the model. This level of simulation should prove beneficial in design as any point of interest within the ring-net barrier can be evaluated. Additionally, the ability to couple structural response of the flexible ring-net barrier and the debris flow is advantageous when evaluating the dynamic nature of a debris flow on barrier response. Debris flow parameters also can be modified in the FEM to assess a variety of debris flow scenarios for a single barrier.

Although there are benefits of using a FEM, there are also challenges. More complex numerical models are more computationally intensive and require longer computation times. For example, the FEMs completed in this study averaged 2 d of computation time on a standard PC. Furthermore, an analytical model (e.g., as developed by Brighenti et al. 2013) can be programmed in Excel, whereas FEMs typically require specialized software (e.g., ABAQUS). Finally, the increased complexity of coupling debris flows and structural response of a barrier in a FEM may increase the likelihood for modeling errors.

The FEM developed herein coupled a debris flow and structural barrier to create a model that captures interaction between a flow and the barrier. Complexity in the numerical simulation of the ring-net structure limited the extent of modeling completed for the debris flow. The debris flow was modeled with individual blocks representing a part of a debris flow instead of simulating the overall flowing mass. This simplification of the debris flows potentially limited the benefit of representing the barrier as a complex system of individual elements. The segmented block flow was representative of an actual debris flow in regards to comparisons of the structural response of the field-scale experiment. Thus, the segmented debris flow used in the FEM herein can provide insight as to behavior of the barrier during loading; however, additional research is needed to evaluate how different simulations of the debris flow influence response of the flexible ring-net barrier system.

To further investigate the response of flexible ring-net barriers to debris flow loading, FEMs should be developed with a simplified barrier system and more complex modeling of the debris flow to represent interactions are the particle level within the flow. Ultimately, coupled FEM simulations with more complex debris flows and the ring-net barrier FEM developed herein can be used to assess the level of model complexity needed for engineering design versus research-based investigations.

REFERENCES

ABAQUS (2005). Overview of ABAQUS/Explicit. [PDF]. *ABAQUS, Inc.*

Armanini, A. (1997) Dynamic impact of a debris flow front against a vertical wall. *Recent Developments on debris flows.* 208-226.

Ashwood, W. and Hungr, O. (2016). Estimating total resisting force in flexible barrier impacted by a granular avalanche using physical and numerical modeling. *Canadian Geotechnical Journal* 53:1700-1717.

Brighenti, R., Andrea, S., and Ferrero, A. M. (2013). Debris flow hazard mitigation: a simplified analytical model for the design of flexible barriers, *Computers and Geotechnics* 54 (9),1-15.

Bugnion, L., Denk, M., Shimojo, K., Roth, A., and Volkwein A (2008). Full-scale experiments on shallow landslides in combination with flexible protection barriers. *Proceedings of 1st world landslide forum.* Tokyo Japan. 99-102

Burtz, J.L. (2003). Behavior and design of grouted anchors loaded in tension including edge and group effects and qualification of engineered grout products. *University of Florida.* 2003.

Calvetti, F., di Prisco, C.G., and Vairaktaris, E. (2015). DEM assessment of impact forces of dry granular masses on rigid barriers, *Acta Geotechnica.*

Canelli, L., Ferrero, A.M., Migliazza, M., and Segalini, A. (2012). Debris flow risk mitigation by the means of rigid and flexible barriers – experimental tests and impact analysis, *Natural Hazards and Earth System Sciences*, 12, 1693-1699.

Cannon, S. (2001). Debris-flow generation from recently burned watersheds. *United States Geological Survey.*

Cannon, S., and Gartner, J. (2005). Wildfire-related debris flow from a hazards perspective, *Debris-flow hazards and related phenomena,* 363-385.

Cannon, S., Gartne,r J., Wilson, R., Bowers, J., and Laber, J. (2008). Storm rainfall conditions for floods and debris flows from recently burned areas in southwestern Colorado and southern California.*Geomorphology,* 96: 250-269.

Cannon, S., Gartner, J., Rupert, M., Michae, J., Rea, A., and Parrett, C. (2010) Predicting the probability and volume of postwildfire debris flows in the intermountain western United States, *Geological Society of America Bulletin.*

Choi, C. E., Ng, C. W. W., Law, R.P.H., Song, D., Kwan, J.S.H., and Ho, K.K.S. (2015). Computational investigation of baffle configuration on impedance of channelized debris flow, *Canadian Geotechnical Journal*, 52(2), 182-197.

Coe, J, and Godt, J. (2003). Historical debris flows along the Interstate-70 corridor in Clear Creek County, Central Colorado, *U.S. Geologial Survey.*

Costa, J. (1984). Physical Geomorphology of Debris Flows. *Developments and Applications of Geomorphology. Heidelberg, Germany. Springer-Verlag.*

Coussot, P. and Meunier, M. (1996). Recognition, classification and mechanical description of debris flows, *Earth Science Reviews.* 40: 209-227

Das, B.M. (2013). Principles of Foundation Engineering. Seventh Edition. Boston, MA: Cenage Learning.

De Cock, F. (2008). Ground Anchors : Overview of Types, Installation Methods and Recent Trends. Proceedings of the International Symposium of Ground Anchors- Limelette test field results. May 2009. Brussels, Belgium.

DeNatale, J.S., Iverson, R.M., Major, J.J., LaHusen, R.G., Fiegel, G.L., and Duffy, J.D. (1999). *Experimental Testing of Flexible Barriers for Containment of Debris Flows*, Open-File Report 99-205, U.S., Geological Survey, Denver, CO, USA.

DeWolfe, V., Santi, P., Ey, S., and Gartner, J. (2006). Effective mitigation of debris flows at Lemon Dam, La Plata County Colorado. *Geomorphology.* 96: 366-377.

Escallon, J.P., and Wendeler, C. (2013). Nunmerical simulations of quasi-static and rockfall impact tests of ultra-high strength tseel wire-ring nets using Abaqus/Explicit. 2013. *SIMULA Community Conference.*

ETAG 027 (2013). Guideline for European technical approval of falling rock protection kits. European Organisation for Technical Approvals. April 2013.

Ferrero, A.M., Segalini, A., and Umili, G. (2015) Experimental tests for the application of an analytical model for flexible debris flow barrier design. *Engineering Geology 185:33-42.*

Gartner, J., Cannon, S., Santi, P., and DeWolfe, V. (2007). Emperical models to predict the volumes of debris flwos generated by recently burned basins in the western U.S. *Geomorpholoy.* 69:339-354.

Gercek, H. (2006). Poisson's ratio values for rocks. *International Journal of Rock Mechanics & Mining Sciences.* 44:1-13.

Geobrugg (2016). Ring net barriers made of high-tensile steel wire: the economical solution to debris flow. [Brochure]. *From www.geobrugg.com*

Godt, J. and Coe, J. (2007). Alpine debris flows triggered by a 28 July 1999 thunderstorm in the central Front Range, Colorado. *Geomorphology* 84.1: 80-97.

Highland, L.M. (2012). *Landslides in Colorado, USA: Impacts and Loss Estimation for Year 2010*, Open-File Report 2012-1204, U.S., Geological Survey, Denver, CO, USA.

Hungr, O. (1995). A model for the runout analysis of rapid flow slides, debris flows, and avalanches. *Canadian Geotechnical Journal* 32.4: 610-623.

Hungr, O. (2000). Analysis of debris flow surges using the theory of uniformly progressive flow. *Earth Surface Processes and Landforms* 25.5: 483-495.

Hungr, O., McDougall, S., and Bovis, M. (2005). Entrainment of material by debris flows. In: *Debris Flow Hazards and Related Phenomena*, Jakob, M. and Hungr, O. (eds), Springer, Heidelberg, 135-158.

Hungr, O., Leroueil, S., and Picarelli, L. (2014). The Varnes classification of landslide types, an update, *Landslides*, 11(2), 167-194.

Iverson, R.M. (1997). The physics of debris flows, *Reviews of Geophysics*, 35(3), 245-296.

Iverson, M. R. (2005) Debris Flow Mechanics. *Debris flow Hazards and related Phenomena*.), *Springer Berlin Heidelberg* 6:105-134.

Iverson, R. M. (2012). Mechanics of Debris Flows and Rock Avalanches. H. J. S. Fernando *Handbook of Environmental Fluid Dynamics, Volume One: Overview and Fundamentals*. 573-587.

Jakob, M. (2004) A size classification of debris flows. *Engineering Geology.* 79:151-161.

Jakob, M. and Hungr, O. (2005). Debris flow hazards and related phenomena. Chichester, UK:Praxis Publishing Ltd.

John Sakash Company. (2016). Wire rope technical information. [Brochure]. *From www.johnsakash.com/products/wire-rope/wire-rope-information*

Keaton, J.R., Wartman, J., Anderson, S., Benoit, J., de LaChapelle, J., Gilbert, R., and Montgomery, D.R. (2014). *The 22 March 2014 Oso Landslide, Snohomish County, Washington*, Geotechnical Extreme Events Reconnaissance.

Leonardi, A., Wittel, F.K., Mendoza, M., Vetter, R., and Herrmann, H.J. (2014). Particle-fluid-structure interaction for debris flow impact on flexbile barriers. Computer Aided Civil and Infrastructure Engineering.

Maccaferri (2016). Rockfall protection and snow barriers. Mac.Ro Systems. [Brochure] from www.maccaferri.com

Matweb (2016). 6000 Series Aluminum Alloy (2016). http://www.matweb.com/.

Mears, A.I. (1997). Debris flow hazard analysis and mitigation-an example from Glenwood Springs, Colorado. *Colorado Geological Survey Department of Natrual Resources.* Information Series 8.

Merifield, R.S. and Sloan, S.W. The ultimate pullout capacity of anchors in frictional soils. *Canadian Geotechnical Journal*. 43: 852-868.

Mizuyama, T. (2008). Structural countermeasures for debris flow disasters, *International Journal of Erosion Control Engineering*, 1(2), 38-43.

Murasishi, H., Samizo M., Sugiyama, T. Development of a Flexible Low-Energy Rockfall Protection Fence. QR of RTRI, Vol. 26. September 2005.

Napper, C. (2006). Burned Area Emergency Treatment Catalog. *United States Department of Argiculture Forest Service National Technology & Development Program.*

Ng, C.W.W., Choi, C.E., Song, D., Kwan, J.H.S., Koo, R.C.H., Shiu, H.Y.K., and Ho, K.K.S. (2014). Physical modeling of baffles influence on landslide debris mobility, *Landslides*, online Feb. 2014, 10.1007/s10346-014-0476-y, 1-18.

Phillips, C., and Davis, T. (1991) Determining rheological parameters of debris flow material. *Geomorphology,* 4:101-110.

Pouliquen, O. and Vallance, J.W. (1999) Segregation induced instabilities of granular fronts, *Chaos: An Interdisciplinary Journal of Nonlinear Science*. 9:621-632.

Prochaska, A.B., Santi P.M., Higgins J.D. (2008). Relationships between size and velocity for particles within debris flows. *Canadian Geotechnical Journal* 45:1778-1783.

Rajapske, R.A. (2015) Geotechnical Engineering Calculations and Rules of Thumb. Second Edition. Waltham, MS: Butterworth-Heinemann. 34:336.

Reddy, J. N. (1993). An introduction to the finite element method. Vol. 2. No. 2.2. New York: McGraw-Hill.

Roth, A., Wendeler, C., and Amend, F. (2010). Use of properly designed flexible barriers to mitigate debris flow natural hazards. *GeoFlorida 2010: Advances in Analysis, Modeling and Design.* 3207-3216.

Santi, P., Higgins, J., Cannon, S., and DeGraff, J., (2006). Evaluation of Post-Wildfire Debris Flow Mitigation Methods and Development of Decision-Support Tools. *Final Report to the Joint Fire Science Program.*

Santi, P., deWolfe, V.G., Higgins, J.D., Cannon, S.H., and Gartner, J.E. (2008). Sources of debris flow material in burned areas. *Geomorphology* 96:310-321.

Santi, P. (2009). That Liquefaction of Her Clothes: Mitigating Debris Flows in the Post-Wildfire Landscape. *Fire Science Breif* 45:1-6.

Santi, P. (2012). Challenges for debris-flow mitigation in Colorado: helpful ideas from recent research, *GeoChallenges: Rising to the Geotechnical Challenges of Colorado*, GPP 7, ASCE, 1-16

Santi, P. and Morandi, L. (2013). Comparison of debris-flow volkumes from burned and unburned areas. *Landslides* 10.6: 757-769.

United States Navy. (1976). U.S. Navy Wire-Rope Handbook on Design and Engineering of Wire-Rope Systems Volume I. *Direction of Commander Naval Sea Systems Command.*

Sasiharan, N., Muhunthan, B., Badger, T.C., Shu, S., Carradine, D.M. (2006). Numerical analysis of the performance of wire mesh and cable net rockfall protection systems, *Engineering Geology*, 88, 121-132.

Savage, S.B. and Iverson, R.M. (2003). Surge dynamics coupled to pore-pressure evolution in debris flows. *Proc. 3rd Int. Conf. on Debris-Flow Hazards Mitigation: Mechanics, Prediction, and Assessment*. Davos, Switzerland.

Sullivan Wire Rope & Rigging Inc. (2016). General Information on Wire Rope. [Brochure]. *From www.sullivanwirerope.com*

VanDine, D.F. (1996). Debris Flow Control Structures for Forest Engineering. *B.C. Ministry of Forests.* Victoria, B.C.

Varnes, D.J. (1978). Slope movement types and processes. In: Schuster, R.L., Krizek, R.J. (eds) *Landslides, Analysis and Control*, special report 176: Transportation Research Board, National Academy of Sciences, Washington, DC., pp. 11–33

Volkwein, A., Wendeler, C. and Guasti, G. (2011) Design of flexible debris flow barriers. *Italian Journal of Engineering Geology and Environment*. 1093-1100.

Volkwein, A. (2014). Flexible debris flow barriers design and application. *Swiss Federal Institute for Forest, Snow, and Landscape Research WSL.*

Volkwein, A., Baumann, R., Rickli, C., and Wendeler, C. (2015) Standardization for flexible debris retention barriers. *Engineering Geology for Society and Territory.* 2: 193-195.

Von Boetticher, A., Hübl, J., Wendeler, C., and Volkwein, A. (2011). Modeling the impact of shallow landslides on flexible protection barriers. *IMAG Conference 2011.*

Wendeler C., McArdell B.W., Rickenmann D., Volkwein A., Roth A., and Denk M. (2006). Field testing and numerical modeling of flexible debris flow barriers. *Proceedings of the 6th international conference on physical modelling in geotechnics.*

Wendeler, C., Volkwein, A., Roth, A., Denk, M., and Wartmann, S. (2007). Field measurements and numerical modelling of flexible debris flow barriers. *Debris Flow Hazards: Mitigation, Mechanics, Prediction, Assessment.* 681-687.

Wendeler, C., McArdell, B.W., Volkwein, A., Denk, M., and Gröner, E. (2008). Debris flow mitigation with flexible ring net barriers-field tests and case studies. *Monitoring, Simulation, Prevention and Remediation of Dense Debris Flows II.*

Wendeler, C. (2016). Debris-Flow protection systems for mountain torrents: Basic principles for planning and calculation of flexible barriers. WSL Berichte. Heft 44, 2016.